UNIVERSITY OF SOUTHAMPTON

Faculty of Engineering and Physical Sciences
School of Physics and Astronomy & Optoelectronics Research Centre

Nanoscale Metamaterials Tailored for Optical and Mechanical Applications

by

Thomas James Frank
MPhys
ORCiD: 0000-0003-4677-4055

A thesis for the degree of
Doctor of Philosophy

February 2025

University of Southampton

Abstract

Faculty of Engineering and Physical Sciences
School of Physics and Astronomy & Optoelectronics Research Centre

Doctor of Philosophy

Nanoscale Metamaterials Tailored for Optical and Mechanical Applications

by Thomas James Frank

Metamaterials have been exploited to show a number of exotic effects, in particular for longer wavelengths, from infrared to microwaves. Extending their response to shorter wavelengths requires structuring on the nanoscale which is made possible with increasing advances of fabrication techniques. The rigid pattern of metamaterials, however, meant that their response can only be observed for a narrow wavelength range. The aim of this project was to extend the functionality of metamaterials to manipulate visible and infrared light and to demonstrate wavelength tuneability. Utilising liquid crystals, with their attractive optical properties and easily controllable nature, was the main method towards achieving adaptive metamaterials. While typically the optical properties of liquid crystals are employed in applications, this work went beyond that and exploited their elastic properties. A liquid crystal layer, coupled to a mechanical metasurface, was shown to remove the limits of the stiction forces present at the nanoscale. New liquid crystal loaded metamaterials, made of nanostructured zigzag bridges, were fabricated and characterised to better understand the interactions taking place and to improve the functionality of future devices. The zigzag design was then explored separately in a project investigating its selective dependence on the spatial coherence of light. Computational modelling of the geometry was first completed and then compared with the experimental results. A large discrepancy between the experimental and modelled spectra for the zigzag metamaterial design was found, namely a split resonance being experimentally observed while the model predicted a single resonance peak. The split resonance was then successfully simulated for the case of incoherent incident light. In order to understand this feature further, variations of the zigzag geometry were fabricated and analysed. The final nanoscale design explored for investigating the optical properties of metamaterials included arrays of asymmetric slits. Optical activity upon reflection from a metasurface with equivalent, larger slits was demonstrated in the earlier work for microwave wavelengths. Samples with pairs of both symmetric and asymmetric slits were fabricated to obtain data from both reference and active samples. The presence of optical activity was then demonstrated for the asymmetric samples at optical wavelengths, in line with the theoretical predictions. The nanostructured metamaterials simulated, fabricated and experimentally characterised for this thesis, contribute to demonstrating the exciting potential of nanoscale metamaterials for photonic components and other groundbreaking technologies.

Contents

Declaration of Authorship

I declare that this thesis and the work presented in it is my own and has been generated by me as the result of my own original research.

I confirm that:

1. This work was done wholly or mainly while in candidature for a research degree at this University;
2. Where any part of this thesis has previously been submitted for a degree or any other qualification at this University or any other institution, this has been clearly stated;
3. Where I have consulted the published work of others, this is always clearly attributed;
4. Where I have quoted from the work of others, the source is always given. With the exception of such quotations, this thesis is entirely my own work;
5. I have acknowledged all main sources of help;
6. Where the thesis is based on work done by myself jointly with others, I have made clear exactly what was done by others and what I have contributed myself;
7. Parts of this work have been published as:

   Oleksandr Buchnev, Nina Podoliak, Thomas Frank, Malgosia Kaczmarek, Liudi Jiang, and Vassili A Fedotov. Controlling stiction in nano-electro-mechanical systems using liquid crystals. ACS nano, 10(12):11519–11524, 2016.

   Thomas Frank, Oleksandr Buchnev, Tamsin Cookson, Malgosia Kaczmarek, Pavlos Lagoudakis, and VA Fedotov. Discriminating between coherent and incoherent light with planar metamaterials. Nano Letters, 19(10):6869–6875, 2019.

Signed:..... Date:.....

Chapter 1

Introduction

1.1 Motivation and aims

Metamaterials are nano-patterned artificial media that can exhibit properties beyond those seen in natural materials. Their resonant response is mostly determined by the geometry and design of the core unit and the base material, thus can be induced by particular incident wavelengths. However, a number of practical applications require metamaterials that are capable of operating across a wider range of wavelengths. Creating metamaterial devices that are capable of tuning their operating wavelength is therefore of great interest. The patterned format of metamaterials has been shown to be well suited to consider hybrid systems, namely integrating metamaterials with soft matter or seminconductors to achieve adaptive response.

The aim of the experimental projects carried out for this thesis was to explore nanoscale, planar metamaterials for visible and near-infrared light manipulation, investigating the robustness of their fabrication on the nanoscale for tuneable metamaterial technologies. The projects undertaken included designing, fabricating and characterising metamaterials, applying external electric fields and LCs to achieve functional metamaterial systems.

Three different, experimental projects were pursued for this thesis and their main findings are captured in the following chapters: Chapter 2 on mechanical metasurfaces, actuated with voltage and hybridised with LCs; Chapter 3 on zigzag metasurfaces and their sensitivity to the spatial coherence of incident light and finally Chapter 4 on optical activity with metasurfaces. Each chapter is accompanied by a brief introduction to the project-specific concepts. This chapter focuses on the introduction to the main concepts of metamaterials, metasurfaces and a brief overview of LCs.

1.2 Artificial photonic materials (metamaterials)

Introducing the general concept of metamaterials is often done through the context of other, well known, and often, man-made material systems, namely photonic crystals [1]. The simplest example of a photonic crystal – a 1D photonic crystal – is a dielectric mirror, which is a stack of thin dielectric slabs. Its optical response results from Bragg diffraction and interference of light at the resulting interfaces and therefore it requires structuring on the scale of the order of one wavelength [2], as shown on Figure 1.1. There different versions of photonic crystals, including those in 2D and 3D, which are obtained by structuring in 2 or 3 mutually orthogonal directions.

The condition that applies in such structures, namely their periodicity (a) being larger than wavelength (λ), photonic crystals cannot be described as an effective media. While examples shown on Figure 1.1 demonstrate artificial photonic crystals, such structures also exist in nature, for instance, in the form of opals and beautifully coloured butterfly wings.

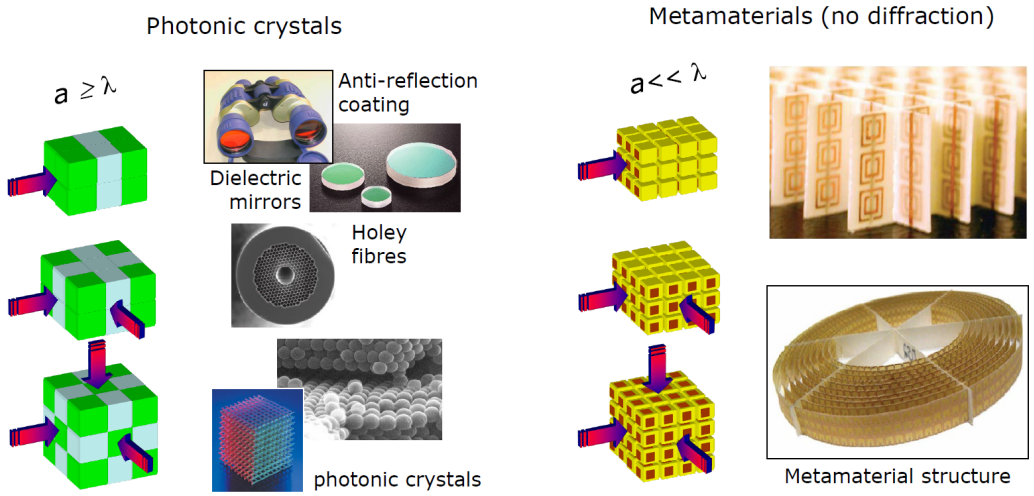

FIGURE 1.1: Examples of (a) traditional photonic structures exhibiting standard diffraction and interference versus (b) controlling light at sub-wavelength scale with metamaterials.

Metamaterials, on the other hand, are artificial by definition, as they are designed to interact with light in ways no natural materials can. More specifically, metamaterials are metal or dielectric composites that are structured on essentially sub-wavelength scale. They do not diffract, thus appearing homogeneous to the incident wave.

The exotic and often dramatic physics demonstrated by the metamaterial crystals is underpinned by resonant electromagnetic scattering of their unit cells, the so-called metamolecules, which can be made resonant in either one, two or three mutually orthogonal directions (Figure 1.1).

1.3 Metamaterials: basic principles and applications

Metamaterials are a class of nano-structured artificial media that have properties beyond those normally found in nature. For optical metamaterials these properties are achieved by creating materials which are periodically structured on the nanoscale, designed to interact with light in novel ways. The unit cells of these structures, called the metamolecules, are arrayed to form large active regions. Effects such as negative refractive indices [3], invisibility cloaks [4] and hyperlenses [5] can be observed by utilising different designs for the metamolecules. Negative refraction, for example, is essential for the development of the hyperlenses, a key component of optical imaging systems that can beat the famous diffraction limit.

Successes in achieving negative permeability and permittivity are paving the way to new phenomena including negative refraction which offers exciting applications in energy harvesting, sensors and image processing [6]. In particular, the opportunity to realise negative-index materials led to a rapid growth of a dedicated branch of metamaterials research. One of the first demonstrations was based on integrating arrays of conducting wires with arrays of split-ring resonators, exploiting the overlap between their frequency bands of negative permittivity and permeability. In this early work, the possibility for creating a perfect lens was also demonstrated [7]. Furthermore, particularly captivating was the demonstration of negative refraction at the optical communication wavelength of 1.5 μm using an array of pairs of parallel gold pillars, thus demonstrating the capability to fabricate metamaterials on the nanoscale [8] to manipulate light.

The design and engineering of metamaterials for particular response and wavelength relies on the consideration of their basic unit, which are called metamolecules, organised in a periodic arrangement in three dimensions and exhibiting a resonant response [9], acting as antennas. When an electro-magnetic field is incident, oscillating currents are generated in the individual metamolecules and electro-magnetic waves are re-radiated, combining to form the transmitted and the reflected, secondary waves.

The metamolecule patterns are typically metallic and fixed onto an insulating substrate. The resonances, λ_0, where strong scattering occurs, of such metamolecule antennas are determined by their sizes and design, and the materials used. By choosing appropriate pattern, the resonances can be tailored to a particular wavelength of interest. However, the limit on the metamolecule size means that for visible and infrared wavelengths, the fabrication challenges to produce precise patterns are more significant than, for example, the metamolecules for THz. Figure 1.2 presents some examples of metamaterial designs.

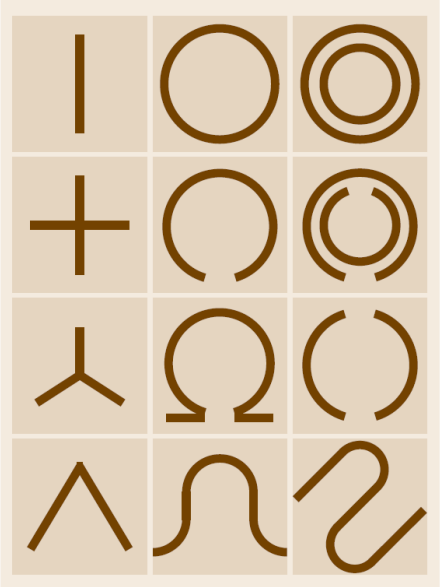

FIGURE 1.2: Typical examples of metamaterial designs.

As summarised in [10], for metamolecules driven by the external electro-magnetic field, their resonant frequency depends on the inductance L and capacitance C of the pattern:

$$\omega_0 = 2\pi f_0 = \frac{1}{\sqrt{LCs}} \tag{1.1}$$

The configuration of metamolecules-antennas, effectively operate as, a type of transmission line with resonant standing waves of conduction currents excited along the length of the structure.

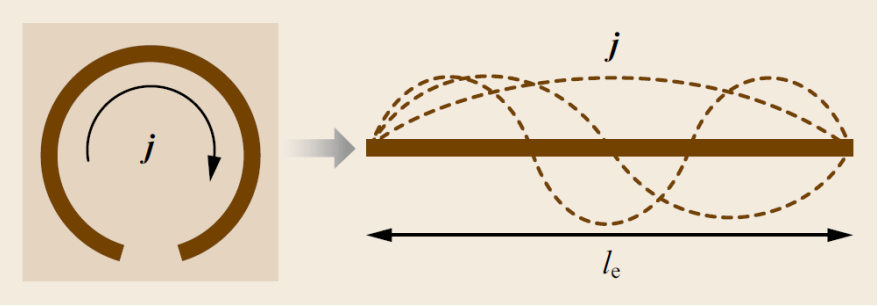

FIGURE 1.3: Resonant modes of metamolecules as standing waves.

The full analysis of the resonant mechanism is complex, but with some approximations, the resonance wavelengths of metamaterials can be understood through a mass-spring model. In the simplest case, the resonance wavelength of the metamolecule, treated as an antenna, is proportional to the effective path of an electron, which in conductors is typically proportional to the size of the antenna. This

direct relationship between the resonant wavelength and the size of the unit element is behind the need to match the structure of the metamaterial to the scale of the wavelength of incident light, hence the nanoscale patterning requirement for a response at visible wavelengths [11].

Following Lewin's theory [12], it can be shown that the resonant wavelength is also dependent on the dielectric permittivity, thus the resonance can be tuned either by the choice of materials or the dimensions and geometry of the core unit [13]. The representation as standing waves shown in Figure 1.3 provides a useful approximation and visualisation of resonances, with:

$$\lambda_0 \approx \sqrt{\epsilon}\frac{2l_e}{m} \tag{1.2}$$

where l_e is the total electrical length of the metallic design forming the metamolecule, ϵ is the relative permittivity of the dielectric medium that the pattern is embedded in, such as dielectric substrate, for example, and m is a positive integer.

The above analysis applies mainly to IR and longer wavelengths, where metals are good conductors. In the visible regime, the resonances of metamolecules are explained through plasmons.

The design of metamaterials is not the only important parameter. The electromagnetic properties of the metamaterials can then be described by effective parameters for the permittivity, ϵ, and permeability, μ, caLCsulated by averaging the local electromagnetic fields [14; 15]. Most natural materials have a magnetic permeability and electric permittivity greater than 0. By engineering the design of the metamaterial, values for ϵ and μ beyond these limits can be achieved. This can lead to novel optical properties, for example if a metamaterial is created with both ϵ and μ being negative, a so-called left-handed material, it will support backward propagating waves [16]. If ϵ and μ are equal then the metamaterial will be perfectly impedance matched with free space resulting in zero reflection at the free space and metamaterial boundary [9].

Most metamaterials only show their designed function for a narrow wavelength band. This leads to difficulties when utilising them as many applications require them to function for a range of wavelengths. Designing devices with the ability to tune their operating wavelength is therefore of great interest. Methods to achieve this include mechanically switching the geometry of the metamolecules [17], taking advantage of phase changes in materials [18; 19], and utilising LCs [20] which we will explore further in this project.

Over the past decade this concept of artificially engineered media, namely metamaterials, has revolutionised the field of optics, pushed the boundaries of microfabrication, and stimulated the development of novel characterisation

techniques [21; 22]. Recent demonstrations of anomalous reflection and refraction of light by metasurfaces opened another exciting chapter in optical engineering [23]. They can display novel effects or can be used to mimic bulk optical components such as lenses.

1.4 Metasurfaces

The focus of metamaterial research has shifted towards planar metamaterials, or the so-called metasurfaces. While metamaterials and metasurfaces are, in principle, two types of materials they are often used interchangeably, as will be used in this thesis. They are a class of low-dimensional (planar) metamaterials or in other words, 2D metamaterials and are typically formed by optically thin metal films periodically patterned on a sub-wavelength scale. Due to their planar nature they can take advantage of currently available fabrication techniques meaning they are less expensive and simpler to make when compared to bulk metamaterials which require complex multilayer technologies in terms of three-dimensional fabrication techniques.

In spite of their small thickness, metasurfaces interact strongly with light, which they can transmit, absorb or reflect without diffraction, effectively operating as optical media of zero dimension along the direction of light propagation. That sets planar metamaterials aside from resonant gratings of various kinds, photonic crystal slabs [21; 22] and perforated metal films exhibiting extraordinary optical transmission [24].

Metamaterials are fully compatible with the existing fabrication processes adopted by CMOS technology, and offer unmatched flexibility in the design and control of light propagation, exhibiting exotic electromagnetic phenomena and replacing conventional bulk optical components. In particular, metasurfaces have already enabled spectral [25; 26] and directional [27] filtering, asymmetric transmission [24; 25], polarisation control and analysis [28; 29], absorption enhancement [30; 31], imaging [32; 33] and sensing [34; 23] as well as being fully compatible with the existing fabrication processes adopted by CMOS technology.

Metasurfaces offer unmatched flexibility in the design and control of light propagation [23; 35; 36; 37; 38; 33] and demonstrating novel electromagnetic phenomena [23; 39; 28; 40]. Because of the sub-wavelength patterning they do not diffract, being effectively media of zero-dimension in the direction of light propagation.

The planar format of metasurfaces offers the benefit of their resonant response in terms of transmission, reflection or absorption for a relatively narrow range of frequencies, thus they can be regarded as an example of frequency selective surfaces, the concept developed the RF and microwave ranges [25].

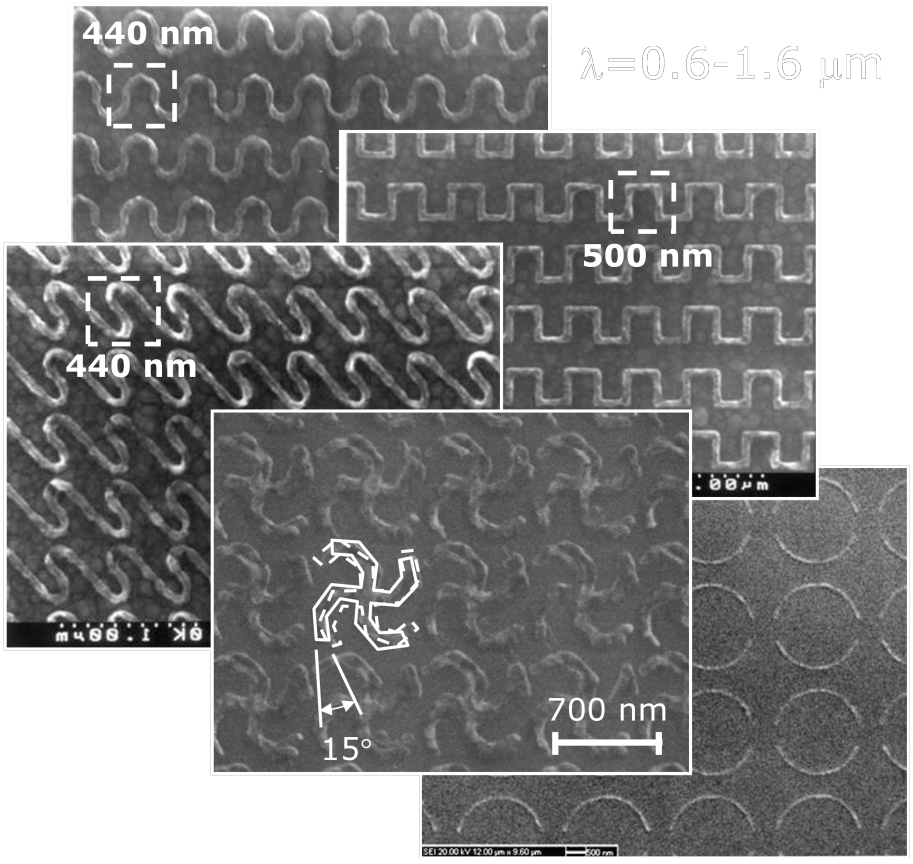

FIGURE 1.4: Different patterns of planar metamaterials (metasurfaces).

The concept of frequency selective metasurfaces has been exploited in this thesis in all three projects. In general, such metasurfaces consist of a two-dimensional lattice of metamolecules with periodicity lower than the incident wavelength. Metamolecules are typically metallic wires or slits of a particular design and dimensions, designed to have a resonance for a particular band of incident wavelengths and transparent beyond that range [10]. Figure 1.5 illustrates the main concepts behind such metasurfaces.

As shown on Figure 1.5(a) and (c), the metasurfaces can be formed by shaping metallic wires (so called positive metasurfaces) as well as through a complementary design of slits cut in the metal film. Such perforated apertures (negative metasurfaces). Their transmission and reflection spectra are complementary, following the Babinet principle, as shown in Figure 1.5(b) and (d) [10].

Similarly to the case of bulk metamaterials, the geometry of the shape determines the resonance frequencies. Furthermore, as such metasurfaces are also typically embedded in a thin, dielectric substrate, dielectric permittivity of such supporting medium also influences the resonant wavelengths.

For estimating the frequency selective metasurfaces, the expression for metamaterials (Equation 1.2) can be adapted to provide [10]:

$$\lambda_0 \approx \sqrt{\frac{\epsilon+1}{2}}\frac{2l_e}{m} \tag{1.3}$$

where l_e is the total electrical length of the shape of a metamolecule, pattern that forms the metamolecule, ϵ is the relative permittivity of the dielectric medium surrounding the metamolecules; m is a positive integer.

The difference between two expressions, (1.2) and (1.3), for metamaterials and metasurfaces, respectively, originates from different conditions in terms of surrounding media. In particular:

$$\sqrt{\epsilon} \rightarrow \sqrt{\frac{\epsilon+1}{2}} \tag{1.4}$$

The replacement of factors indicated in (1.3) stems from having two different media surrounding metasurfaces: the supporting dielectric and air on the other side. Following the treatment developed earlier for conducting wires embedded in to dielectric media, the effective permittivity is the average of dielectric substrate and of air. Such effective permittivity, namely $\sqrt{\epsilon}$, can be understood as the overall permittivity of a homogeneous medium that represents the layer of air and the dielectric regions of the wire, thus the field of the resulting electromagnetic wave will be partly in the dielectric and partly in air. The right-hand side of expression (1.3) therefore represents such effective permittivity of the conducting-dielectric system, estimated as an average between the permittivities of the dielectric and air as shown in [25].

Such analysis of resonant frequencies, with their transmission and reflection bandwidths for positive and negative metasurfaces only applies to thin samples [25], where the total thickness, d:

$$d << \lambda_0 \tag{1.5}$$

The designs of metamolecules could be made more complex and this created a rich field of metasurfaces of different designs, with either narrow or more broad transmission/reflection properties, in line with the needs of particular applications, as summarised earlier in this section.

Modelling the expected response typically involves COMSOL simulations and its libraries provide suitable underpinning code. They are based on consideration interaction between the incident electro-magnetic wave and using Maxwell equations to derive an appropriate version of wave equation. For metamaterials, in general, the unit cells (metamolecules) are much smaller than the incident wavelength, hence the

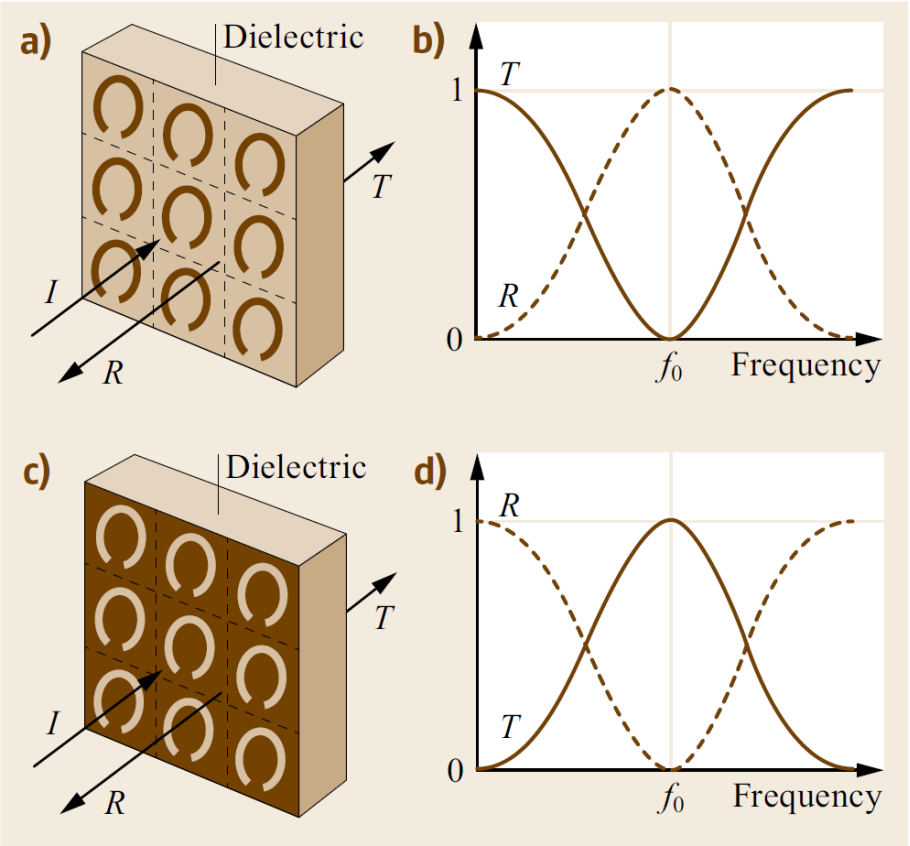

FIGURE 1.5: Principle of operation of frequency selective metasurfaces consisting of array of split-ring resonator metamolecules. (a) array of split-ring wires b) spectra of transmission (solid line) and reflection (dashed line) for wires c) array of split-ring slits cut in thin metal d) spectra of transmission (solid line) and reflection (dashed line) for split-ring slits [10].

whole material could be assumed as being homogenous [6]. Hence, the effective permittivity and effective permeability can be expressed as $\epsilon_{ff} = \epsilon_0\epsilon_r$ and $\mu_{ff} = \mu_0\mu_r$ with ϵ_{ff} and μ_{ff} being averaged over each metamolectules and do not depend on the wave vector, k or their values in the adjacent units, thus neglecting spatial dispersion.

Maxwell equations for metamaterials can be expressed [28]:

$$\nabla \times \mathbf{E} = -\mu_0\mu_r\frac{\delta \mathbf{H}}{\delta t} \qquad \nabla \times \mathbf{H} = \epsilon_0\epsilon_r\frac{\delta \mathbf{E}}{\delta t} \tag{1.6}$$

Taking the curl of both the left and the right sides and applying Ampère's Law, leads to the following wave equation for metamaterials [41]:

$$\nabla^2\mathbf{E} = -\epsilon_0\mu_0\epsilon_r\mu_r\frac{\delta^2\mathbf{E}}{\delta t^2} \tag{1.7}$$

If losses are negligible and ϵ_r and μ_r are considered as real, then the wave equation remains the same when both ϵ_r and μ_r are negative.

Exploring different options for ϵ_r and μ_r leads to some interesting effects, as discussed in [6; 41]. For example, when both ϵ_r and μ_r are smaller than zero, the direction of the refracted beam is on the same side of the normal as the incident beam, thus the metamaterial is regarded as having an effective negative refractive index. Hence, if both the effective relative electric permittivity ϵ_r and magnetic permeability μ_r magnetic permeability are negative, the value that can be associated with the effective medium's refractive index is:

$$n_{eff} = -\sqrt{\epsilon_r \mu_r} \tag{1.8}$$

Having an effective refractive index of a medium that is negative when both the real parts of the permittivity and permeability are negative is a general result, and can apply to different materials. However, careful consideration is needed in the case of materials where either the permittivity or the permeability is active. The rich opportunities to design new metamaterials led to the modelling of several exotic phenomena, initially for the microwave regime, including the impact of having asymmetric designs [10] and such robust modelling was essential to guide the experimental work carried out.

Given the constraints on the size of metamolecules, the fabrication of metamaterials is particularly challenging for the optical regime, as will be discussed in detail in the following chapters. However, in general, while technical challenges meant that high precision and a cleanroom environment was required for optical and near-infrared metamaterials, the flexibility and almost unrivaled prospect to manipulate local electric and magnetic properties led to the development of underpinning fabrication methodologies and the sharp increase in the demonstration of nanostructures with distinctive electromagnetic response to incident light. The other approach to address this challenge was to reduce the complexity related to bulk, three dimensional metamaterials by constraining them to thin planar surfaces, called metasurfaces. The fabrication approach also benefits from the experience and recipes from well known technologies such as computer chip, phase-array antennas and diffractive optics. Optically thin layers, structured on the sub-wavelength scale not only can influence polarisation or phase of light, but they can also be chosen from a wide range of materials with attractive electronic and optical properties, such as graphene, semiconductors or plasmonic metals. Therefore, the benefits and the exciting opportunities to explore new fascinating phenomena with prospects for further miniaturisation and high performance optical components mean that the effort devoted to fabrication methods has been paying off [42]

Apart from different shapes of metamolecules, there are also different options in the choice of supporting dielectric media, an example of such investigation with different media will be discussed in the next chapter, where LCs, instead of air, were surrounding a metasurface from one side. This project was among the recent effort of the world's leading metamaterial labs on implementing the idea of tuneable and active metamaterials, a generation of artificial photonic media with dynamically controlled optical properties. The latter is perceived as the next important stage in the development of the metamaterials, which should dramatically expand the range of their potential applications. One of the first proposals towards this goal was to combine metamaterials with nematic LCs.

1.5 Liquid crystals for tuneable metamaterials

LCs are molecules which exhibit phases of matter in between the basic solid and liquid phases [43]. These phases have some degree of orientational order and in some cases a degree of positional order, but are also able to flow like liquids. The different phases exhibited depend on the molecular structure, with some only having a single LC phase and others having multiple phases depending on their temperature. In the simplest case, called the nematic phase, the molecules tend to point in one direction even if they are flowing. The result of this preferred orientation is that nematic LCs can be described as anisotropic fluids, characterised by optical and dielectric anisotropy. Another more complex phase of LCs is the smectic phase, where the molecules are pointing in the same direction but are also organised in layers showing some long range positional order.

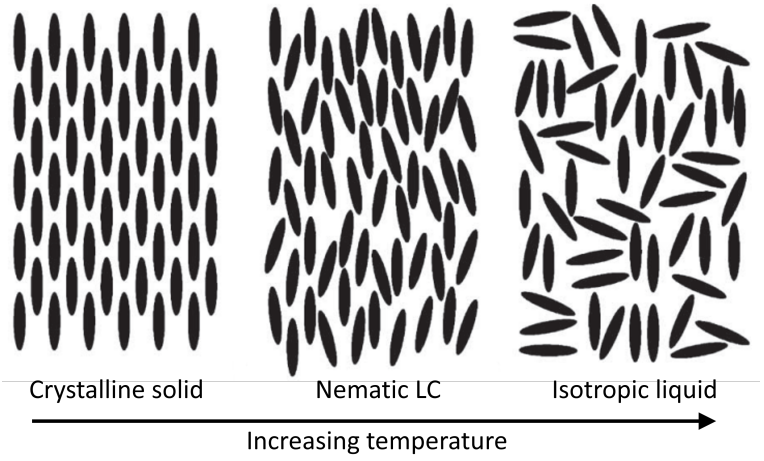

FIGURE 1.6: The phases of a nematic LC as temperature is increased.

The transition between the solid, LC and isotropic liquid phases is achieved through increasing the temperature, which reduces the degree of order. The materials exhibiting LC phases start with a high degree of order at low temperature when they

are solid and then with increased temperature turn into LC phases. First, for LCs that show this phase, there will be a more ordered smectic phase and then the less ordered nematic phase as the temperature increases. Finally, at the so called clearing temperature, the material will turn into an isotropic liquid. This change of order and of material parameters that is induced and controlled by temperature adds to the versatility of LCs, explored both for research and practical applications.

In this work, only nematic LCs were considered, thus the discussion of LCs material parameters and their influence on metallic structures will only consider this phase. Therefore, when LCs will be mentioned, this means nematic LCs.

There are several nematic LCs that exhibit high optical birefringence in the visible range. Those with high birefringence, such as 5CB which will be discussed in the next chapter, retain sizeable birefringence even in the terahertz range, namely 0.14 around $2THz$ [44]. LCs are easily controlled by temperature, light, electric and magnetic fields. They have also arguably the largest and most broad-band optical nonlinearity. They share properties with both liquids and crystalline solids, appearing to move like a liquid but show an ordered nature like that found in crystals upon closer investigation. The structure of these ordered phases depends on the type of LCs and on external properties such as temperature and external fields [43]. One of the simplest and most useful of these is the nematic phase where the molecules behave like rods with no positional order but with the molecular rods all pointing in the same direction described by a vector called the director. Light passing through such anisotropic materials experiences a different refractive index depending on its polarisation and propagation direction. There are two possibilities, n_o and n_e. If the direction of propagation is the same as the director then no is experienced by all polarisations of the light. If the light propagates perpendicular to the director then light with polarisation parallel to the director will experience n_e while the light with polarisation orthogonal will experience n_o. The director can be influenced by external forces such as magnetic and electric fields. This effect is utilised in LCs displays to vary the intensity of transmitted light. One example of this is the twisted nematic cell in which the LCs is sandwiched between two glass planes each coated with an aligning layer with a transparent electrode underneath. This set up is shown in Figure 1.7.

The electrodes, typically made from Indium Tin Oxide, allow an electric field to be placed across the cell. The aligning layers consist of a rubbed polymer such as polyimide which causes the local LCs molecules to align with the rubbing direction. For a twisted cell the rubbing directions of the top and bottom aligning layer are perpendicular to each other causing the LCs molecules to form a helix like structure with a 90° twist between the 2 layers. The last part of the device is a set of crossed polarisers on the outside of the glass planes which are aligned parallel to each of the alignment layers. Light passing through the device will be linearly polarised by the first polariser, then have its polarisation rotated by 90° as it propagates through the

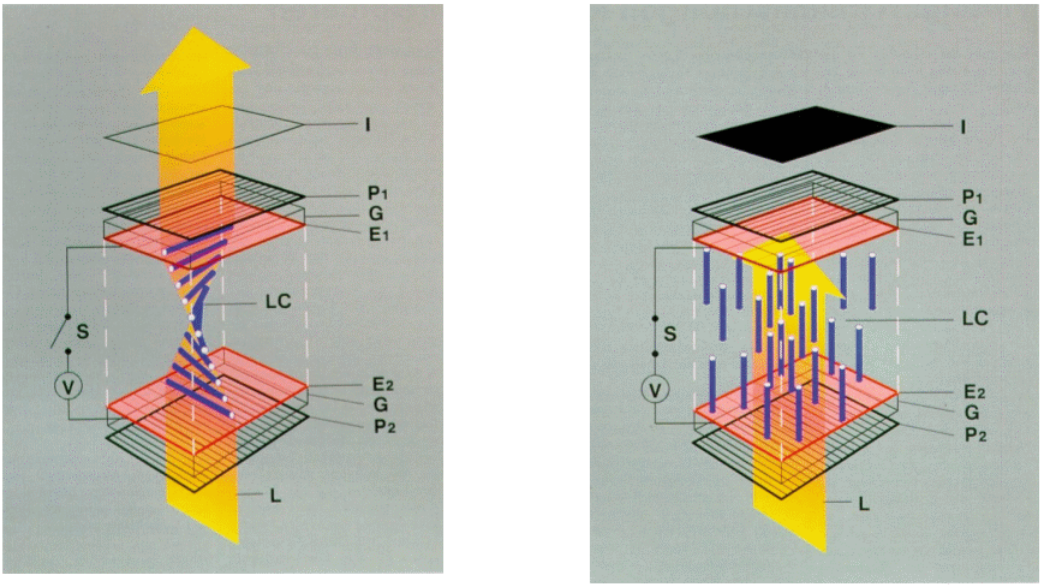

FIGURE 1.7: Twisted nematic LCs cell in ON state, left, and OFF state, right. P, G and E are the polarisers, glass and electrodes respectively.

LCs [45]. The light can then pass through the second polariser without being absorbed leading to the 'on' state of the device. When an electric potential is placed across the cell the LCs molecules will align in the direction of the electric field, destroying the helix like structure. Now the polarisation of the light will not be rotated and the light will be absorbed by the second polariser creating the 'off' state for the device.

There have been a number of works on LCs-loaded metamaterials since the emergence of the field. Early work included radio-frequency and microwave metamaterials controlled by electric and magnetic fields [46; 47], followed by Near-IR metamaterials controlled with temperature [48], then by near-IR metamaterials controlled with light, namely UV light [49] and finally near-IR materials controlled by electric field [50; 51; 20].

It has been shown that metasurfaces can be used to replace many of the components of a LCs cell. Buchnev et al. [51; 20] demonstrated this by fabricating a cell with one half consisting of the traditional assembly of a glass substrate, polariser, ITO electrode and polymer aligning layer, as shown in Figure 1.7, and the other half consisting of a gold metasurface on a glass substrate. The metasurface was formed of zigzag shaped gold nanowires which effectively acted as the polariser, electrode and aligning layer for the cell.

Using LCs to tune the operating wavelength of negative permeability [47] and negative index [52] metamaterials has been experimentally shown in the microwave regime. Tuning at optical wavelengths has been demonstrated relying on the LCs phase change from nematic to isotropic as the temperature is increased [48]. This

tuning will only allow two discrete values to be attained in contrast to electrical tuning which will allow for a near continuous range of values.

The ability of LCs for tuning metamaterial devices operating at optical and near-IR is impeded due to the surface anchoring of the LCs molecules [53; 54]. To efficiently tune such devices, the LCs must be able to switch in the vicinity of the metamaterial structure where the plasmonic fields are strongest. The surface anchoring of the molecules renders the region of the LCs in contact with the substrate inactive. One solution to this problem was demonstrated here, at the University of Southampton, by Buchnev et al. [20]. A metasurface was fabricated from gold deposited on a SiN membrane using a focused ion beam. During the fabrication the focused ion beam cut through the supporting membrane as well as the gold leaving zigzag shaped gold nanowires suspended on SiN bridges. LCs added to this metasurface have no surface to anchor to and are therefore free to move in the plane of the metasurface when a voltage is applied between the wires of the device. This allowed the spectral tunability of the sample to approach the theoretically predicted limit of 9%.

All the methods summarised here, aiming to enhance functionality of metasurfaces, rely on strong optical birefringence from the LCs. Although changes of the refractive index attainable in LCs are hysteresis-free and large, the extent of tuneability achieved for metamaterials in this way proved relatively modest for widespread and practical applications. Therefore, in this thesis, the main focus will be on expanding the area of hybrid metamaterials and their functionality further, by engaging the elastic response of nematic LCs.

Chapter 2

Elasto-Mechanical Coupling for tuneable Liquid Crystal Metamaterials

The current effort in the field is being focused on implementing the idea of active and tuneable metamaterials (MMs), a generation of artificial photonic media with dynamically controlled optical properties. The latter should enable to dramatically expand the range of the potential applications of the MMs making them the fundamental base of future photonic devices [55].

In this chapter, a new generation of non-linear, dynamically tuneable artificial material systems is demonstrated. It belongs to a class of optical metamaterial hybrids that exploit elastic coupling of liquid crystals (the hybrids' functional component) with the mechanically re-configurable fabric of the metamaterial host. Thus, the concept of non-linear tuneable metamaterials is taken to the next level by adopting the best of the indirect and direct control methods and eliminating their shortfalls with a single hybrid approach.

Following on the earlier work on hybrid LC-metamaterial, where the elastic forces on anisotropic media such as LCs was used to prevent the detrimental effect of stiction, the results of this experimental study discussed here focuses mainly on exploring if LCs could restore mechanical actuators damaged due to stiction.

2.1 Hybrid approach to controlling metamaterials: exploiting elasto-mechanical coupling

Developing artificial photonic media with dynamically controlled optical properties has become one of the key stages in the metamaterial research, as it should enable the creation of smaller and more efficient photonic structures and devices, dramatically expanding the range of metamaterial applications [55; 56]. The dynamic control of a metamaterial can be implemented using generally two approaches – the direct approach, by physically modifying (though often irreversibly) the fabric of the metamaterial through either mechanical deformations [57; 58] or the use of MEMS/NEMS (micro/nano-electromechanical systems) -based actuators [59; 60]; and the indirect approach, by altering optical properties of the metamaterial's host matrix or substrate/superstrate, which features naturally available functional materials (e.g. non-linear, phase change or gain). Among functional materials liquid crystals (LCs) possess arguably the largest broadband optical non-linearity and externally controlled birefringence, which has made LCs one of the first and most popular ingredients exploited by indirectly-tuneable metamaterial designs [47; 61; 53; 56; 57]. In particular, earlier work in the group demonstrated efficient spectral tuning of LC-MM system in the optical part of the spectrum, which was achieved by reorienting LC molecules in a specially designed nano-structured hybrid using in-plane electric field [20].

In all reported designs of tuneable LC-MMs the role of the liquid crystals has so far been limited to acting as a macroscopic dielectric environment with controlled optical anisotropy. Although changes of the refractive index attainable in liquid crystals are hysteresis-free and large, the extent of spectral tunability demonstrated in LC-MM hybrids is still too modest for most of practical applications. For example, the maximum value of the birefringence of E7 ($\Delta n_{max} = 0.225$) would correspond to a spectral shift of less than 15%.

At the micro and nano scale, devices experience a range of effects that are not seen in larger components. One of these that can be very problematic for mechanically switching metamaterials is stiction. This occurs when a mechanical actuator comes into contact with another surface and becomes stuck as the adhesive forces, such as capillary, Van de Waals and electrostatic forces, exceed the restoring force of the actuator. This becomes more problematic as the size of the device decreases due to the restoring force, related to the volume, becoming weaker compared to the adhesive forces, related to the surface area. For functional devices that rely on mechanical switching, a method to mitigate or even control stiction would be extremely useful. Furthermore, in reality, the tuning range is reduced by at least a factor of two due to the presence of a supporting dielectric substrate, which prohibits the complete immersion of metamaterial framework into the bulk of LC. Moreover, the efficiency of tuning may be lowered even further as a result of strong anchoring of LC-molecules to

the surface of the metamaterial; it renders few tens of nanometers of LC adjacent to the surface as inactive (which is particularly detrimental for nano-structured metamaterials designed to operate in the near-IR and visible spectral domains).

LCs are optimum materials to overcome these limitations and take full advantage of the available LC control mechanisms, involving temperature, light, electric and magnetic fields, and exploiting the elastic properties of liquid crystals. In the new section, it is shown how LCs, when coupled to the fabric of a re-configurable photonic metamaterial, can efficiently modify the character of its nanoscopic mechanical actuators, which then transform elastic distortions of LC into changes of the metamaterial optical properties. Furthermore, strong surface anchoring of LC-molecules turns here into an advantage: it ensures robust elasto-mechanical coupling between the metamaterial framework and LC, whilst eliminating the major shortfall of mechanically re-configurable systems, namely their susceptibility to electrostatic/capillary stiction resulting in permanent structural damage [62; 63].

LC-MM structures discussed here, with elastic forces preventing stiction, are directly relevant to NEMS (nano-electro-mechanical systems), which are integrated miniature devices that combine electrical and mechanical components at the nanoscale. They have demonstrated great potential for a wide range of applications including nanoactuators and sensors [64; 65; 66], electromagnetic detectors [67; 68; 69], optical switches and relays [70; 71; 72] and, recently, reconfigurable metamaterials and plasmonic devices [73; 74; 75; 76; 77]. The reliability of NEMS (as well as MEMS) faces challenges related to issues such as “stiction”, undesired adhesion between the relevant surfaces of the mechanical components, which typically leads to their irreversible damage [78; 79].

Stiction takes place when surface adhesion forces, such as capillary, Van der Waals, electrostatic forces or their combinations, are stronger than the mechanical restoring force from an actuator. The methods to prevent stiction have been developed and are typically applied at the device fabrication stage, for example, by changing the surface hydrophobicity or by eliminating liquid-vapor interfaces through supercritical fluid, freeze-drying, or dry release methods [80; 81; 82]. However, such approaches sometimes fail, for example, due to changes in ambient conditions or during routine operation of the device when its mechanical components come into close contact with each other. Therefore, there are ongoing efforts to tackle such undesired effect, including surface treatment and coatings [83; 84; 85], adapting the structure of designs of cantilevers and/or contact electrodes [86; 87]. Stiction, while posing a significant issue in microscale electromechanical systems (MEMS) [81], creates more major problems for the reliability of NEMS, with their larger surface-to-volume ratio. Furthermore, the stiction-preventive methods developed earlier and proven effective for MEMS [84; 88] are not easily applicable to NEMS, with the reduced size of these devices. Therefore, the alternative method proposed here, using LCs with their

fluidity accompanied by strong elastic forces offers an attractive solution to stiction issues.

The structures were first exposed to an AC voltage to check for any short circuits without moving the nanobridges and then to a DC voltage. It is worth noting that DC driven LC devices can suffer from long term stability issues. Charge carriers and ions can be generated with longer exposure to DC voltage and they can accumulate close to the conducting surfaces and electrodes, effectively screening the applied electric field. Such negative effects can be limited if LCs with low ionic content are used and the structures are refreshed with the application of AC voltage. This particular aspect was not studied in detail as part of this thesis, but it would offer an interesting extension to the work presented here.

2.2 Background to experimental LC - Metasurfaces

From the previous work carried out in the group by Buchnev et al. [20], where the already tested zigzag metamaterial design used in the past to implement active control via volume and in-plane switching of liquid crystals, a new metasurface was designed and fabricated [89]. The changes from the previous metasurface can be seen in Figure 2.1 below. Joining the project [89] in its final stages, I assisted with final tests, additional analysis and discussions. The methodology and the experiments carried out in [89] are presented here in detail as they were followed for the fabrication and the experiments discussed in this chapter.

The zigzag geometry had each metamolecule consisting of a single chevron shape. This shape was chosen following earlier work in the microwave regime, where wave like structures were fabricated and showed distinct resonances. For the optical and near-infrared regime, the nanoscale fabrication is more challenging and sharper, rather than curved endings of the structures, are more feasible to achieve. In the first work on such "sharp" zigzag structures [20] it was successfully shown that they act efficiently not only as an alignment layer, as electrodes, but also a polariser in MM-LC cells. Therefore, the zigzag pattern was retained for the further studies.

As Figure 2.1 shows, the metasurface, while retaining the shape, was modified slightly and consisted of fully suspended on dielectric nano-bridges. This new metasurface was designed to deform when a voltage was applied to the electrodes. The wires were arranged in pairs instead of the alternating electrode pattern used before, such that odd and even pairs were electrically disconnected from the opposite sides of the gold frame. Straight sections were added on to the ends of each wire to increase its flexibility and those straight extensions on each side of the nano-bridges ensured uniform displacement of the zigzag sections in the plane of the structure. The bridges were cut in a $50nm$ thick low-stress SiN membrane using focused ion beam. In more

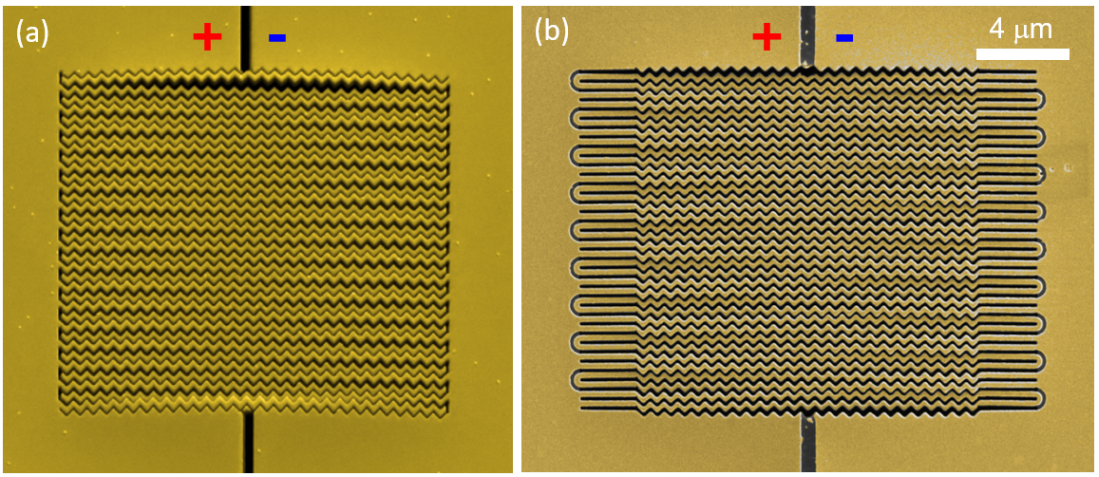

FIGURE 2.1: Comparison between the metasurface [20], (a), and the metasurface used to investigate stiction effects [89].

detail, the metasurface was fabricated by milling, with a focused ion-beam, a $50nm$ thick gold film, which had been sputtered beforehand on a $50nm$ thick silicon nitride membrane. The milling completely removed parts of the membrane in the gaps between zigzag nano-wires, yielding a wire grid that was fully suspended on silicon nitride bridges and could mechanically flex in the plane of the structure. The metamaterial structure was configured to operate in the near-IR, exhibiting a plasmonic resonance as a peak in the transmission spectrum at around $0.8\mu m$.

The nano-wires were grouped in pairs with the odd and even pairs being connected to the electric potentials of opposite signs, so that the resulting electrostatic attraction/repulsion between the neighbouring wires would trigger their lateral displacement. That allowed us to apply a potential difference between the pairs, making sure that electrostatic forces acting on each and every nano-wire were not balanced. The resulting combination of repulsion and attraction triggered lateral displacements of the supporting nano-bridges. Hence, when a voltage was applied the wires were attracted together in pairs due to the electrostatic attraction and repulsion between them. In this way, a metamaterial could be made re-configurable.

The metamaterial structure was infiltrated with a nematic liquid crystal 5CB (Merck) applied to the surface of the sample using a drop-casting method. The choice of 5CB (versus other nematic LCs) was done for the convenience of working with this LC, which has the lowest clearing temperature among widely available nematic liquid crystals ($35^{\circ}C$), relatively low viscosity, and weak optical anisotropy ($n_o = 1.520$, $n_e = 1.681$, $n_{iso} = 1.574$ at $\lambda = 1\mu m$).

For the purpose of optical measurements, the drop was squeezed by a glass cover slide, yielding a thin, optically uniform LC layer. The glass slide was coated with a $20nm$ thick film of non-rubbed polyimide, which ensured both parallel alignment and weak anchoring of LC molecules at its surface. As observed in earlier work [51], a

zigzag patterned metamaterial can act as a polariser, an electrode and as an alignment layer. For the devices studied in this thesis, planar alignment of the LC on the metamaterial bridges was also observed so there was no need to rub the polyimide layer to ensure planar orientation. As a benefit, the weak anchoring from the non-rubbed polyimide provides extra freedom of orientation for the LC well above the metamaterial structure.

The thickness of the LC layer was set to $2\mu m$ by using dielectric spacers placed between the glass cover and gold film. To promote the infiltration of the LC into the metasurface, the temperature of the sample was maintained above the clearing point of 5CB for about 10 minutes.

The optical response of the metamaterial sample was characterised in transmission at normal incidence using linearly polarized light. The polarisation was set either parallel or perpendicular to the wires of zigzag nano-grid. Transmission spectra were collected in the range $0.7 - 1.9\mu m$ with a spectral resolution of $0.1\mu m$ using a microphotospectrometer.

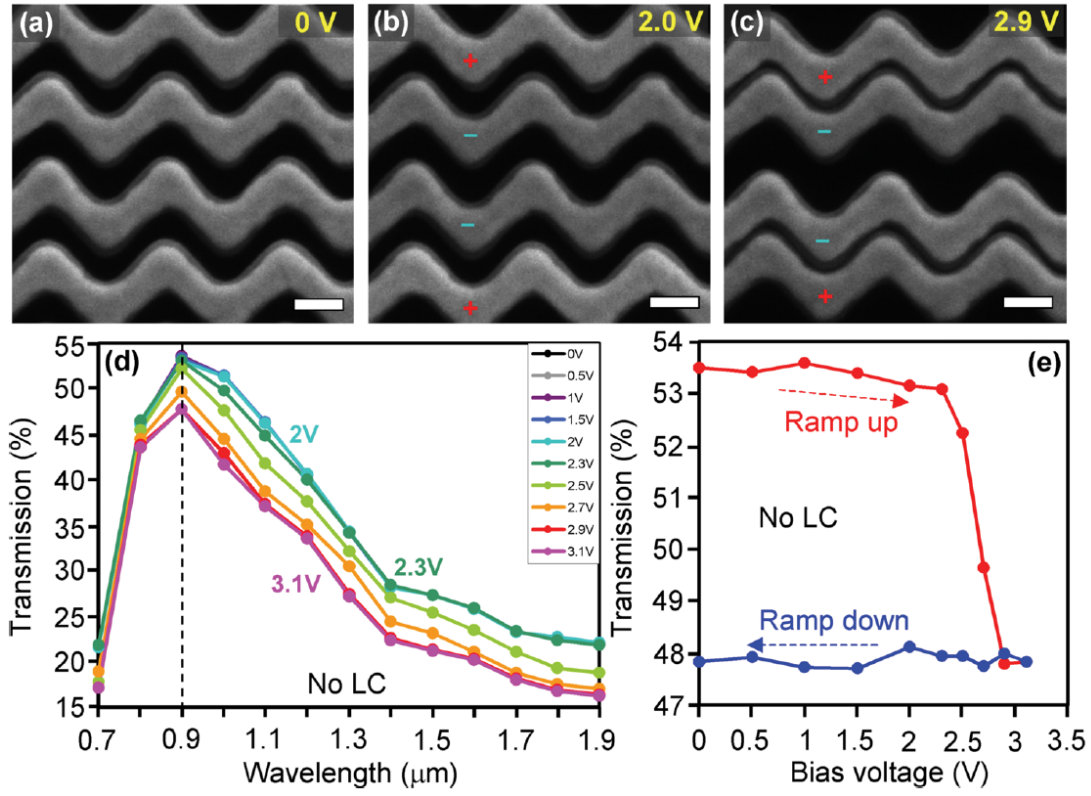

FIGURE 2.2: (a)-(c) SEM images of the nanowire metasurface captured as voltage was increased. Scale bars corresponds to $200nm$. (d) Transmission spectra of the metasurface as voltage was increased. (e) Plot of transmission at $0.9\mu m$ as voltage was increased and then decreased.

The failure of the reconfigurable metamaterial due to stiction was first observed directly under a scanning electron microscope. As the voltage was increased, the

potential of each wire could be seen in the SEM image as a change in the brightness. The wires remained in place until the voltage reached the critical value of $2.7V$, when they quickly snapped together in pairs. Once the wires were touching the voltage was decreased, but they remained coupled in pairs due to the adhesive forces between the wires being greater than the restoring force for the deformation. This effect, as described before, is called stiction. The SEM images of this process are shown in Figure 2.2.

The same experiment was conducted with a new sample while the spectral response of the metasurface was observed with a microphotospectrometer. The transmission of the sample was seen to remain stable with the increasing voltage until, as expected from the previous experiment, it sharply reduced at $2.7V$. Above this voltage the transmission spectra showed no changes. The spectra are shown plotted in Figure 2.2(d). To make this easier to view the transmission value at the peak of each spectrum was plotted against the applied voltage. This is shown in Figure 2.2(e). We can see the sharp fall in the transmission value as the wires couple together and that as the voltage was ramped back down the transmission remained at its final value. This showed we could verify optically when stiction had taken place.

A new set of samples was then fabricated and infiltrated with 5CB, a liquid crystal. The sample was observed under the microphotospectrometer as before. Due to the presence of the LC, the transmission resonance of the sample was red-shifted by approximately $200nm$ and the voltage required to actuate the sample was increased from $2.7V$ to $6V$. This is because of the increased electrical permittivity from the LC. First the sample was observed with the LC in its disordered isotropic phase. This was done by heating the sample above the clearing point of 5CB, $35°C$, using a heated stage for the microscope. Figure 2.3(a) and (b) show the response as the voltage was applied. A similar response to that seen with the dry sample was observed with the transmission at the peak of the resonance sharply falling around $6V$. Above this the transmission spectrum remained the same and as the voltage was ramped down the sample remained in this final state. This showed that the bridges had become stuck due to stiction.

The difference between isotropic and nematic LC effect could be understood through an increase in the restoring force acting on the nanowires, such additional originating from the elastic bend and splay deformation of the LC in the area between and directly above the oppositely charged wires [89]. The force acting on the wires is much stronger in the nematic than in the isotropic phase. This is because the force results from the local distortions of the LC interacting with the large scale nematic order present in the bulk of the LC. This force is not confined to the case where the wires are closest together, but during their entire range of motion, acting to cushion their movement.

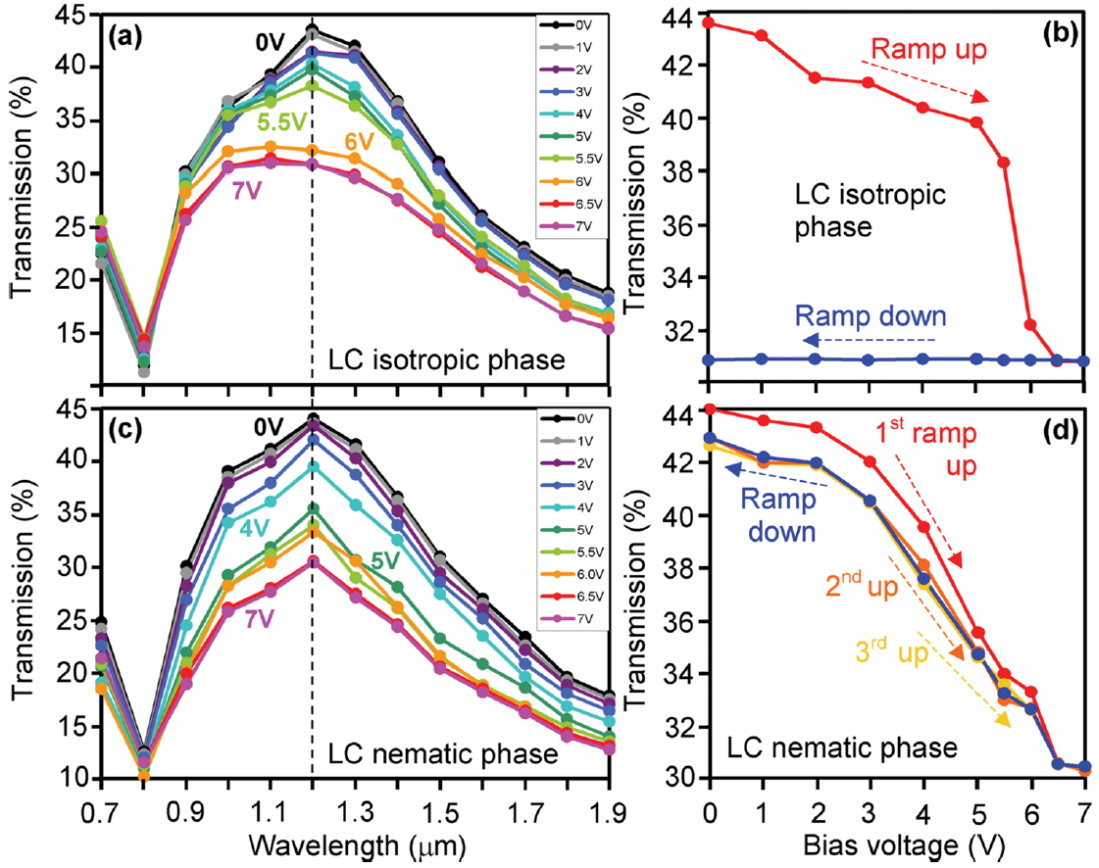

FIGURE 2.3: (a) Transmission spectra with isotropic LC as voltage increased. (b) Transmission at 1.2μm as voltage was ramped up and down with isotropic LC. (c) Transmission spectra with nematic LC as voltage increased. (d) Transmission at 1.2μm as voltage was ramped up and down with nematic LC.

The wavelength of peak transmission for the case of a sample with the isotropic LC shifted to a lower wavelength and the peak became less pronounced as the applied voltage was increased. The exact mechanism behind these trends is still not fully understood. There are many different contributions stemming both from the material properties of the LC as well as from the structure of the flexible nanobridges changing as they become coupled. Additionally the LC can become locally aligned due to the applied electric field while remaining disordered away from the metasurface. To investigate these factors and to fully understand the interplay between them would require a complex simulation model to be created which is outside the scope of this project.

While the application of LCs showed that stiction could be avoided, the aim of the further study pursued for this thesis was whether the application of LCs after stiction took place could reverse the damage and free up the nanobridges.

2.3 Experiments on zigzag metasurfaces for preventing irreversible damage

This previous study led to the question and idea whether LCs in nematic phase could be used to repair damaged nanobridges by separating them after stiction had occurred or whether prior infiltration was required for the observed effect. This required tests on multiple, pristine metasurface samples to check the repeatability and universality of the stiction effect.

The fabrication process of metasurfaces for this thesis followed the procedure pursued for [89]. With the assistance of Dr Buchnev, six new metasurfaces were produced. The fabrication is a very delicate process hence the need to fabricate multiple metasurfaces, with the aim of selecting those of the best quality. They were fabricated together on the same, large substrate and after inspection, only two were selected for further study. These 2 samples were electrically isolated by cutting wide strips in the gold with the FIB. There were 4 external connections onto the membrane allowing each sample to be investigated individually.

These two samples were then observed with the microphotospectrometer as voltage was applied with the aim of more detailed characterisation of the spectral response when the stiction effect occurs. The results of this were not as expected so the samples were viewed with the SEM to inspect for any problems. This showed that both samples had sustained major damage, most likely from electrical short circuits where some gold had not been fully removed. This led to excess heating of the nanobridges resulting in large deformations and some gold being vaporised. SEM images of other samples with similar damage are shown in Figure 2.4.

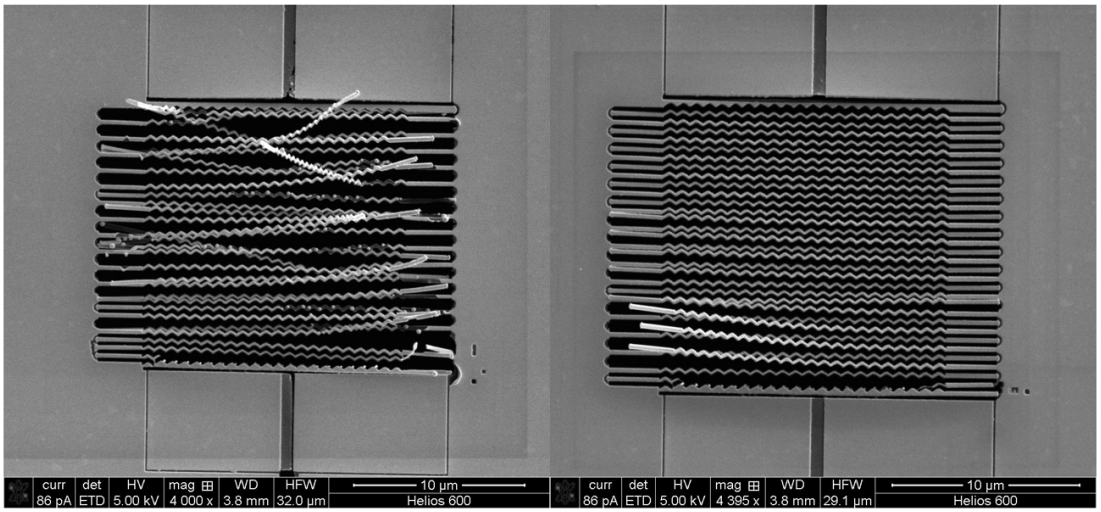

FIGURE 2.4: SEM images of two samples after damage from electrical problems. Scale bars, shown at the bottom of the SEM images, are $10\mu m$

2 new samples were fabricated on the same membrane. These were the same design but with slightly reduced overall size to ease the fabrication process. A zoomed out SEM image of the membrane is shown in Figure 2.5. The tracks cut in the gold can be seen with the 2 old damaged samples in the center and the other rejected samples. To connect the new samples to milled track in the gold must be bridged. This was done by depositing a small track of platinum using a gas injection system.

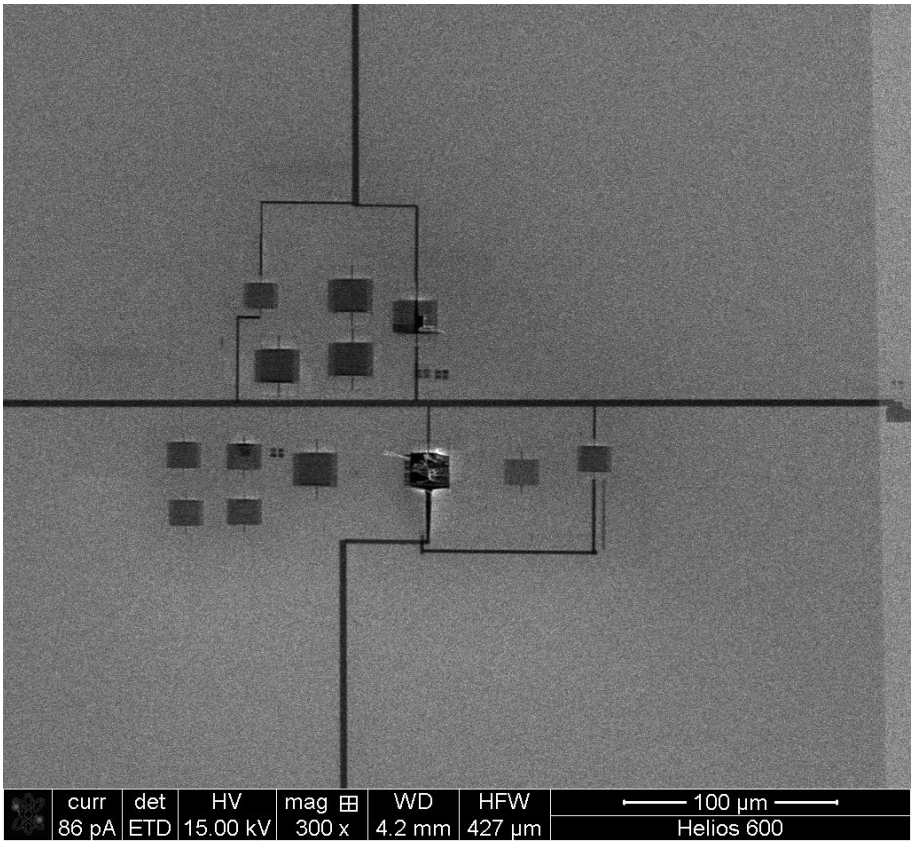

FIGURE 2.5: Zoomed out SEM image of the samples.

2.3.1 Spectra response of metasurfaces with applied voltage

Our two new metasurfaces were then observed with a microphotospectrometer, using the same method as in [89]. The aim was to investigate how the spectra are affected by the, effectively, changing structure and pattern of the metasurface.

In order to capture in more detail, the relevant differences in the spectra, the whole spectrum was collected from $400nm$ to $2000nm$, although for the wavelengths below $600nm$, the spectra are dominated by the absorption of gold. As shown in the following figures, the spectra are rather complex for such zigzag membranes, with the actual resonances being quite broad and does not consist of a single, resonance peak. Indeed, with incoherent illumination from the spectrometer, the broad resonance peak appears to be split, with a dip in the middle. The investigation of this feature was

pursued in a separate project and is covered in Chapter 3. Here, for the purpose of the analysis of the change in spectra/resonance due to applied voltage, the comparison between transmission at different voltages was carried out for a wavelength at which the changes in transmission were the largest.

Figures 2.6 and 2.7 presents the spectra collected for Sample 3, for voltages increasing from $0V$, through $2V$, then $3V$ and back to $0V$.

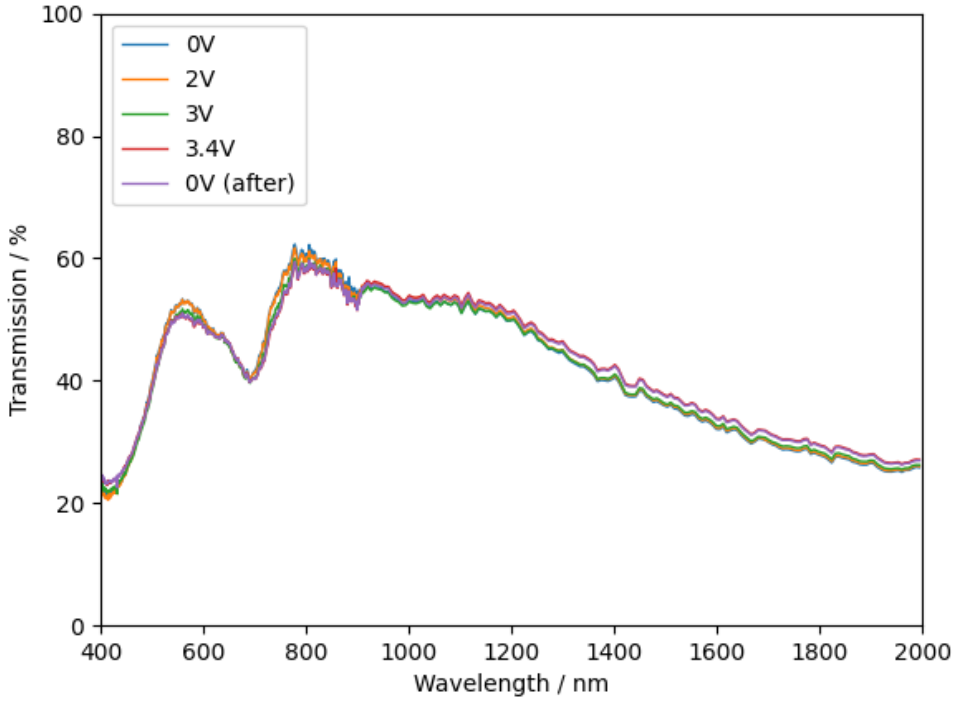

FIGURE 2.6: Transmission spectra of Sample 3 metasurface measured at increasing voltage starting from $0V$ to $3.4V$ and then back to $0V$.

As shown in Figure 2.7, the spectra for the initial $0V$ and $2V$ are closely overlapping, with little difference between them, indicating that up to $2V$, the nanobridges are only slightly deformed from their initial state. There is evidence of stronger deformation at $3V$ and then again at $3.4V$, suggesting that mechanical reconfiguration becomes noticeable around that voltage. Finally, reducing voltage to $0V$ makes no obvious difference to the spectra – they remain approximately the same as for $3.4V$, thus confirming the results from the SEM images, that the nanobridges experienced stiction at $3.4V$ and remained attached to each other even if the voltages is switched off.

Figure 2.8 shows an example of the same measurement for Sample 4, where a larger range of deformation was observed for voltages from $0V$ to $3.9V$ and then back to $0V$.

The comparison between spectra of the two samples provided some important insight, confirming the need to test multiple samples.

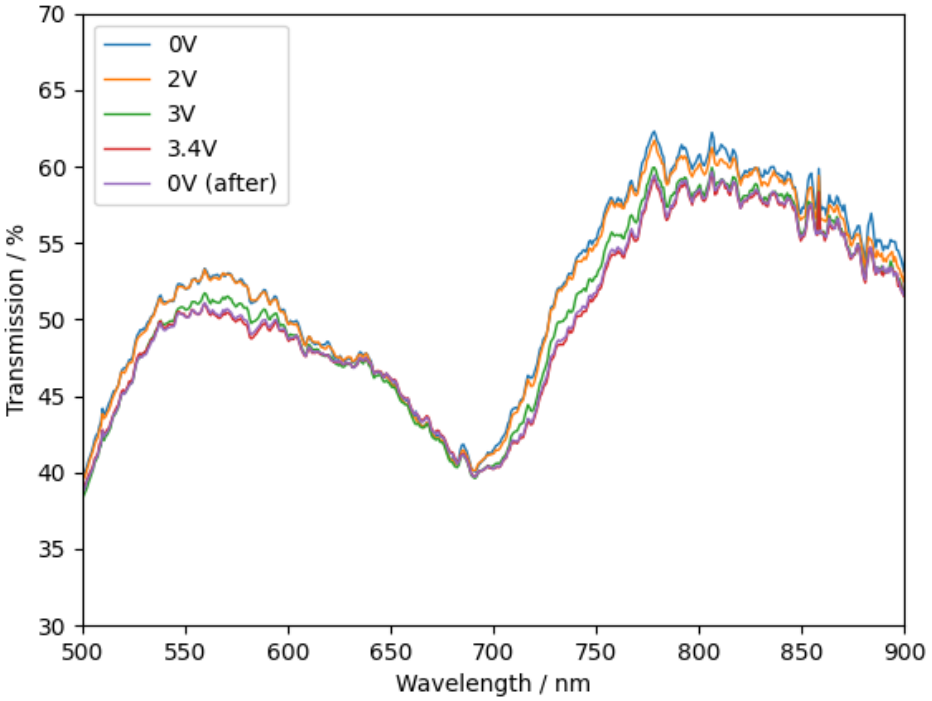

FIGURE 2.7: Zoomed in transmission spectra of Sample 3 metasurface measured at increasing voltage starting from $0V$ to $3.4V$ and then back to $0V$.

In Sample 3 spectra at $0V$ before and after the voltage was applied were noticeably distinct. The spectra Sample 4 for such case showed a somewhat different trend. While the metasurface does not recover completely to the initial state, the blue and black curves (at $0V$ before and after higher voltage was applied) overlap more closely than in the first sample. Furthermore, the trend in the changes in transmission with applied voltage, increasing to $3.9V$, while evident does not follow the same route as in Sample 3 nor does it follow what was observed in [89].

2.3.2 SEM images of fabricated metasurfaces actuated with electric field

Following the measurements using the microphotospectrometer the metasurfaces were viewed again under the SEM to verify that a change had occurred. All of the wires had coupled together on sample 4 but 2 pairs of wires remained unstuck on sample 3. Figure 2.9 shows sample 3 with $3V$ applied. The electrical potential can be seen on the wires as a change in brightness.

As seen in Figure 2.9, most of the nanobridges are in direct contact. The voltage was increased in steps to $3.7V$ and then switched off. Figure 2.10 shows SEM images of one of the unstuck pairs as the voltage was varied. The zigzags can be seen to couple together at $3.7V$ and remain stuck once the voltage was reduced to $0V$.

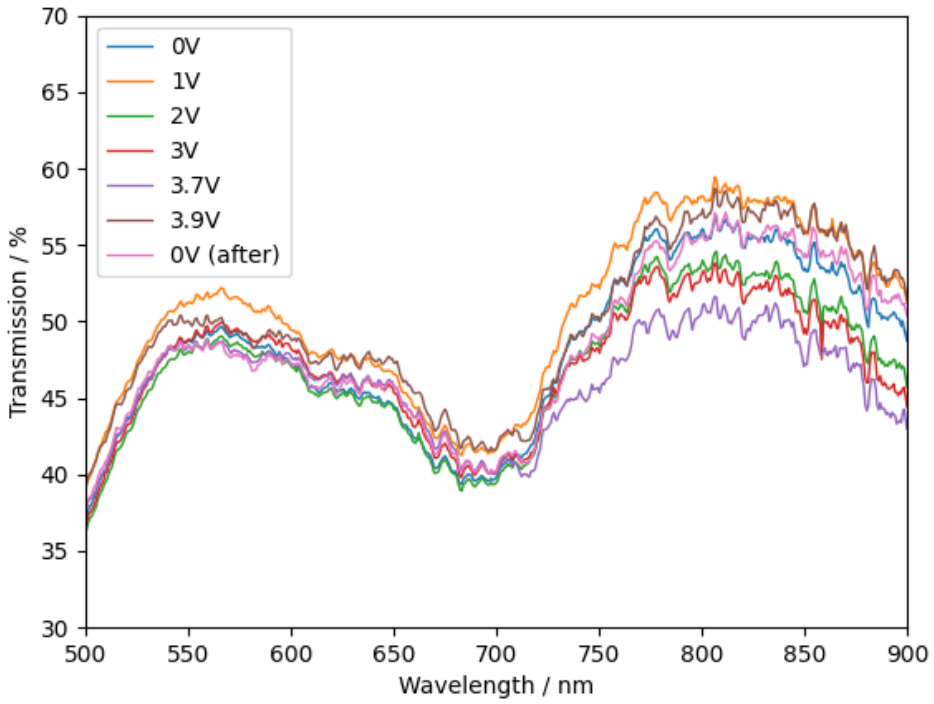

FIGURE 2.8: Transmission spectra of Sample 4 metasurface measured at increasing voltage starting from $0V$ to $3.9V$ and then back to $0V$.

This experiment on the pristine metasurface shows that the nanobridges that bore the wires connected to opposite potentials, started to move only at around $3V$ and come into physical contact with each other immediately. When the bias voltage was withdrawn the nano-brides remained stuck, held together by Van der Waals forces and dielectric charging. That process permanently transforms the pattern of the metamaterial from a single to a, effectively, double-wire zigzag grid as shown on Figure 2.2c, which was also detected optically as an irreversible change in the transmission spectrum of pristine metamaterial samples. Hence, in comparison with [89] and between two samples (3 and 4), it can be concluded that in spite of fabrication aiming to produce exactly the same samples, their response to applied voltage – for example – the voltage that stiction occurs can vary from $2.7V$ to $3.4V$, for example, and the spectral response of such dynamic system is complex and not exactly overlapping for different samples with the same applied voltage.

Although, optical changes due to complete structural switching in a reconfigurable metamaterial can in principle be extremely large, it is of no use if the switching happens once and cannot be reversed. Thus, highlighting once again that stiction is a major reliability issue in many micro and nano-electro-mechanical systems, and it so far has severely limited the application of mechanical tuning in metamaterials.

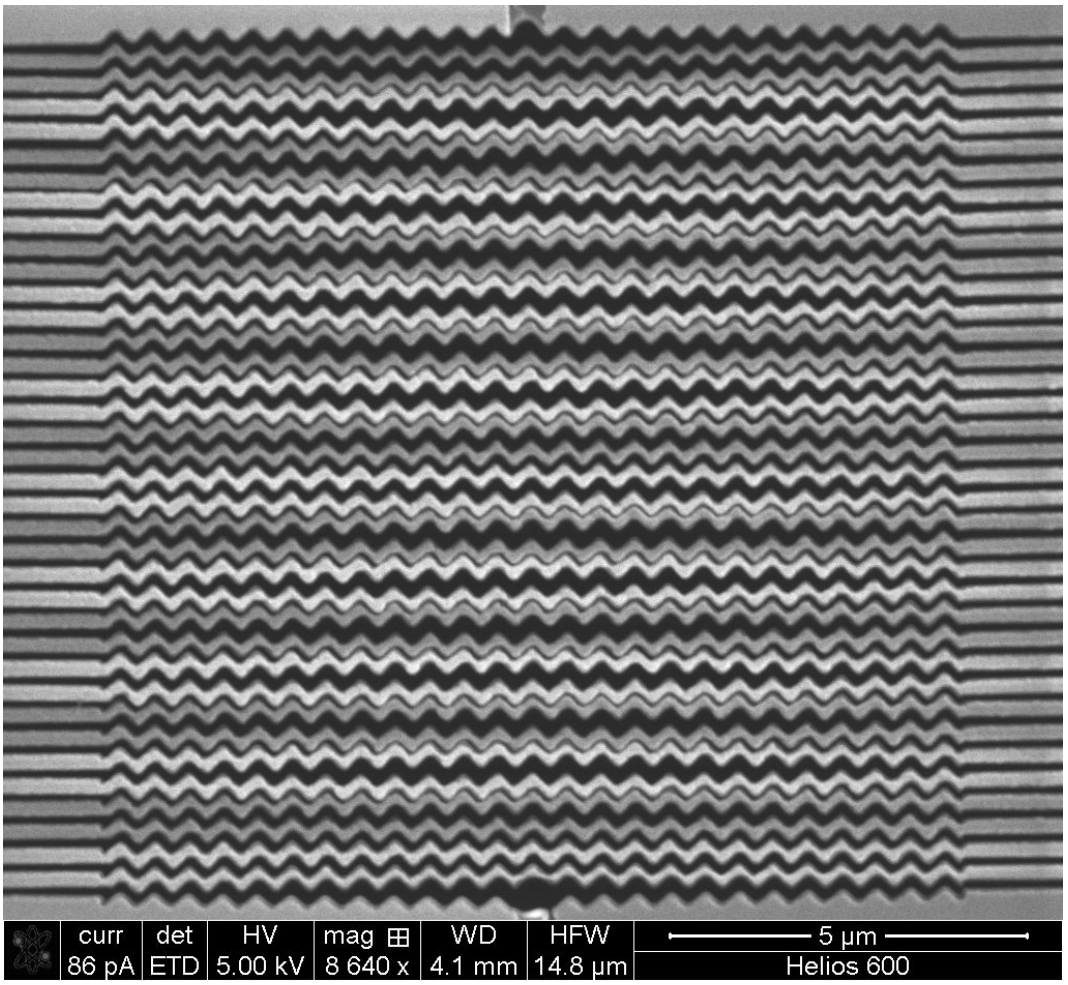

FIGURE 2.9: Sample 3 with $3V$ applied. Most bridges are coupled except the bottom pair and a pair in the center. Scale bar, shown at the bottom right of the SEM image, is $5\mu m$.

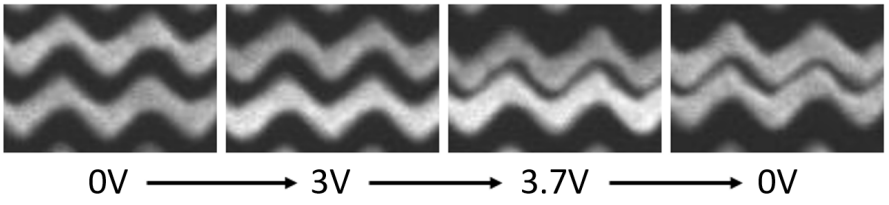

FIGURE 2.10: Zoomed in image of a pair of nanobridges as voltage was applied and then removed.

While applying voltages and measuring spectra, the resistance between nanobridges was also monitored, providing additional data on when the bridges get attached and their resistance changes.

After testing the metasurface samples and leading to stiction, in the next part of this project LCs were applied to their surface to explore if the nanobridges could be repaired using the elastic forces of the LC.

2.3.3 Spectra of zigzag nanowire membrane with liquid crystals and applied voltage

Sample 3 and Sample 4 were then hybridised with the liquid crystal 5CB following the procedure described earlier. A drop of LC was deposited on a glass substrate, covered with polyimide, a typical alignment layer used in LC cells to ensure uniform arrangement of LCs. The glass substrate was placed on a hot plate, kept there for approximately 15 minutes and thus warmed up to the temperature of $65^{\circ}C$, to induce a phase transition in the LC to the isotropic phase. Subsequently, the substrate was then put together with a metasurface membrane. Figure 2.11 shows the changes in transmission spectra of sample 3 with the addition of 5CB.

Spectroscopic results provided most useful insight into the response of the bridges with and without LCs. Ideally, capturing images of the membranes containing organic layers would have been very helpful, but given the nanoscale of the zigzag features, optical microscopy would be of limited value. SEM images, of sufficient resolution and contrast, were not possible to obtain due to technical challenges in capturing images of systems with an organic overlayer.

Figure 2.12 shows the changes in transmission spectra of sample 4 with the addition of 5CB.

5CB remained as a LC of choice. Although there are other liquid crystals that have higher elastic constants [90], so in principle other LCs could provide a stronger restoring force. 5CB elastic constants are $K_1 = 6pN$ and $K_3 = 9pN$ while another, easily available liquid crystal, E7, has $K_1 = 10.7pN$ and $K_3 = 16.2pN$. However, E7 has relatively high phase transition temperature, $58^{\circ}C$, so realising isotropic-nematic transition as shown in [89] for 5CB (with its nematic to isotropic phase transition temperature of $35.2^{\circ}C$) would be more difficult to realise. Furthermore, another important parameter for infiltrating small gaps between nanobridges is viscosity. 5CB has rotational viscosity of approximately $92.5m.Pa.s$, while E7 has viscosity approximately 2.5 times higher, namely $232.6m.Pa.s$ [91]. Thus, 5CB is more suited as a tool to detach stuck nanobridges. The viscosity of 5CB decreases to approximately $20m.Pa.s$ in the isotropic phase, hence the LC was heated to reach this phase, thus promoting more strongly the infiltration of the gaps between the nanobridges. The elastic constants are also reduced in the isotropic phase, all approaching $2pN$. Hence, the effect observed in Figure 2.3, where voltage was ramped up and down with LC being in the isotropic phase and this state, there was a hysteresis in transmission, indicating that the nanobridges remained stuck. The small elastic forces of 5CB in the isotropic phase were not able to prevent stiction, but when cooled to the nematic phase, at room temperature, the bridges were unstuck.

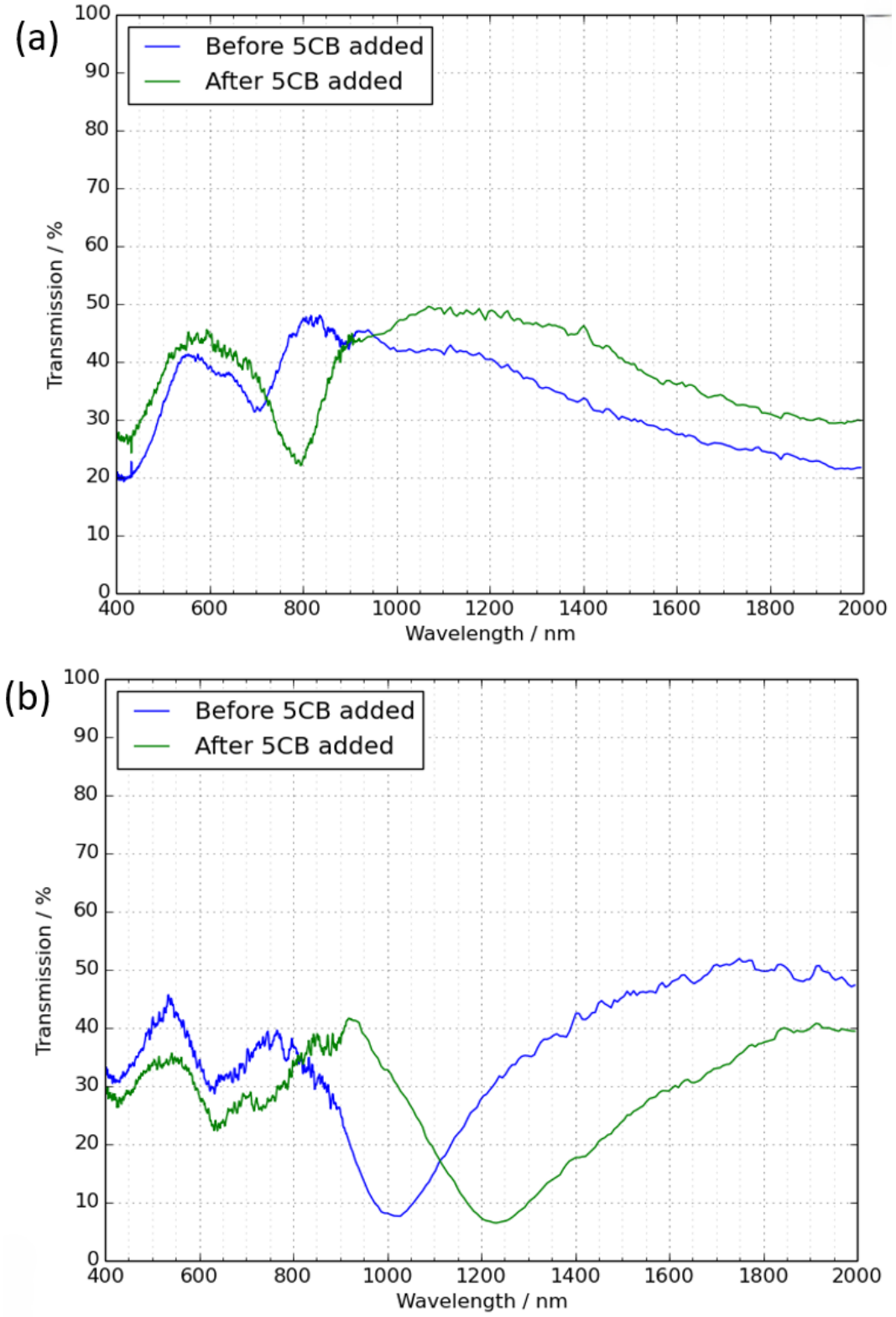

FIGURE 2.11: Transmission spectra of sample 3 before and after 5CB added for polarisation parallel (a) and perpendicular (b) to the nanowires.

The same procedure was undertaken to test the samples as in [89] and in the case of pristine samples, as shown in the previous section, except as mentioned earlier, the

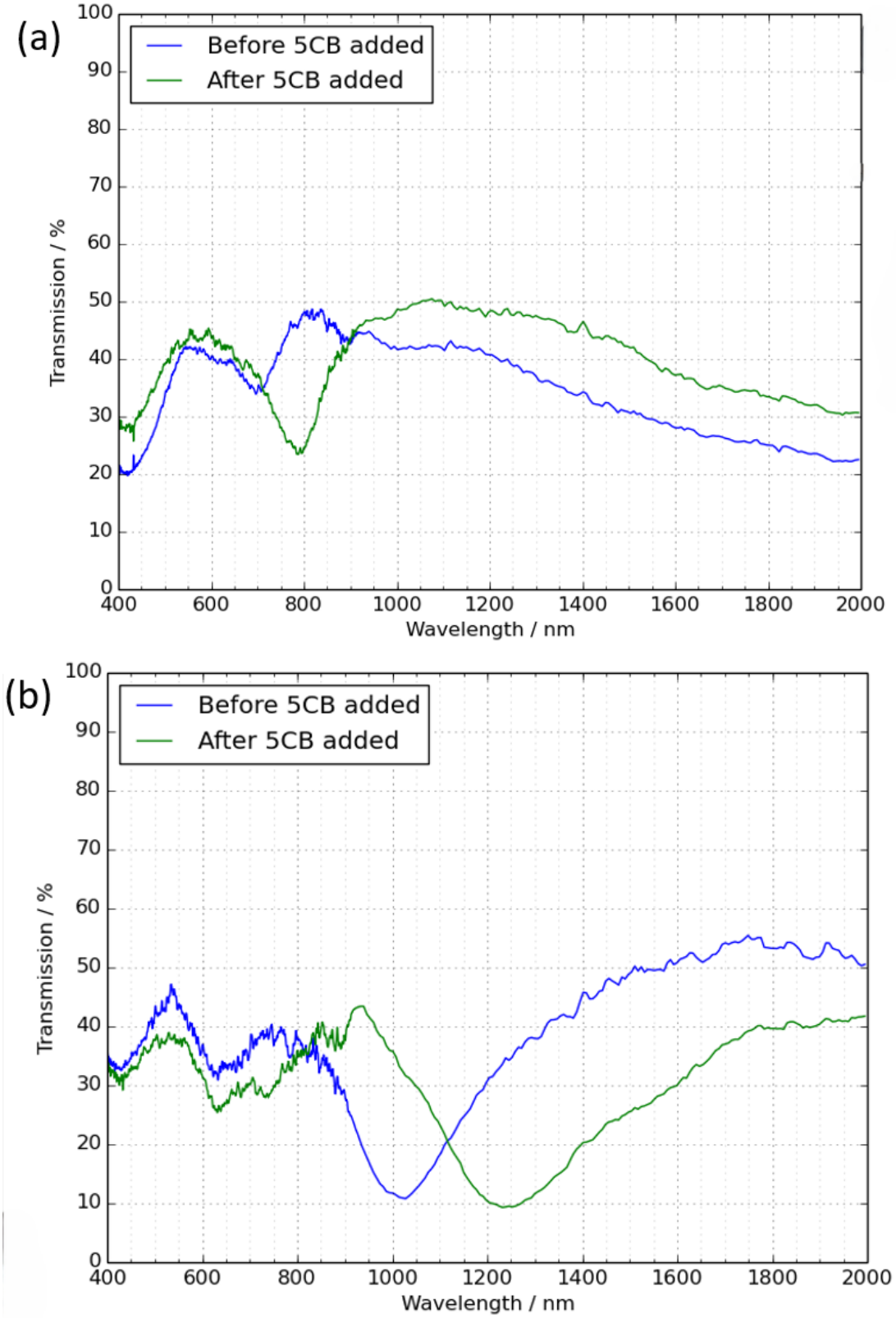

FIGURE 2.12: Transmission spectra of sample 4 before and after 5CB added for polarisation parallel (a) and perpendicular (b) to the nanowires.

samples could not be observed using the SEM as having an organic layer of LCs on top, the image of the underlying structure could not be captured with a technique like SEM. The samples were therefore only tested using a microphotospectrometer as before. As in the previous study, due to the presence of the LC, the transmission resonance of the sample was red-shifted by approximately $200nm$, as

As stated earlier, following the results shown in Figure 2.3, the challenge was whether a metasurfaces, with stuck nanobridges, could be repaired by the subsequent application of liquid crystals. This was tested on Sample 3 and Sample 4, with stuck nanobridges and LCs applied to their surface after stiction occurred. The spectra were then collected to see if returning to $0V$, following application of voltages above $3V$, leads to close overlap with the spectrum recorded for a pristine sample (and accounting for a phase shift due to LC layer).

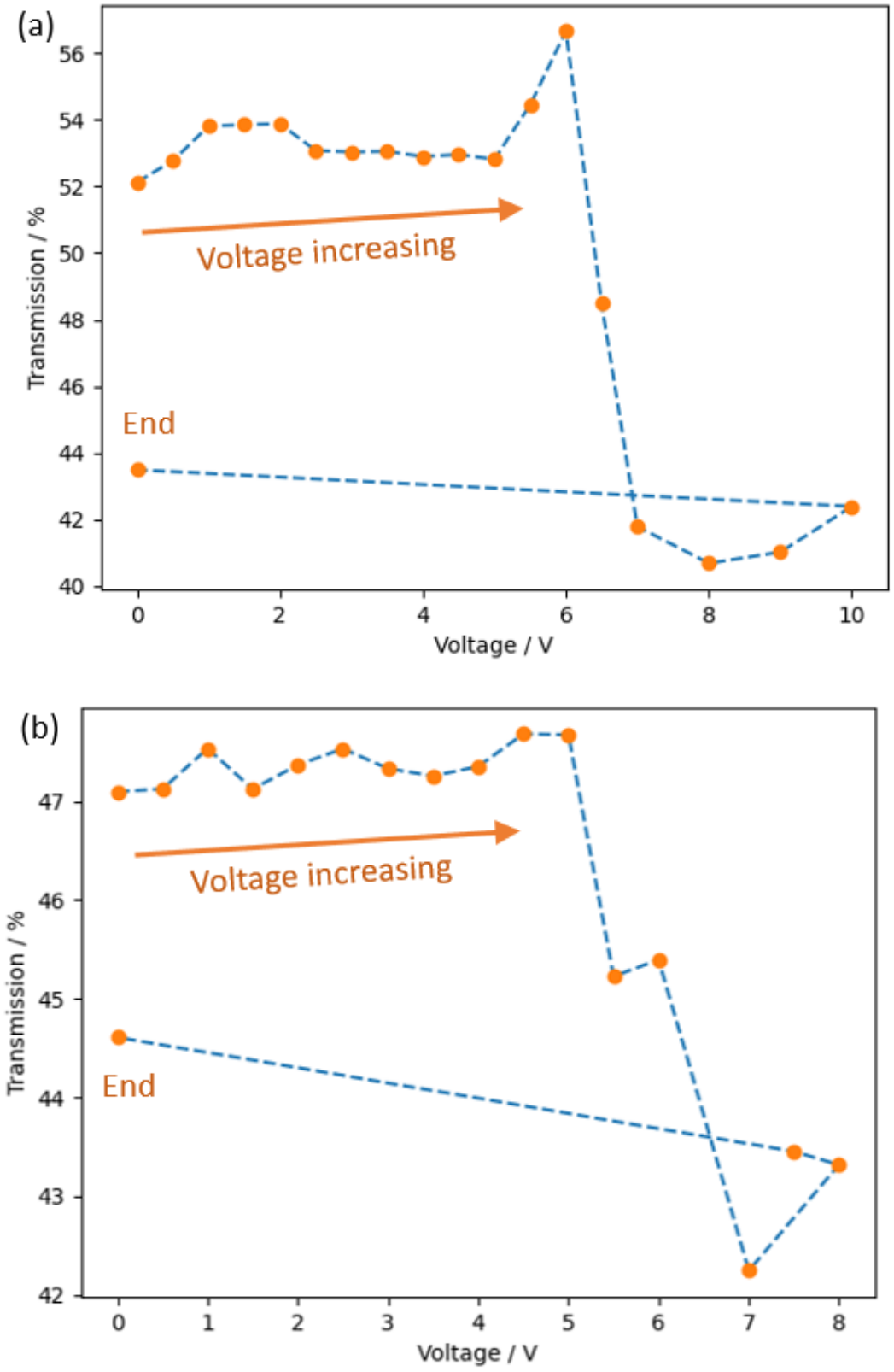

FIGURE 2.13: Transmission at $1\mu m$ as the voltage is varied with 5CB for polarisation parallel to the nanowires. (a) Sample 3 and (b) Sample 4.

The preliminary results, shown in Figure 2.13 were promising. Both samples show

similar paths as the voltage was varied. The relatively flat response in the level of transmission, measured at the resonant wavelength, from 0V up to approximately 5V indicates that the core membrane structure remained the same in that range. The transmission for neither of the samples returned to its starting point once the voltage (10V) was removed. It is hard to tell whether this change is from the increased mobility of the bridges, once released, or whether we are seeing changes due to the liquid crystal present. As the change is irreversible, one explanation could be the LC being worked into the metasurface and penetrating further as the voltage was cycled.

The differences in spectra of the pristine samples 3 and 4 as they were coupled, indicated their differences, stemming from their different stiffness and their varying dependence with increasing voltage. Therefore, it was decided that several additional samples, had to be fabricated in order to fully understand the effect. Unfortunately, in spite of successful fabrication of the previous samples, all the new metasurfaces kept failing due to persistent short circuit problems, with the issue persisting for months in spite of multiple attempts. One of possible reasons was a different supply of gold material (as the old source was no longer available) or contamination from the FIB. The attempts with fabrication were paused and the closure of cleanrooms due to Covid prevented any later experiments.

2.4 Conclusions

The results shown in this chapter extended the earlier work aiming to implement tuneablity in metamaterials as well as offering an anti-stiction solution for NEMS/MEMS, multifunctional sensors and switches. Liquid crystals were chosen to achieve this functionality and given a wide range of the structural transitions exhibited by these materials at the nano-scale, smart and adaptable nano-systems and meta-devices could be envisaged.

As shown in the experimental section, the work carried out for this thesis, confirmed in new samples that LCs, when coupled to the fabric of a re-configurable photonic metamaterial, can efficiently modify the behaviour of nanoscopic mechanical actuators.

SEM images and spectra were captured from two different nanobridge metasurface samples and their analysis showed that stiction observed in SEM images of the pristine samples can also be detected through the observed spectra. The optical spectra capture the changes in the structure of the nanobridges, where in places it changes from a single zigzag wire to a double zigzag, where the nanobridges end up attached to each other. The comparison of the two metasurface samples, although designed to be the same, revealed that while they both experienced stiction, the effect started at different voltages and the trends observed in their spectra with increasing voltage were also somewhat different. Further investigation could include measurements with AC voltage at different frequencies to explore the effect on the spectra and on the voltage when stiction occurs. In addition, different polarisation states of the incident light, such as circular for example, could be included, following the experiments presented here with linearly polarised light parallel or perpendicular to the zigzag nanowires.

The results and analysis shown in this chapter demonstrate that nanostructured metasurfaces remain an attractive platform and test bed to explore both optical and mechanical effects, in spite of the challenging fabrication techniques required. Their structure is well suited to integrate organic materials, such as LCs, to investigate how the dielectric, optical and elastic properties of the organic layer can affect the response and the performance. This study of a suspended metasurface was followed by a related project which explored the optical characteristics of the zigzag metasurface geometry on a static glass substrate, in particular their response to light with different levels of coherence.

Chapter 3

Zigzag Metamaterials

As summarised in the previous chapter, the concept of artificially engineered media (known as metamaterials) has revolutionised the field of optics, photonics and materials, extended the boundaries of microfabrication and stimulated the development of novel characterisation techniques. The demonstration of anomalous reflection and refraction of light by metasurfaces opened another exciting chapter in optical engineering [92].

One class of such metasurfaces, namely non-diffracting wavevector selective metasurfaces [27], exhibit optical transmission spectra with a strong amplitude correlation with the angle of incidence. The zigzag design, belonging to this class, was explored in this study. Different variations of this design were simulated and fabricated to further explore its properties. These designs were optically characterised and showed differences when compared with the simulated spectral responses. To understand these differences the zigzag metasurfaces were characterised using a coherent light source in the near-IR.

3.1 Design and fabrication of zigzag metasurfaces

The first 2 metasurfaces that were investigated consisted of arrays of continuous zigzag nano-wires (ZZnW) and their inverse, continuous zigzag nano-slits (ZZnS). The unit cell of the metasurface was $650nm \times 500nm$ which rendered the zigzag metasurfaces immune to scattering into high-order diffraction modes in the near-IR. Each unit cell contained a single chevron of the zigzag structure. The chevrons arms were $125nm$ wide and at 45° to the base of the unit cell and at 90° to each other. A 32×40 array of this unit cell formed the full metasurface making an active area of $20.8\mu m \times 20\mu m$.

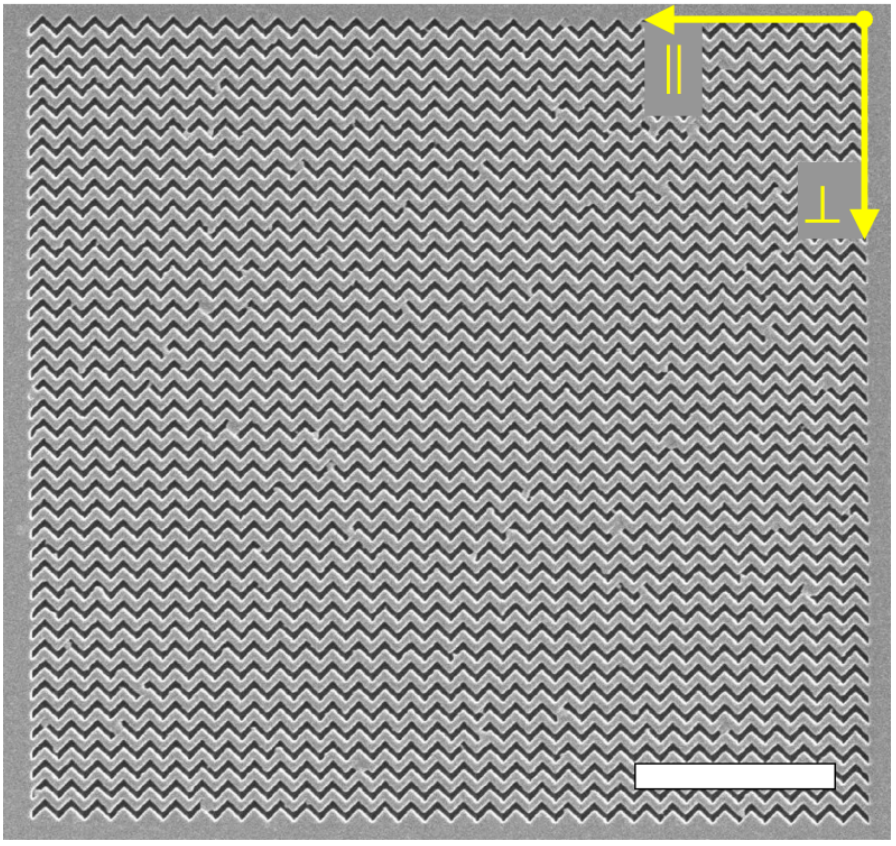

FIGURE 3.1: SEM image of entire continuous zigzag slits metasurface. Scale bar is 5 μm.

A Helios Nanolab 600 DualBeam FIB/SEM was used to mill the metasurfaces into an $80nm$ thick film of amorphous gold sputtered onto a $0.5mm$ thick fused-quartz substrate. This machine incorporates a field-emission SEM with imaging resolution down to $1nm$ and a gallium ion gun with a milling resolution of $20nm$.

To further investigate the properties of the zigzag metasurfaces additional samples were fabricated with variations in the zigzag geometry. The first of these was to break the continuous structures to see how they are affected by blocking the propagation of plasmons along the zigzag wires and slits. To do this, gaps were placed at each apex in the zigzag geometry to form metasurfaces of isolated wires or slits. The gaps were $50nm$ wide for the wire samples and $100nm$ wide for the slit samples. This difference was required to ensure the gaps in the slit samples remained intact during the milling process. In addition to the fully isolated designs another variation was made with gaps placed at every other apex to form metasurfaces of separated chevrons. These samples are shown in Figure 3.2. The next change was to make the angle between the zigzag arms sharper. Samples were fabricated with the zigzag arms at 51° and 59° to the base of the unit cell with the width of the zigzag arms remaining constant. These had unit cells with dimensions of $600nm \times 600nm$ and $500nm \times 650nm$ respectively.

The angle variations for the slits are shown later in Figure 3.18. Continuous, isolated and chevron wires and slits were fabricated with each of these sharper angles.

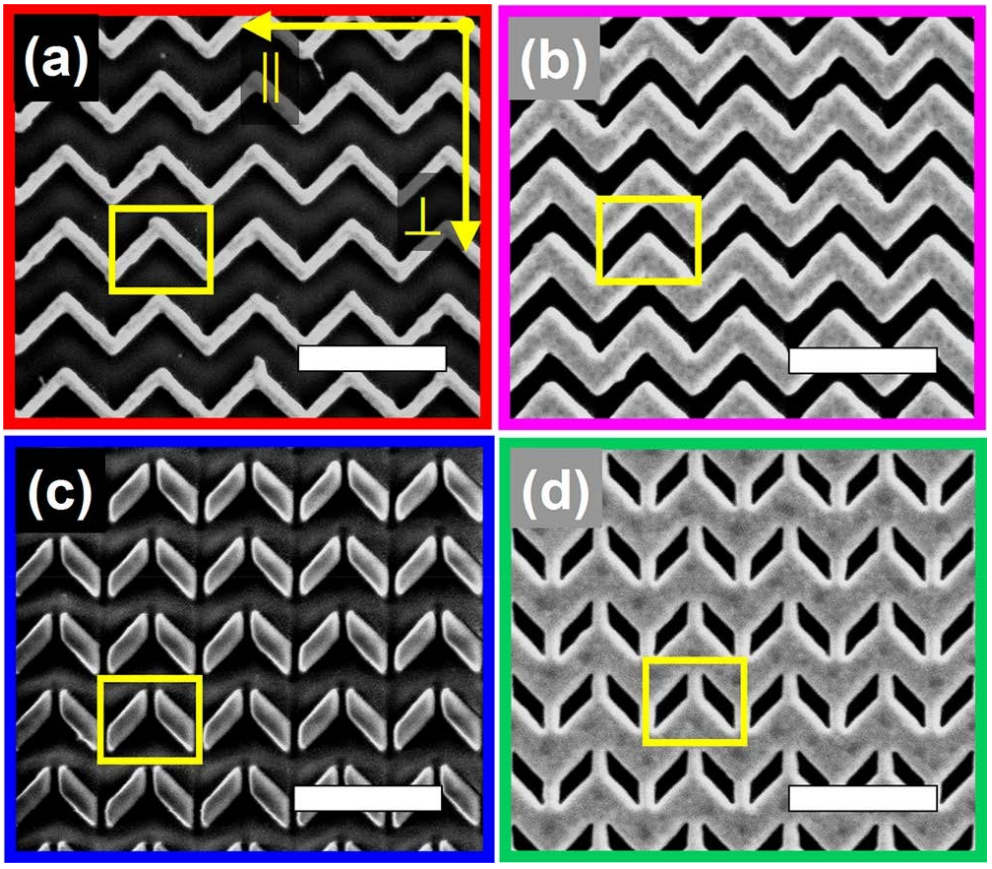

FIGURE 3.2: SEM images of fabricated planar metamaterials featuring (a) continuous zigzag nanowires, (b) continuous zigzag nanoslits, (c) broken zizag nanowires, and (d) broken zigzag nanoslits. Yellow boxes indicate elementary unit cells of the metamaterials. Scale bars are $1\mu m$.

3.2 Optical characterisation

The transmission and reflection spectra of the metasurfaces were recorded using a commercial near-IR microspectrophotometer. It was developed by CRAIC Technologies based on a ZEISS Axio microscope and features a cooled near-IR CCD array with spectral resolution of $0.8nm$ and a Köhler illumination system with a broadband linear polariser. The latter incorporated a tungsten-halogen lamp and was tuned to a $\times 15$ reflective objective with NA 0.28, producing broadband incoherent plane-wave illumination at near normal incidence. The spectra were collected through a set of square apertures of various sizes installed in the image plane of the microscope. The largest aperture that fit within the active sample area was used for each measurement, most commonly the 11µm square. The measured transmission spectra were normalised to the transmission of the bare substrate or with the sample

removed where this was not possible. The reflection from a bare gold area of the samples was used to normalise the reflection spectra. A dark scan was also used to remove any stray incidental light from the measurements. For reflection this was done by replacing the sample with a piece of Vantablack which has near 0% reflectivity and for transmission by blocking the illumination path.

Some of the spectra presented in the following figures include a minor technical artefact present at $900nm$ where the detectors change in the spectrometer from one sensitive to visible light, to a cooled detector for infrared radiation. This is a common issue in spectrometers with a large spectral range and can be reduced through careful calibration of the machine.

3.3 Simulation method

The commercial simulation software COMSOL Multiphysics was used to model the zigzag metasurfaces. The model consisted of a single unit of the gold metasurface placed on top of fused quartz and with air above. The quartz and air extend $2\mu m$ away from the gold with refractive indices of 1.45 [93] and 1 respectively. The real and imaginary refractive indices from tabulated data [94] were used to define the properties of the gold. The 4 boundaries surrounding the metasurface were defined as continuous boundary conditions, effectively making the model an infinite plane. The top and bottom of the model were defined as ports and were terminated using perfectly matched layers to eliminate any reflections. Different volumes in the metasurface plane were selected to be gold to model the inverted and isolated structures. An identical model with no gold present was used as a reference to normalise the results. Further details can be found in Appendix B.

3.4 Transmission spectra of zigzag metasurfaces

Figure 3.3 shows the details of the three designs of slits explored in this study. The inverse of these formed the wire samples discussed later.

3.4.1 Spectra of zigzag slits

The following figures show either the reflection or the transmission spectra of the three types of zigzag structures considered here: Continuous, Isolated and Chevron illuminated by incoherent light. The first set of figures presented the slits format as shown in Figure 3.3.

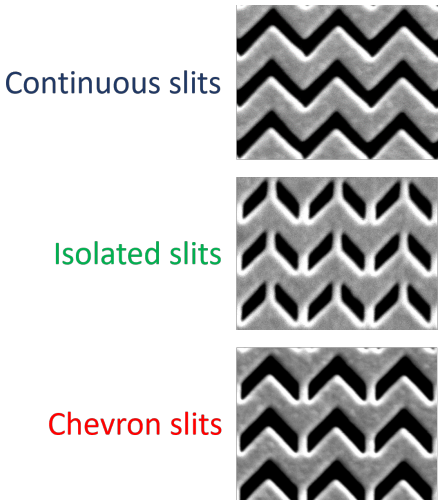

FIGURE 3.3: SEM images of the 3 zigzag slit variations investigated. Each image contains 9 unit cells in a 3×3 array with a total size of $1.95\mu m \times 1.5\mu m$.

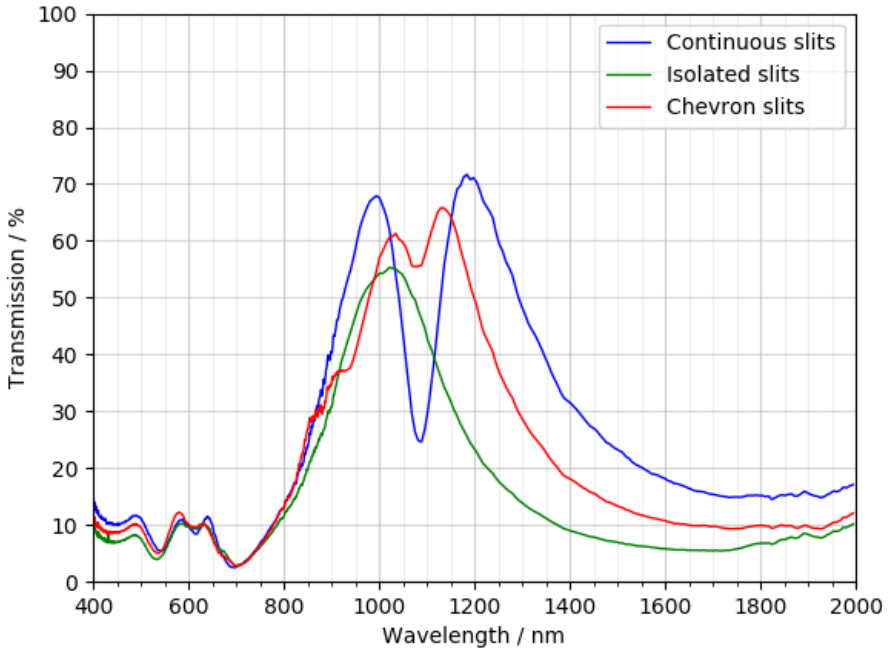

FIGURE 3.4: Transmission spectra from three zigzag variants. Polarisation parallel to slits.

As shown in Figure 3.5, the continuous slits have a distinct double dip in reflection around $1100nm$. The chevron slits have a less pronounced double dip at a slightly lower wavelength. The isolated slits have a single dip in reflection at $950nm$. Figure 3.4 shows features in transmission that line up with the features observed in the reflection spectra. The continuous slits have a distinct double peak, while the chevron slits have a much less pronounced double peak. The isolated slits show a single peak in transmission.

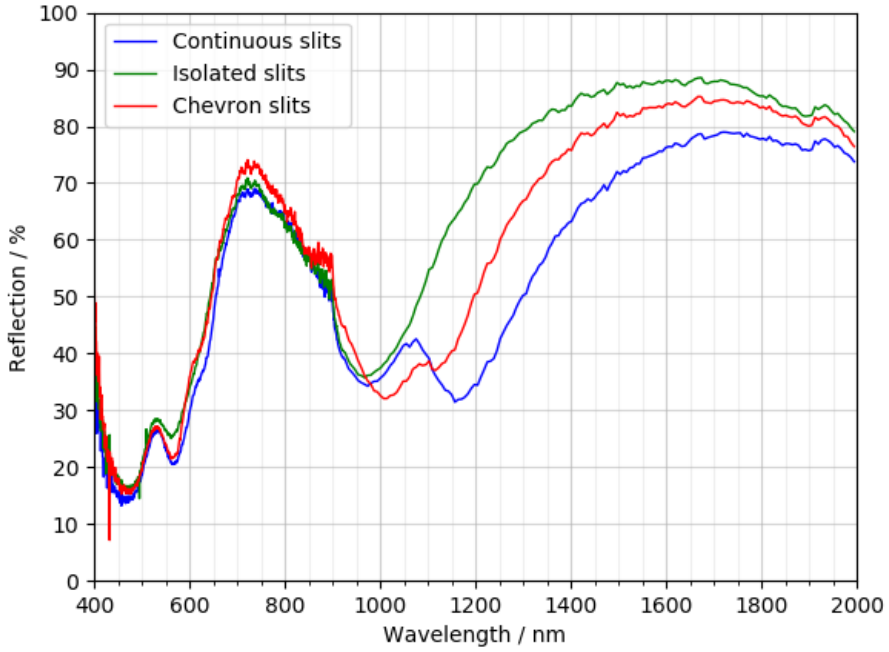

FIGURE 3.5: Reflection spectra from the 3 zigzag variants. Polarisation parallel to slits.

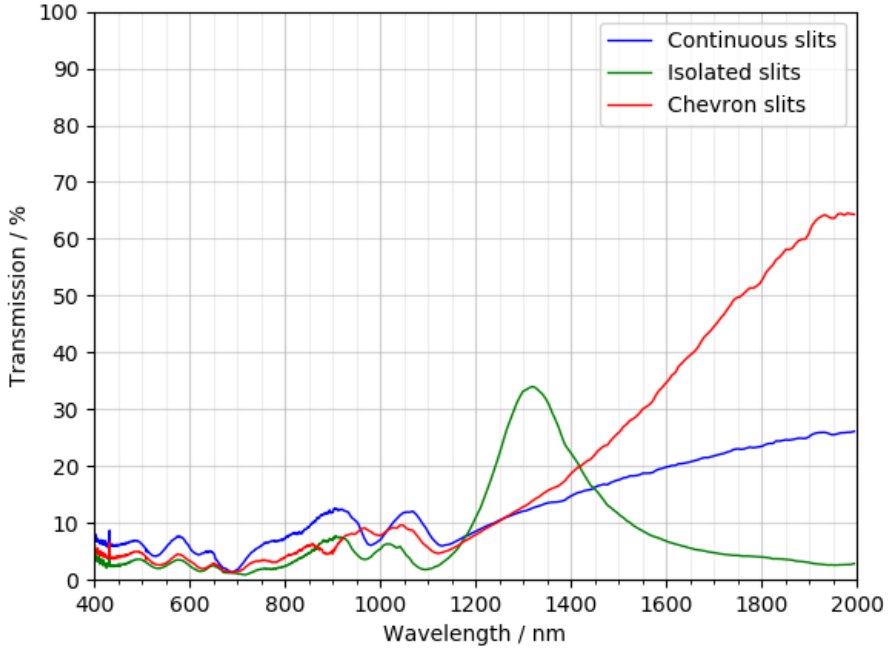

FIGURE 3.6: Transmission spectra through the three zigzag variants. Polarisation perpendicular to the slits.

Figure 3.7 spectra indicate that both the isolated and chevron slits have a strong dip in reflection at 1300nm and 1900nm, respectively.

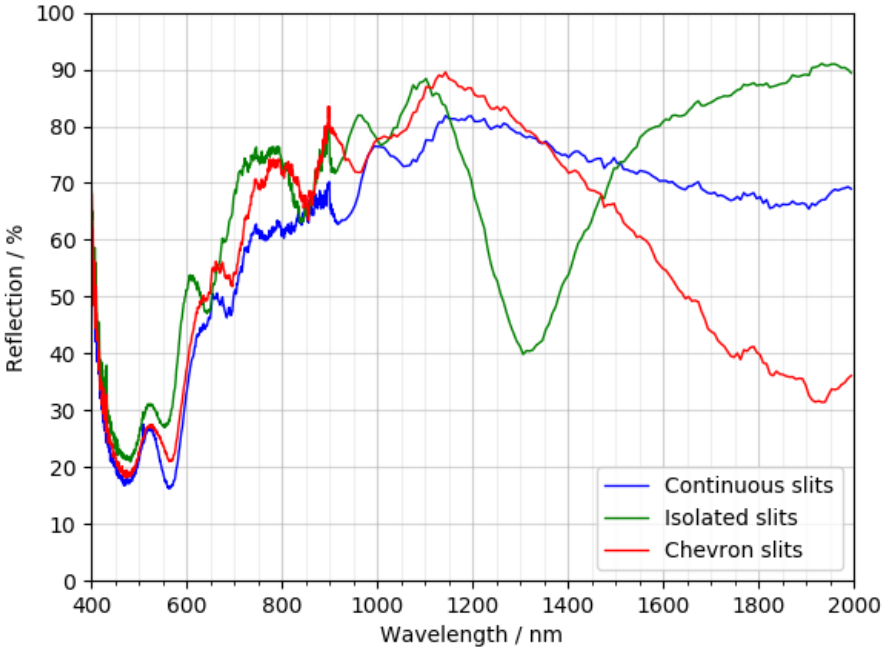

FIGURE 3.7: Reflection spectra of three zigzag slit variants with incident polarisation perpendicular to slits.

Figure 3.6 presented the spectra with the isolated and chevron slits that have peaks in the transmission spectra that line up with the dips in reflection on the previous slide. The peak for the isolated slits is much lower and shows absorption of around 40% when compared with the dip in reflection. Chevron slits only show around 5% absorption.

3.4.2 Spectra of zigzag wires

The next figures show the spectra of the inverse metasurface consisting of nano-wires. These can be considered as the positive complement to the negative designs shown previously which consisted of nano-slits. 3 variations on the design were again investigated. These are shown in Figure 3.8 and were continuous, isolated and chevron zigzag nano-wires.

Figure 3.10 shows the reflection spectra with the polarisation perpendicular to the nano-wires. The continuous wires show a double peak in transmission around $1150nm$. The chevron wires only have a single peak here. The isolated wires have a single peak at a slightly lower wavelength.

Figure 3.9 shows that the continuous wires have a double dip in the transmission while the chevron and isolated wires only have a single dip. These features correspond to the reflection features seen on the previous slide.

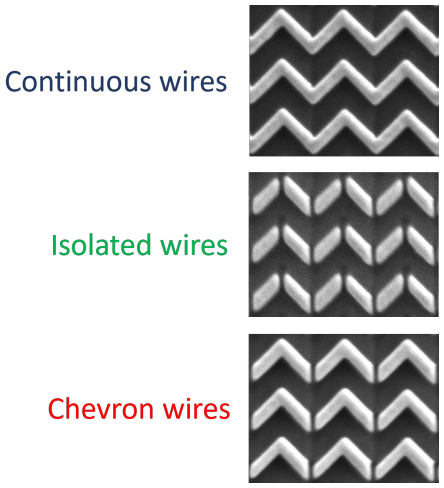

FIGURE 3.8: SEM images of the 3 zigzag wire variations investigated. Each image contains 9 unit cells in a 3×3 array with a total size of $1.95\mu m \times 1.5\mu m$.

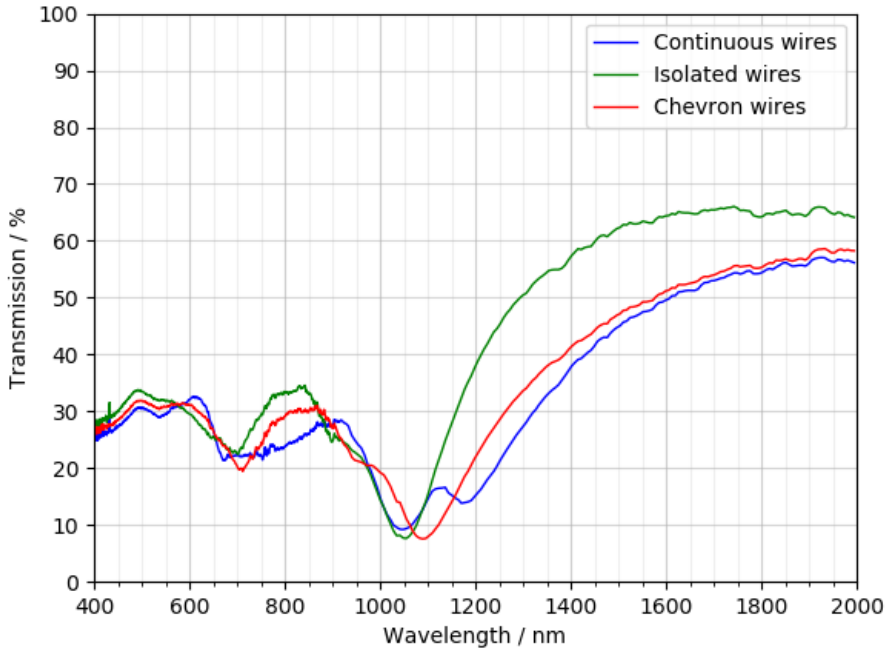

FIGURE 3.9: Transmission spectra from the zigzag wire variants. Polarisation orthogonal to the wires.

Figure 3.12 shows that the isolated wires have a peak in reflection at $1350nm$. The chevron wires have a peak around $1900nm$. The continuous wires have a peak at $700nm$ and show a rise in reflection towards the end of the wavelength.

Figure 3.11 shows that the isolated wires have a dip in transmission at $1350nm$ which shows around 30% absorption when compared with the reflection spectra. The chevron wires have a dip at $1900nm$ with an absorption of about 20%. The continuous wires show the same split resonance feature that is seen with the continuous slits

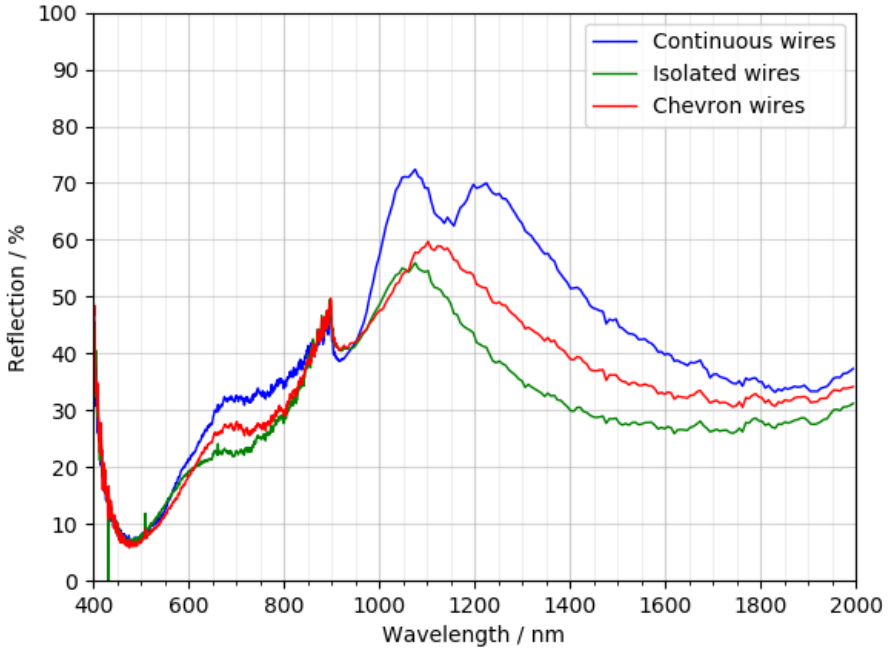

FIGURE 3.10: Reflection spectra from the three wire variants. Polarisation orthogonal to the wires.

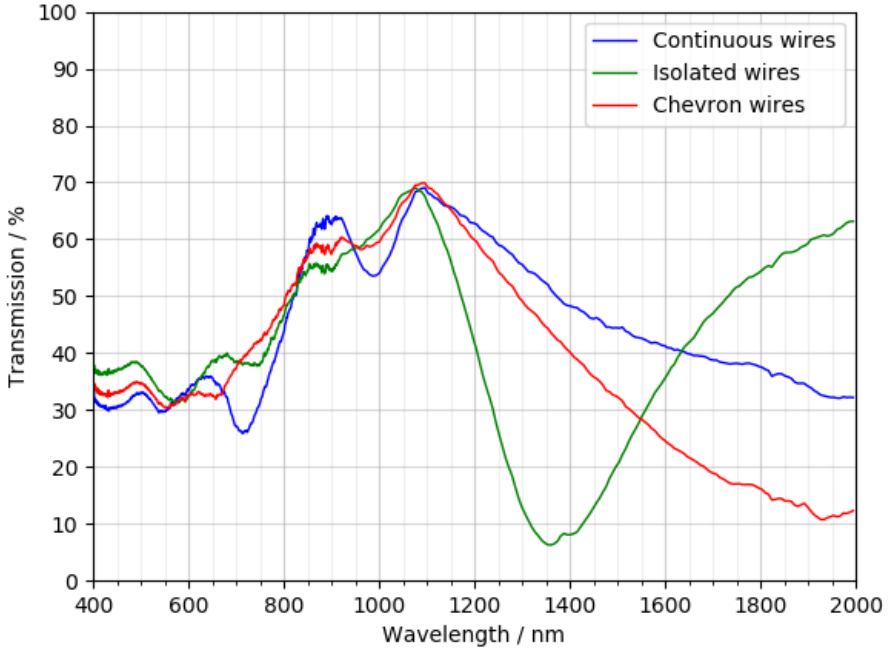

FIGURE 3.11: Transmission spectra from the zigzag wire variants. Polarisation parallel to the wires.

sample at $1\mu m$. While this is the same resonance feature it is much broader and the

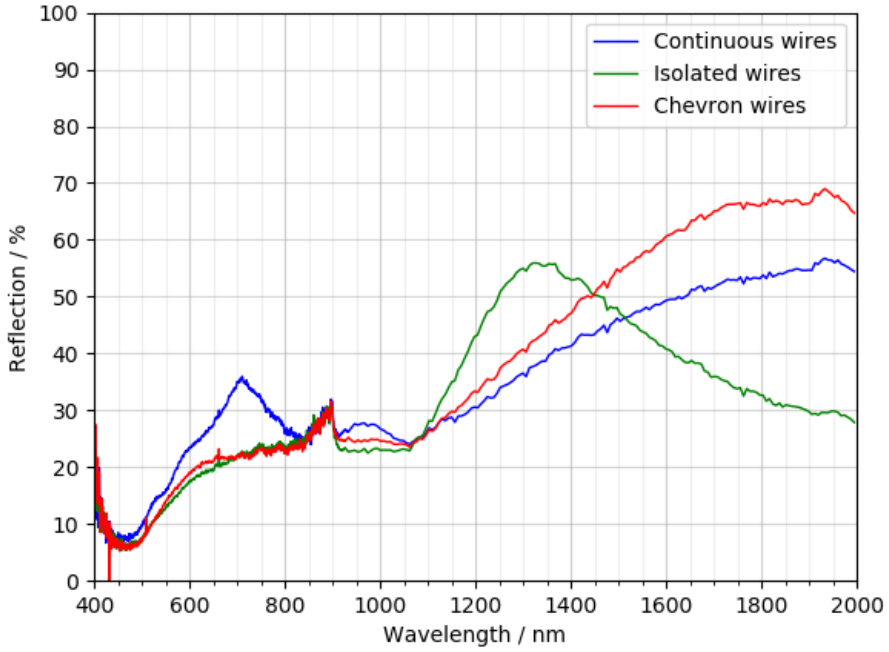

FIGURE 3.12: Reflection spectra from the zigzag wire variants. Polarisation parallel to the wires.

split is not as deep for the wires as their geometry has not been optimised for this polarisation.

3.5 Discussion

The figures presented in the previous section demonstrate the emergence of the split resonance for the continuous wires and slits, and for the chevron slits. The relationship between the reflection and transmission spectra for each polarisation can be seen and the effect of absorption is also observable. The transmission and reflection spectra of the continuous, isolated and chevron metasurfaces for both polarisation orientations form a comprehensive dataset for the exploration of these effects.

The discussion of results starts with a comparison between the experimental results and simulated spectra.

3.5.1 Comparison between modelling and experiments

The results of the COMSOL simulations for each metasurface design are shown in the Figure 3.13 alongside their corresponding experimental results. The method used was described previously in Section 3.3 and further details can be found in Appendix B.

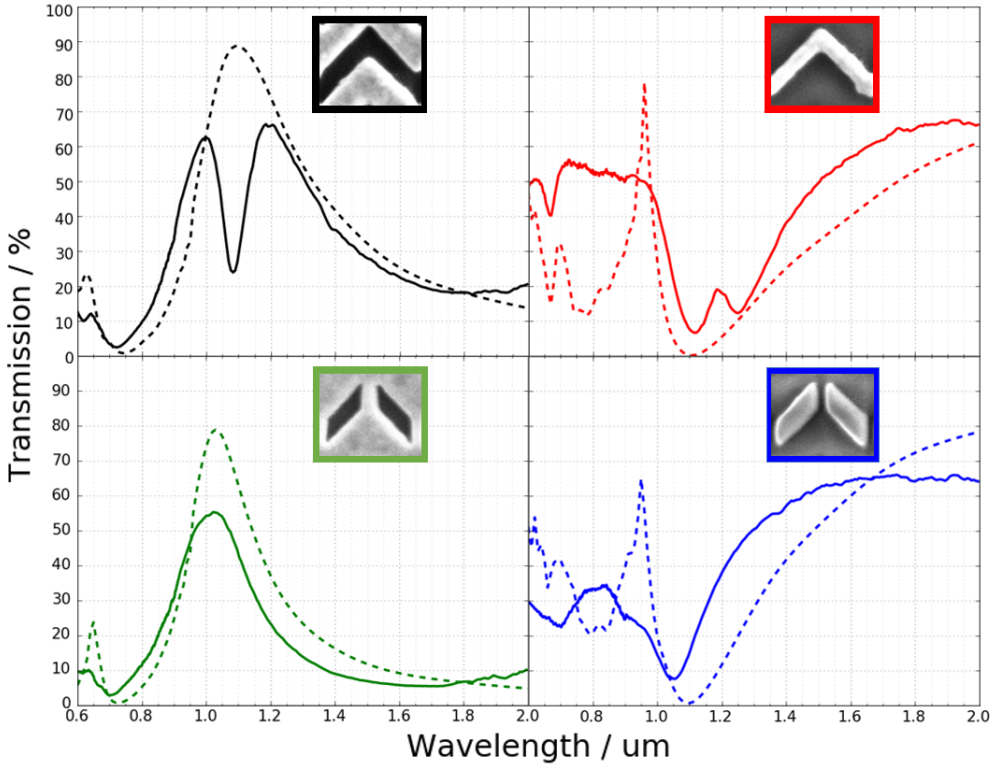

FIGURE 3.13: Transmission spectra for the continuous and isolated slits and wires, as indicated in the insets. Measured spectra are shown as solid lines and the simulated spectra as dashed lined. Note the colours: black, red, green and blue indicate the four designs indicated in the insets.

There is a large disparity between the experimentally obtained spectra and those from the modelling. The experimental result for transmission through the zigzag slits, plotted as a solid black line, shows a double peak when the incident polarisation is parallel to the slits of the surface. This is not seen in the modelled spectra, plotted with a dashed line, which shows a single resonance peak. An analogous effect is observed for transmission through the zigzag wires when the polarisation is orthogonal to the wires, shown again in Figure 3.13. Here a double dip is observed experimentally where a single dip is found when the structure is modelled.

The double dip feature seen for the zigzag wires corresponds to the double peak feature for the zigzag slits. The feature for the zigzag wires is red shifted by $100nm$ from that of the slits. This is due to the two metasurfaces not being the exact inverse of each other. This can be seen in the SEM images in Figure 3.13 where the slits and wires milled in the gold are roughly $150nm$ and $100nm$ wide, respectively. This is due to imperfections from the fabrication techniques.

The simulations for the chevron structures show a single peak or dip for the slits and wires respectively. The experimental results for the chevron wires agree with this while the chevron slits show a less pronounced double peak. For the isolated slits and

wires the experimentally obtained spectra agree with the results from the simulations, both showing a single peak or dip. These result shows that the effect is inherent to the larger superstructure of the surface and not the individual unit cells.

The results of my simulations, presented in Figure 3.13, agree with the experimental spectra observed from the isolated wires and slits but not for the continuous wires and slits where the distinctive split resonance is missing. One apparent difference between my simulations and our experimental set up is the coherence of the incident light. In the microphotospectrometer, the light originates from an incandescent white light source, meaning the light is incoherent. In contrast, the light in my simulations is in the form of a plane wave and is therefore spatially coherent.

To investigate this difference further a larger and more complex COMSOL model was constructed by Dr Vassili Fedotov to simulate the effect of incoherent illumination. Instead of using periodic boundaries, a complete, albeit smaller, version of the continuous zigzag slits was created. It contained 10×12 unit cells, measuring $6.6 \times 6.2\mu m$. All the simulation's boundaries were terminated using scattering boundary conditions. Light was input through one of the faces parallel to the surface and the power was captured at the opposite face. Unlike before the input face was split into 9 different regions which each produced an individual light beamlet. Each of these beamlets had a cross-section measuring $2.4 \times 2.4\mu m$. This size corresponds to the spatial coherence length of incandescent white light at a wavelength of $1.1\mu m$. The response to incoherent light was simulated by running the model 9 times, each time engaging only one of the beamlets, and then calculating the sum of the 9 transmission spectra. By running the model with all the beamlets engaged, coherent illumination could be produced.

The results of Dr Fedotov's simulations are shown in Figure 3.14. As can be seen, for incoherent light, the model reproduced the signature double peak feature that we observed experimentally. When the model was set to produce coherent light the same response as was seen in our previous simulations was observed.

3.5.2 Spectral response of the zigzag slits

The simulated spectral response of the metasurfaces for all three types of designs, continuous, isolated as well as chevron, contained a single resonance spanning from $0.9\mu m$ to $1.5\mu m$ and centred at $1.1\mu m$. This resonance corresponds to the excitation of the fundamental $\lambda/2$- current mode – a standing wave of charge (plasma) oscillations, which builds up in every straight segment of the zigzag pattern once the half of its period can fit the length of the segment.

In the wavelength range $0.9 - 1.5\mu m$ the spectral feature, shown in blue curve in Figures 3.4 and 3.10, for example for the continuous slits design, includes a pair of

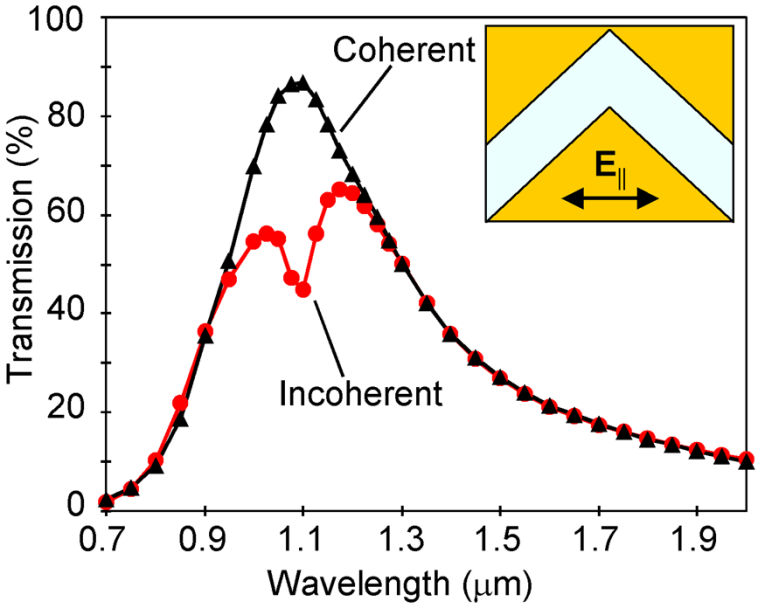

FIGURE 3.14: Modelled spectral response of the continuous zigzag slits when illuminated using incoherent and coherent light. Insert shows the polarisation orientation relative to the slits.

resonances separated by a gap of about $0.2\mu m$. This feature is also visible, but less pronounced for the case of the chevron slits, shown in red curve, but is absent for the case of isolated slits (green curve) Intriguingly, the overall profile of the spectral response in each case resembles closely that of Fano resonances normally exhibited by metasurfaces with substantially more complex patterning. More intriguingly, the results of our measurements disagree – even at the qualitative level – with the predictions of rigorous numerical modelling that informed the actual design of the metasurfaces.

Given the complementarity of the two metamaterials, the profiles of the respective split resonances were also complementary (as dictated by Babinet's principle): peaks in one spectrum corresponded to dips in the other, and vice versa. Intriguingly, the results of our measurements disagree, even at the qualitative level, with the predictions of rigorous numerical modelling that informed the design of our metamaterials (dotted curves in Figure 3.13). Indeed, the modelled response in each case displayed a whole resonance centred at $1.1\mu m$ [25]. It resulted from the excitation of the fundamental $\lambda/2$-current mode, the most common localised (dipolar) resonant mode that had been particularly favoured by microwave and RF antennas and planar metamaterials of various designs [25; 26]. In the zigzag metasurfaces the mode corresponded to a standing wave of charge oscillations, which built up locally in every straight segment of the zigzag pattern, once the half of the wave's period fitted the length of the segment (see insets to Figure 3.13). That rendered each segment as an independent half-wavelength resonator, which determined the response of the planar

metamaterials. The noted strong (and rather unexpected) discrepancy called for careful examination and verification of the methodology used.

Importantly, since the resonant mode supported by the continuous pattern had its nodes located in the corners of the zigzags, the described modification did not affect the nature of the resonant response in the resulting nanostructures. The localised distributions of charge density sustained by the reference metamaterials at their resonance were very similar to those calculated for the ZZnW and ZZnS metasurfaces. Also, as in the case of continuous zigzags, the transmission spectra predicted for piecewise zigzags featured a whole resonance spanning from $0.9\mu m$ to $1.5\mu m$, though its centre appeared blueshifted by about $50nm$ due to physical shortening of the broken segments. In spite of the apparent similarities between the two cases, it was possible to reproduce experimentally the main features of the response predicted numerically for the reference samples.

Some quantitative mismatch resulted from an uncertainty in specifying the dielectric function of gold and the difficulty of reproducing fine features of piecewise zigzags during the fabrication. The apparent discrepancy between the calculated and measured spectra in Figure 3.13 below $0.9\mu m$ signifies the appearance of the first-order diffraction modes in the substrate due to the $660nm$ period of the metasurfaces (which acted as conventional diffraction gratings in that wavelength range for light propagating in the substrate). The discrepancy results from the fact that those diffraction modes existed only in the substrate, which for practical reasons was modelled as a semi-infinite slab while in the experiment it had a finite thickness.

3.5.3 Origin of transmission suppression by ZZnS metasurface under incoherent illumination

The analysis shown above indicates that the discrepancy between the theory and experiment we observed earlier with the ZZnW and ZZnS metasurfaces corresponded to a genuine effect, previously unseen in metamaterials and somewhat exclusive to the continuous pattern. This discrepancy could only have resulted from the difference between the simulated and actual illumination conditions, which thus far had been routinely disregarded in the study of metamaterials: the common modelling approach assumed the complete coherence of incident light, while the spectroscopic measurements involved spatially incoherent light.

The nature of the discovered effect and, more specifically, the origin of the split resonance can be deduced from the distribution of electric field near the ZZnS Metasurface at the split's centre wavelength. Light wave polarised in the plane of the cross-section (———-polarization), which propagates upward as a beamlet until scattered by the nanostructure. While the incident wave is confined laterally to the

area of the patch, the transmitted and reflected waves can be pictured as spreading along the plane of the metamaterial far beyond these confines. The resulting field configuration indicates that the mechanism of light scattering by the ZZnS metasurface is extremely nonlocal. Since planar metamaterials do not diffract as a whole (i.e. do not support high-order diffraction modes) this mechanism must involve plasmon waves, which due to the continuity of the pattern can leak from a locally excited unit cell and propagate up and down the zigzags. In the ZZnS metasurface these waves are guided in the form of a mode confined to the nanoslits. It transports the excitation via the zigzag channels to other parts of the metamaterial, where it is radiated and interferes with the fields scattered there locally.

A strong local response plays a crucial role here not only by selecting the actual mode that mediates nonlocal scattering but also by rendering it nondispersive. As explained earlier, at the resonance of the zigzag metasurfaces the period of the plasmon waves has to fit inside one unit cell exactly.

Since in the near-IR the dispersion of surface plasmons in gold is close to linear, their wavelength can be estimated as $\lambda_g \approx \lambda\sqrt{(1+\epsilon_s)/2}$, where ϵ_s is the dielectric constant of the substrate. Correspondingly, at the resonance $\lambda_g/2 = 0.44\mu m$ matches almost exactly the length of zigzag segments, $0.45\mu m$.

This ensures that only $\lambda/2$-mode is sustained by the zigzag channels and all the unit cells engaged in nonlocal scattering will be driven to the resonance radiating most strongly. More importantly, this guarantees that the radiated fields are all in phase and, hence, add up to form planar wavefronts that stretch wide over the metamaterial, significantly increasing the spatial coherence of scattered light. Nothing of this kind happens outside the resonance.

The total transmitted field then arises as a superposition of the planar wavefronts propagating in the forward direction, which are sourced by different unit cells exposed to light. In the case of incoherent illumination, the exposed unit cells are excited with random phases and, hence, the planar wavefronts they produce do not interfere, preventing the transmission of a ZZnS metasurface from reaching maximum. Under coherent illumination all unit cells oscillate in sync, which ensures constructive interference of the scattered planar wavefronts and, as a result, maximal transmission.

The effect could also be summarised as follows. The field transmitted by a ZZnS metasurface arises as a superposition of the planar wavefronts propagating in the forward direction, which are sourced by different unit cells exposed to light. In the case of incoherent illumination, the exposed unit cells are excited with random phases and, hence, the planar wavefronts they produce do not interfere, preventing the transmission of the metamaterial from reaching its maximum (as illustrated in Figure 3.15a). This is evident from the expression for transmitted light intensity written down below in terms of the planar waves scattered non-locally as shown in Equation 3.1:

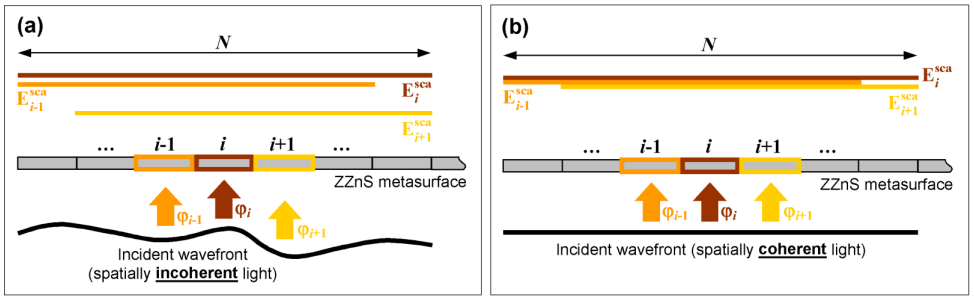

FIGURE 3.15: Panels (a) and (b) show schematically how the field transmitted by a ZZnS metasurface is formed under incoherent (a) and coherent (b) illumination. φ_i – is the phase of the excitation of i^{th} unit cell. E_i^{sca} is the amplitude of the planar wavefront that locally excited i^{th} unit cell produces via non-local scattering.

$$I^{tr} = \frac{c\epsilon_0}{2}\left(\sum_{i=1}^{N}|E_i^{sca}|^2 + 2Re\sum_{i=1}^{N}\sum_{\substack{j=1\\ j\neq i}}^{N}E_i^{sca}E_j^{sca*}\right) \tag{3.1}$$

where N is the number of unit cells, which are engaged in non-local scattering by each locally excited unit cell, and E_i^{sca} is the complex amplitude of the planar wave sourced by i^{th} unit cell through non-local scattering. Given that the phases of E_i^{sca} are random, all cross-terms in Equation 3.1 cancel out. Correspondingly, under coherent illumination all unit cells oscillate in sync with the exact same phase, which ensures that the cross-terms in Equation 3.1 all add up (constructive interference of the scattered planar wavefronts) and, as a result, maximum transmission is achieved (see Figure 3.15b).

Figure 3.16 shows a cross-section of the simulated ZZnS metasurface discussed earlier, in Section 3.5.1, while it is excited from the center only with light polarised parallel to the zigzag slits at a wavelength of $1.12\mu m$. The plane of the cross-section is parallel to the slits with the blue to red colours representing the real part of the electric field. The direction of incidence is indicated by the white arrow with the white dashed lines indicating the lateral extent of the incident wave.

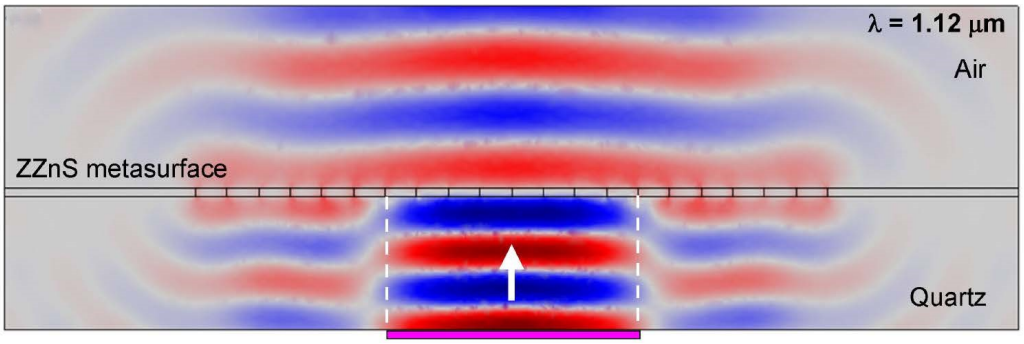

FIGURE 3.16: Simulation of the zigzag metasurfaces response to plane wave, incoherent illumination at $1.12\mu m$ (from [95]).

3.5.4 Zigzag nanowires under incoherent illumination

The results obtained for the wires version of metasurfaces agree and are consistent with the spectra measured for the slits version. However, the evidence of the split resonance is less pronounced, indicating perhaps stronger absorption. Furthermore, while in Figures 3.4 and 3.5, there was some evidence of the split for the chevron slits, in the corresponding case of wires, Figures 3.9 and 3.10, the split shows a smaller contrast and, furthermore, it is absent for the case of chevron wires.

In this case of a ZZnW metasurface the scattering process at the resonance is very similar to that revealed by the case of slits. The only differences are that nonlocal scattering is mediated by the plasmonic mode of the nanowires, while the field scattered forward propagates alongside the field of the incident wave.

Correspondingly, nonlocal scattering controls reflection of the ZZnW metasurface in the exact same way as it controls transmission of the complementary ZZnS design (in agreement with Babinet's principle): it reduces the intensity of light reflected by the ZZnW metasurface under incoherent illumination. This translates into an enhancement of transmission, as it was observed in the experiment.

3.6 The effect of coherent illumination on the transmission spectra of the zigzag metasurfaces

The zigzag metasurfaces have been modelled under both coherent and incoherent illumination but the spectra have so far only been recorded experimentally under incoherent illumination. The final piece missing was to measure the spectra under coherent illumination. To achieve this, 2 new metasurfaces were fabricated on a gold coated fused-quartz substrate. These consisted of a continuous ZZnS metasurface and a continuous ZZnW metasurface using the same design as discussed earlier, in Section 3.1. Both metasurfaces were $20 \times 20\mu m$ and were spaced further apart than usual to ensure that they could be illuminated individually. Additionally, a window matching the dimensions of the metasurfaces was milled into the gold to be used as a reference.

The experiment was carried out in Professor Pavlos Lagoudakis lab and was led by Dr Tamsin Cookson. A quasi-CW optical parametric oscillator (Chameleon Compact OPO) by Coherent with a tuning range of 1 - $1.35\mu m$ was used. The transmission response of the metasurfaces to coherent light was measured using a combination of the wavelength-tuneable laser and a broadband power meter. The Linearly polarised OPO output was focused on the samples to a spot with a diameter of $50\mu m$ by an achromatic lens with an $100mm$ focal length. Another $100mm$ lens was used to collect the transmitted light and direct it towards the power meter. The spectra were acquired

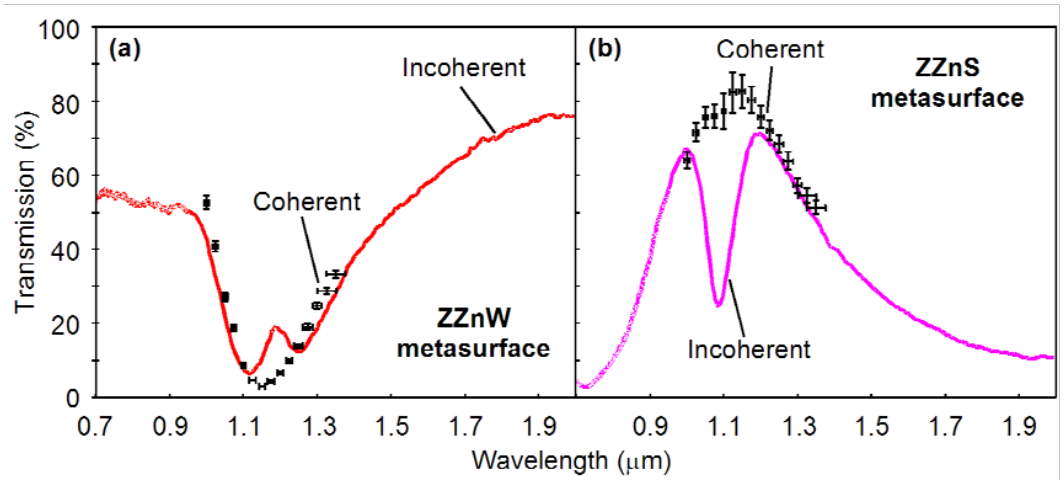

FIGURE 3.17: Transmission spectra of (a) ZZnW metasurface and (b) ZZnS metasurfaces measured under incoherent (solid lines) and coherent (crosses) illumination at normal incidence.

with a step of 25nm and normalised to the transmission of the fused-quartz window. The recorded spectra, shown in Figure 3.17, are missing the split resonance observed with incoherent illumination and feature a single resonance centred around 1.1μm.

3.7 The effect of a sharper angle between the zigzag arms

The angle between the zigzag arms was varied to explore the effect on the split resonance discussed earlier. The original design, with arms at 45° to the horizontal, was fabricated alongside 2 new designs with their arms at 51° and 59° to the horizontal. Figure 3.18 shows SEM images of the different zigzag slit structures used.

The following figures capture the main experimental results collected, with each angle variation shown in a different colour for the continuous, isolated and chevron designs. The design of these structures was discussed earlier in Section 3.1. As in the previous experiment, the incident light polarisation was set to be either perpendicular or parallel to the zigzag rows.

The results for the continuous zigzag slit metasurfaces are shown in Figure 3.19. As the angle of the zigzags was made tighter the split in the resonance is seen to reduce. The wavelength of the split is shifted to a higher wavelength for the 51° design.

Figure 3.20 shows the spectra from the chevron slit zigzag designs. The maximum transmission at the resonance increases and the split appears to move away from the central resonance to lower wavelengths for the larger angles.

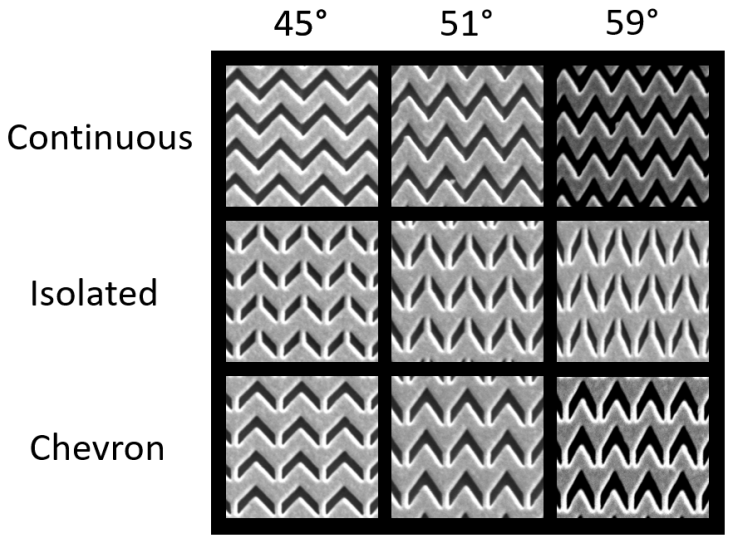

FIGURE 3.18: SEM images of the zigzag slit metasurfaces used. Images are not to the same scale.

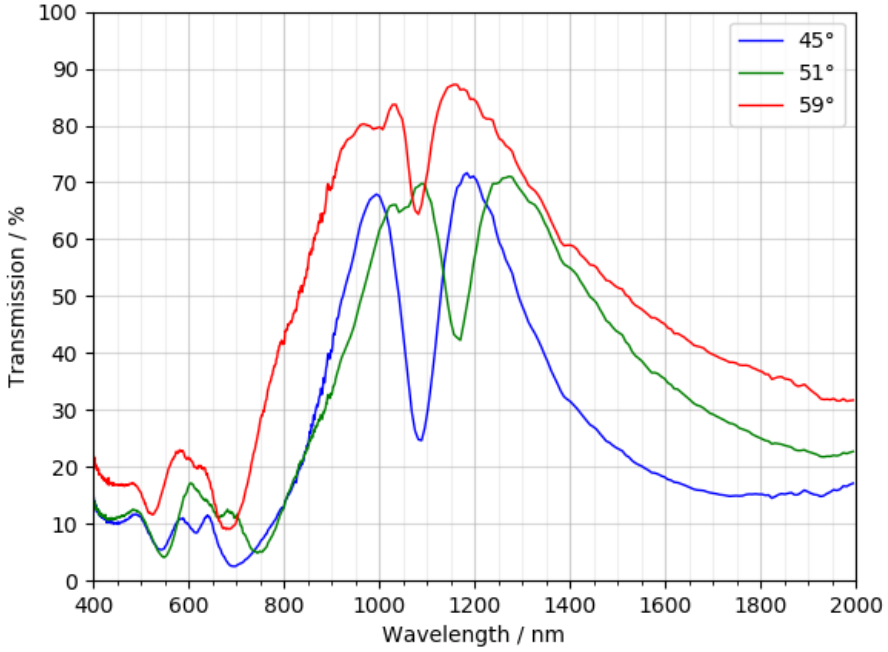

FIGURE 3.19: Transmission spectra of the three continuous zigzag slit metasurfaces with polarisation parallel to the zigzags.

All three of the isolated slit metasurfaces showed a well defined single resonance peak in their spectra. The wavelength of the resonance moves to higher wavelengths for the 2 larger angles investigated.

The next figures explore the zigzag wire metasurface designs. Figure 3.22 shows the results for the continuous zigzag wire metasurfaces. The double dip feature for 45°

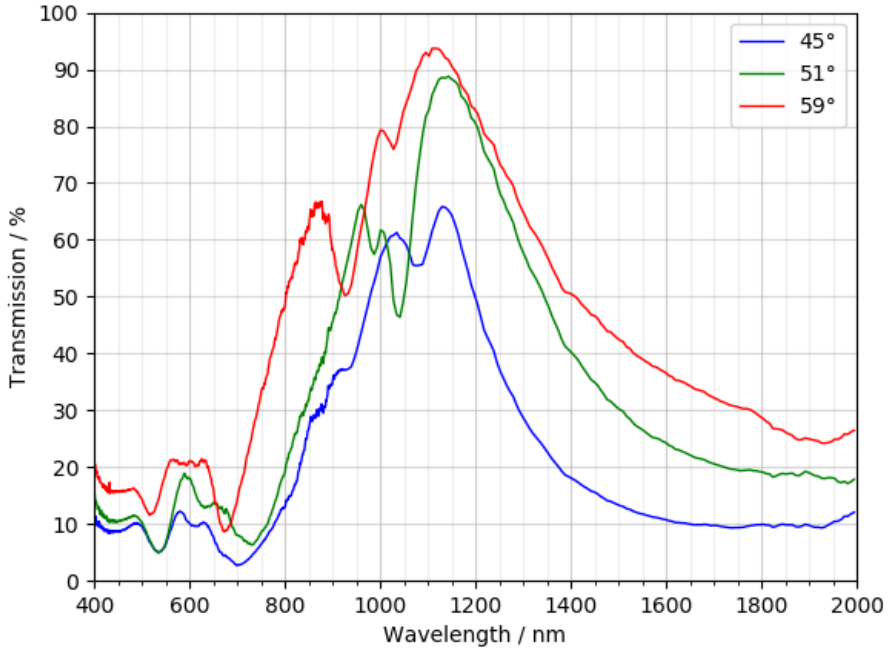

FIGURE 3.20: Transmission spectra of the three chevron zigzag slit metasurfaces with polarisation parallel to the zigzags.

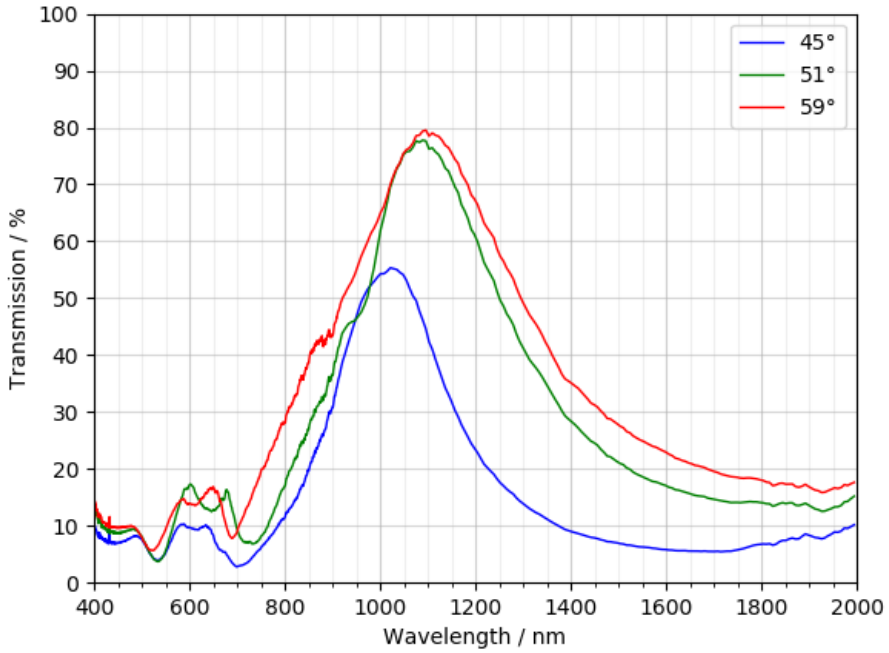

FIGURE 3.21: Transmission spectra of the three isolated zigzag slit metasurfaces with polarisation parallel to the zigzags.

which can be seen to be reduced as the angle is increased with an additional dip appearing at a slightly lower wavelength.

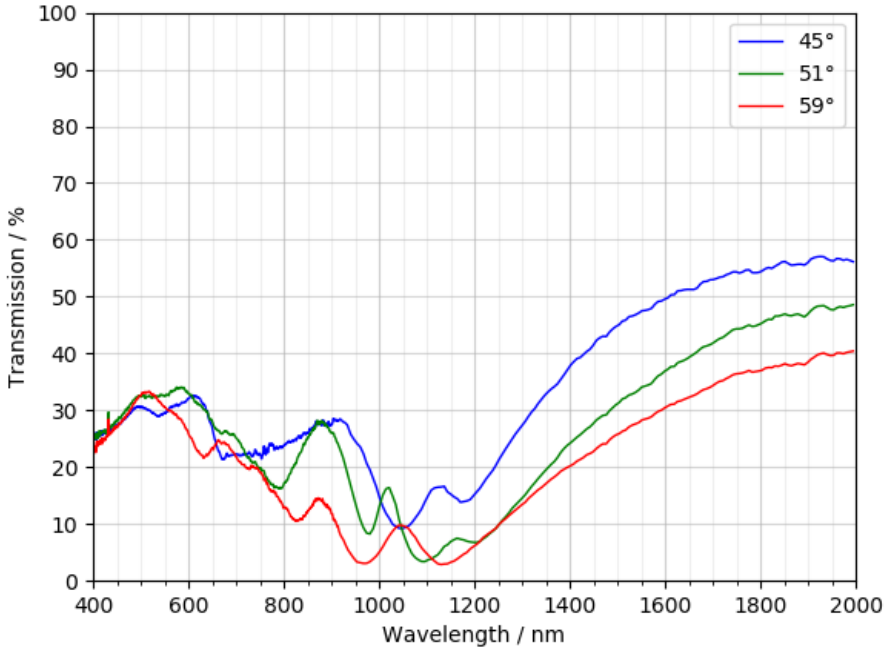

FIGURE 3.22: Transmission spectra of the three continuous zigzag wire metasurfaces with polarisation perpendicular to the zigzags.

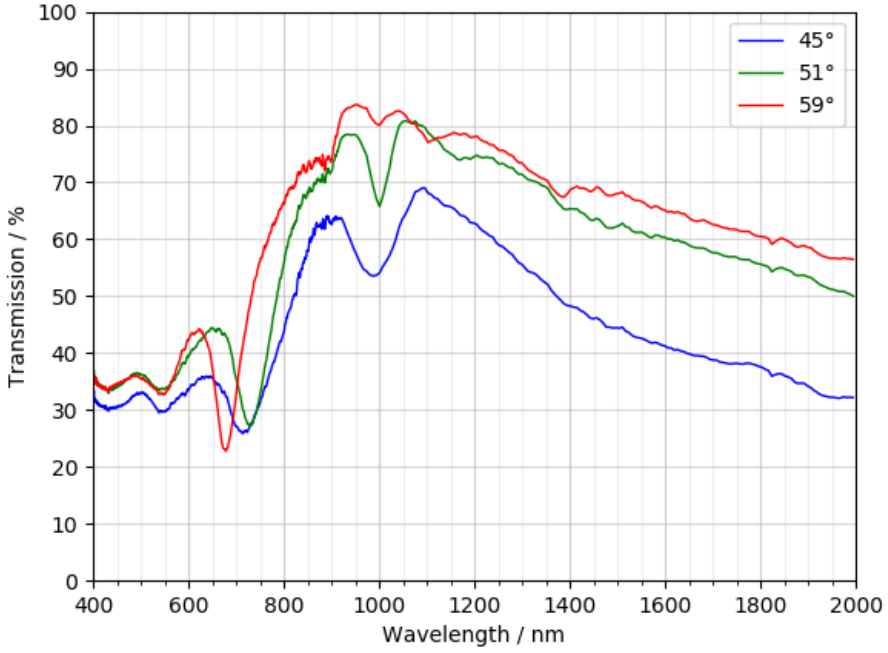

FIGURE 3.23: Transmission spectra of the three continuous zigzag wire metasurfaces with polarisation parallel to the zigzags.

Looking at the opposite polarisation orientation for the continuous zigzag wire designs the same split resonance feature observed for the continuous zigzag slit

metasurfaces is seen. It is broader and less defined for the wires designs as they were not optimised for this polarisation. As the angle of the zigzags is increased the split in the resonance becomes narrower for 51° and then almost disappears for the 59° sample.

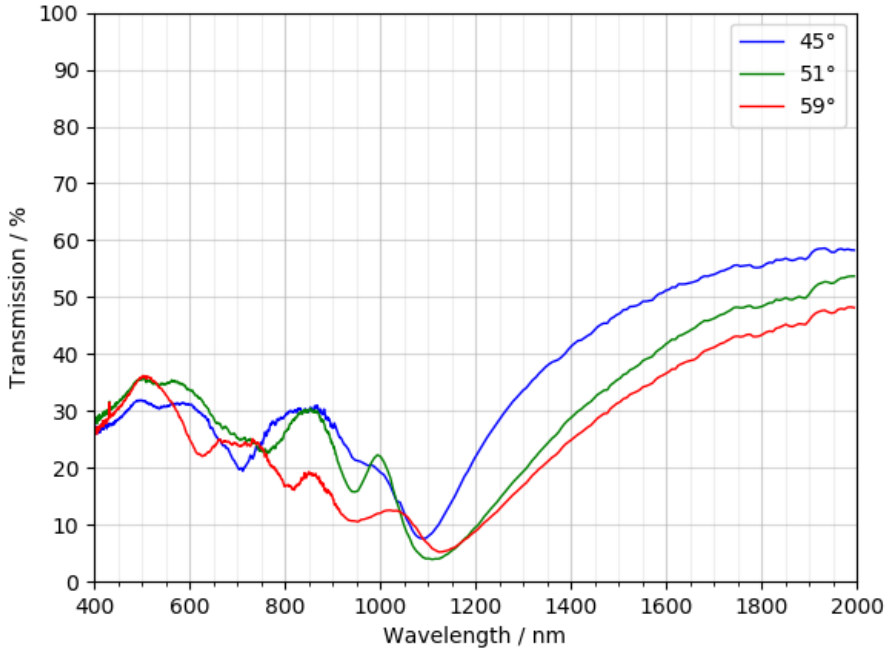

FIGURE 3.24: Transmission spectra of the three chevron zigzag wire metasurfaces with polarisation perpendicular to the zigzags.

For the chevron wire structures a single dip is observed for the 45° design with an additional dip appearing at lower wavelengths for the larger angles. This is shown in Figure 3.24.

Figure 3.25 shows the spectra for the isolated wire designs. For 45° and 51° a single dip can be seen. For 59° a second dip appears for lower wavelengths.

The reduction of the split resonance feature, as the angle is increased, can be explained by increased losses stemming from the sharper corners of the zigzag geometry and by the larger path length the plasmons must take to travel along the zigzags. These increased losses mean that the plasmons originating from different points along the zigzags have less chances to interfere with each other leading to a reduction of the split resonance observed.

The centre wavelength of the resonance is determined by the size and the geometry of the unit cell, as discussed earlier. In general, each unit acts as a resonator thus the resonance can be controlled by altering its design, in particular the length of the arms. In this part of the experimental work, different angles between the arms were considered, but in doing so the length of the arms did not remain constant. Hence,

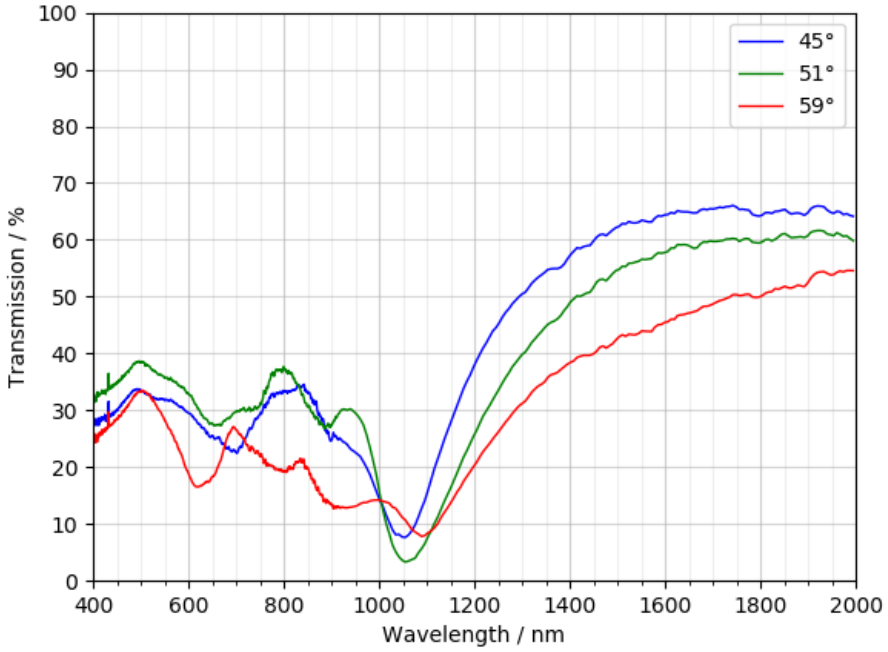

FIGURE 3.25: Transmission spectra of the three isolated zigzag wire metasurfaces with polarisation perpendicular to the zigzags.

multiple aspects of the designs were altered, making more precise conclusions about the effect of the varying angle more challenging. An extension of this project would need to consider these aspects separately.

Concluding this part of the project, the split resonance feature was observed in the new designs with different angles. As the angle was increased it was seen that the split in the resonance decreased in contrast. However, exploring these different designs and angles, with the aim of determining the optimum design did not lead to a stronger effect, thus the original design proved to be the most successful.

3.8 Varying the angle of incident illumination

To explore further this effect, a separate study was carried to explore the dependence of the spectral response on the experimental conditions, namely the tilt of the samples at different degrees and planes with respect to the incident light. The aim was to investigate how the split resonance in the optical transmission spectra varied with the angle of incidence.

The following figures present the impact of tilting the sample on the spectra. Figures 3.27 and 3.28 considers the case of slits/wires being tilted so that the zigzags are

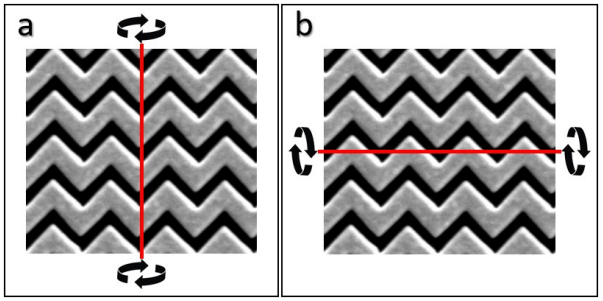

FIGURE 3.26: Rotation axis with zigzags down the slope, (a), and along slope ,(b).

running “down the slope”. Figures 3.29 and 3.30 show the case where the zigzags are running ”along the slope”. The axis of these rotations are defined in Figure 3.26.

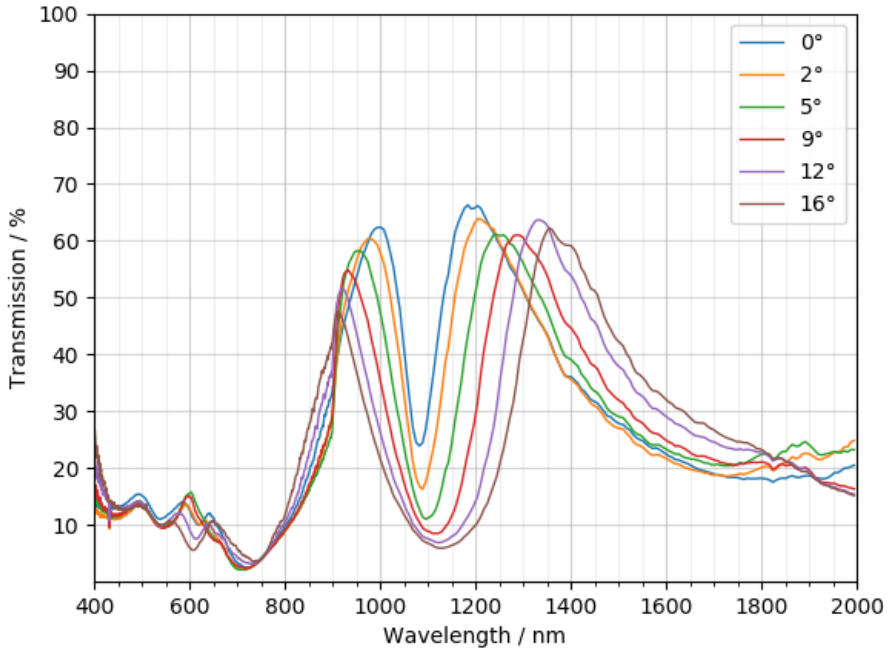

FIGURE 3.27: Spectra of continuous zigzag slit metasurface as inclination angle is increased with the zigzags going down the slope. Polarisation parallel to the slits.

For both the nanowire and nanoslit samples, shown in Figures 3.27 and 3.28, the split in the resonance becomes broader and deeper as the incidence angle is increased. The central wavelength of the split becomes slightly red-shifted at the larger angles.

Figures 3.29 and 3.30 show the spectra as the sample was inclined on the opposite axis. In this case, the dependence on this tilt angle is much less pronounced. The slits, shown in Figure 3.29, show an overall decrease in transmission around the split resonance with the lower wavelength half having the largest change. In Figure 3.30 we can see that the nanowires metasurface shows very little change when the tilt angle

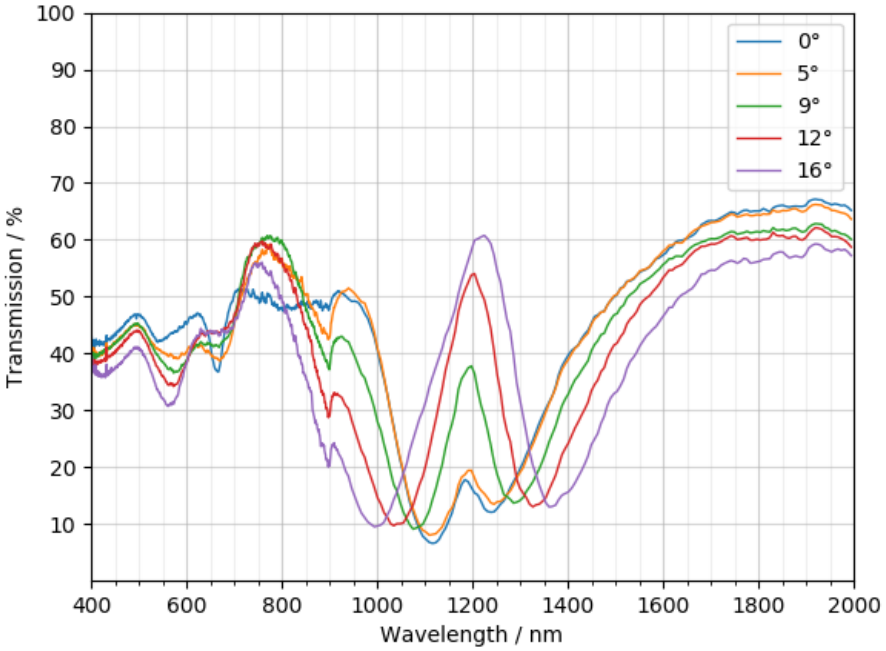

FIGURE 3.28: Spectra of continuous zigzag wire metasurface as inclination angle is increased with the zigzags running along the slope. Polarisation perpendicular to the wires.

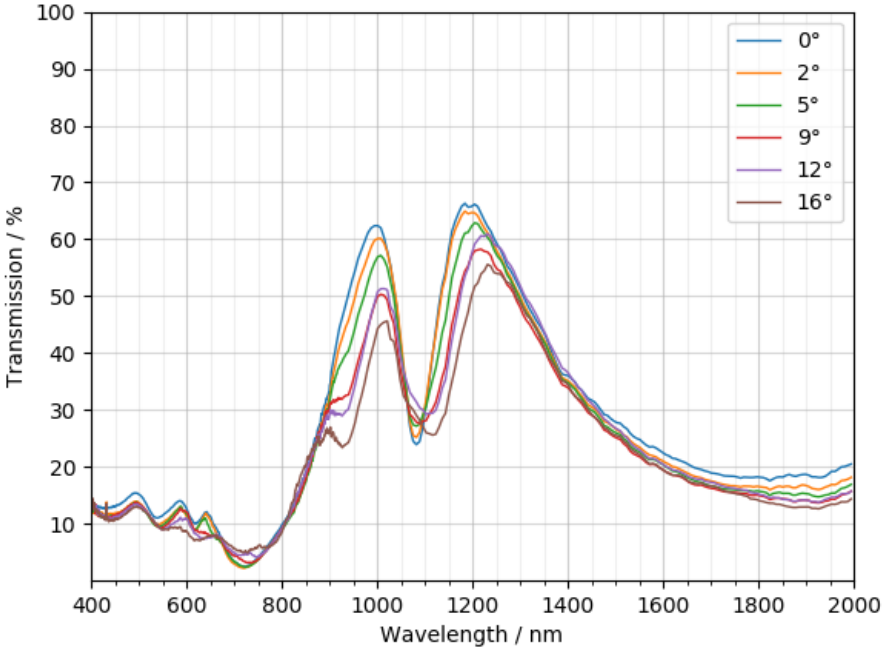

FIGURE 3.29: Spectra of continuous zigzag slit metasurface as inclination angle is increased with the zigzags running along the slope. Polarisation parallel to the slits.

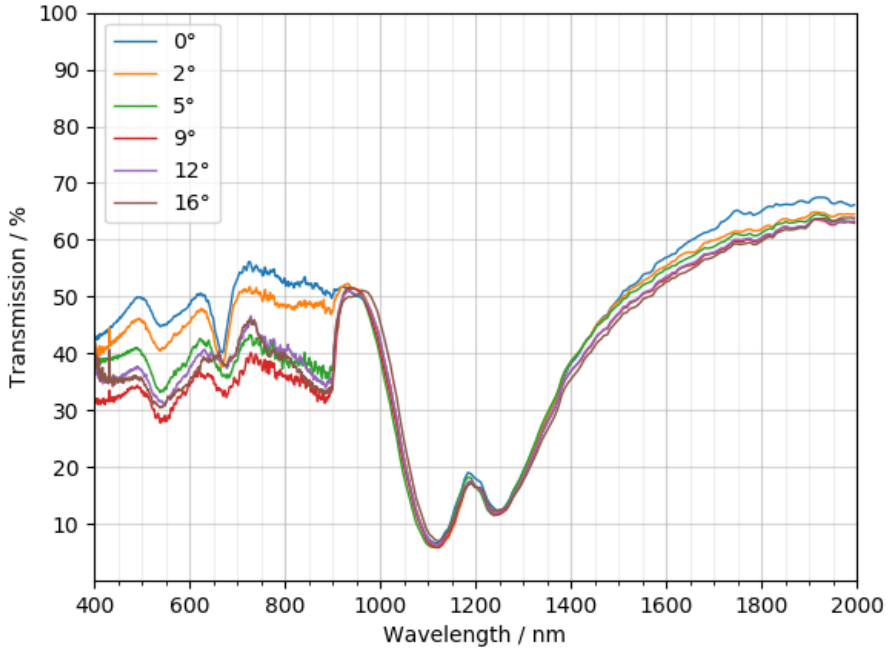

FIGURE 3.30: Spectra of continuous zigzag wire metasurface as inclination angle is increased with the zigzags running along the slope. Polarisation perpendicular to the wires.

was increased with the largest decrease in transmission being below 900nm away from the split resonance.

The enlarging of the split in the resonance observed for the zigzag slit samples can be explained by the effect discussed previously, in Section 3.5.3 and shown in Figure 3.16, where the metasurface scatters light of the resonant frequency in the form of a plane wave. This scattered plane wave will propagate perpendicular to the plane of the metasurface and therefore, as the angle of incidence is increased, more light of the resonant frequency will be redirected from the beam path through the spectrometer leading to a reduction in the observed transmission. As discussed in Section 3.5.4, the ZZnW metasurface acts as the inverse to the ZZnS which explains the enhancement of the transmission observed as the angle of incidence is increased.

Changing the angle of incidence of the light illuminating the sample was another experimental parameter that was explored to further investigate the observed split in the resonance. This part of the experimental work was intended as a proof of principle investigation to provide an additional control on the observed split, in particular the mechanism of the directional selectivity and its effect on the spectra. A more in-depth understanding of the trend observed requires follow-on modelling that would constitute future work and the extension of this project.

3.9 Conclusions

In this chapter, planar metamaterials were shown as a powerful paradigm of optical engineering, which enables one to control the flow of light across structured material interfaces in the absence of high-order diffraction modes. Here, planar metamaterials, formed by nanopatterned metal films, respond differently to incoherent light, depending on the design of the zigzag pattern.

Experimentally verified, and confirmed via rigorous numerical modelling that the optical response of metallic planar metamaterials (homogeneous metasurfaces that do not diffract as a whole) may vary dramatically with the spatial coherence of incident light. Correspondingly, any continuous periodic metamaterial pattern should exhibit the effect provided that its unit cells locally support the resonant excitation of the symmetric $\lambda/2$-dipole mode.

In future work, different shapes of the nanostructure could be explored, for example, an array of meanders, the so-called fish-scale pattern [96] could be among the potential candidates. Further investigation into variations in the zigzag design could also include shallower angles of the zigzags or the case half way between the slits and wires designs, where the surface is its own inverse. Further simulations should be undertaken to model the response of the zigzag metasurfaces as the angle of incident light is varied. A more complex simulation method using COMSOL reproduced the signature double peak feature which could be explored further.

Following this investigation of the different zigzag designs, and their influence on the transmitted and reflected light, the next part of the project expanded on the exploration of nano-structured metamaterials, focusing on those consisting of achiral units and their potential to induce optical activity.

Chapter 4

Specular optical activity with metasurfaces

Specular optical activity effect manifests itself as rotation of light polarisation upon reflection from chiral materials and diffusive scattering from chiral liquids. It is an extremely weak phenomenon which has been rarely studied and reported in literature or, indeed, used in practical applications. One exception was the strong specular optical activity observed at microwave frequencies for oblique incidence of an incident beam on a reflective planar metamaterial [40]. However, the demonstration of the effect in the visible domain has remained difficult to achieve mainly due to the challenging nanoscale fabrication.

The results show a strong effect from a single reflection from our nano-structured non-magnetic metal films, so called metasurfaces, where it mimics longitudinal magneto-optical Kerr effect. While the magneto-optic Kerr effect is a well-known phenomenon of rotating light polarisation on reflection and is commonly used to characterise magnetic materials, the new, subtle effect explored here investigates the contribution to polarisation rotation from nanostructured metallic films that are not magnetic themselves.

4.1 Optical activity

There are many examples of materials which have the ability to rotate the polarisation of light. This effect is called optical activity and is usually observed from the transmission of linearly polarised light through structurally chiral materials, such as quartz crystals or solutions of chiral molecules such as sugars. Optical activity is also present in some liquid crystals, mainly in cholesteric liquid crystals that form a helical order with their molecules. Their spiralling structure is present with the average

direction of the molecules twisting around an axis perpendicular to the long molecular axis. Incident, linearly polarised light is rotated by such helix and if its pitch is comparable to the wavelength, then reflected light of a single wavelength can be observed. The cholesteric pitch, and thus the wavelength of the reflected light can be changed with temperature, where the pitch decreases for increasing temperature. Temperature was therefore used from early on to tune the response of chiral systems and they found applications in thermometers, guest-host colour displays and lasers [97].

Chirality can be expressed as asymmetry between the refractive indices for right and left-hand circular polarised light (Δn), so the light polarisation undergoes optical rotation by an angle determined by

$$\Delta\phi = \frac{\pi L \Delta n}{\lambda} \tag{4.1}$$

where L is the thickness of the medium and λ is the wavelength of incident light [98].

If in a medium the absorption coefficients for the right and left-hand circular polarisations are different, the effect called circular dichroism [99], optical activity also takes place.

Manipulation of light polarisation in bulk metamaterials has been extensively explored over the past several years [10]. For example, photonic metamaterials were fabricated, consisting of a lattice of submicron gold helices, which acted as a broadband circular polariser [100]. Other metamaterial designs of chiral metamolecules included sets of two identical, twisted planar metallic coils, crosses and rosettes [101].

Exploring metasurfaces for optical activity offers a clear advantage in terms of more straightforward fabrication. Indeed, such planar metamaterials, when homogeneously patterned, act on light polarisation [29], but their effect is not confined to its rotation and more complex polarisation patterns can emerge. The underlying mechanisms [102] are not just stemming from the asymmetry of refractive indices or absorption and the medium chirality in its structure is no longer required to observe asymmetric light transmission.

While polarisation rotation is often described considering transmission through an optically active medium (as in Equation 4.1), for planar metamaterials, the rotation is due to reflection from the surface. Upon reflection from a chiral material the polarisation of light will be rotated by a much smaller amount when compared to transmission through the material [103]. This is due to the light only interacting with a few atomic layers at the surface, in contrast to propagating through the bulk of the material.

4.2 Polarisation control with metasurfaces

Giant specular optical activity from a single reflection off a metasurface has been demonstrated in the microwave region of the spectrum [40; 104; 105]. The concept exploited an array of oriented, achiral metamolecules in combination with particular direction of propagation of incident light, such as oblique incidence.

The effect was demonstrated on metasurfaces with arrays of asymmetric, split-ring metamolecules, which was an example of a unit without two-fold rotational symmetry, that together with together with oblique incidence of an illuminating beam forms a chiral system.

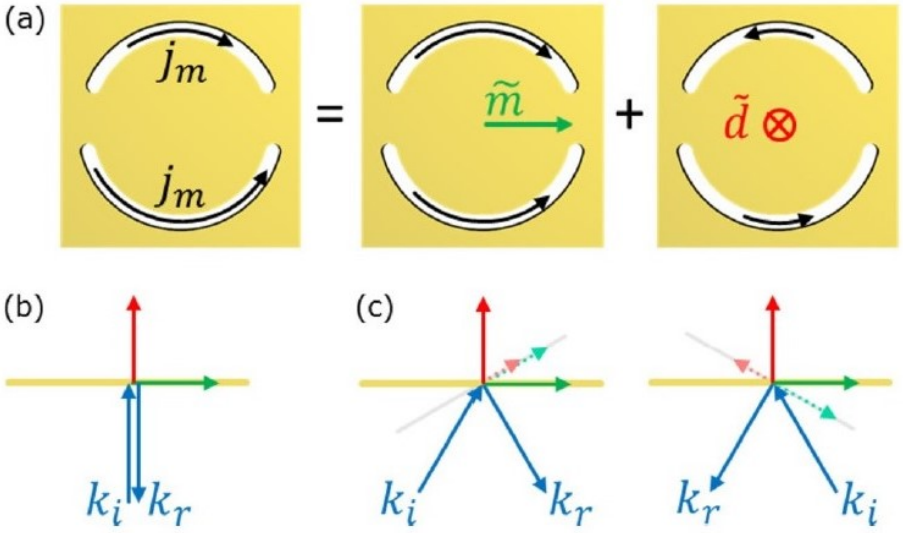

FIGURE 4.1: (a) - Metamolecule with fictitious magnetic currents and resultant fictitious electric and magnetic dipoles. (b) - Interaction at normal incidence [40].

Figure 4.1 presents a metasurface consisting of an array of double split circular slits [40]. At the metamolecule level the optical activity is due to simultaneously excited electric and magnetic dipoles in the structure, just as with conventional optical activity. These dipoles are the result of fictitious magnetic currents oscillating along the length of the slits. The fictitious currents oscillate with a phase difference dependant on the frequency of incident radiation and can oscillate in two modes, symmetric and anti-symmetric. The symmetric mode where they oscillate together results in a fictitious magnetic dipole in the plane of the surface while the anti-symmetric mode results in a fictitious electric dipole normal to the surface. This is shown in Figure 4.1(a). When both dipoles radiate differently polarised fields in the direction of the reflected wave certain effects can be observed. At normal incidence, shown in Figure 4.1(b), only the magnetic dipole can contribute to the reflected wave so there is no effect. Whereas at non-normal incidence, shown in Figure 4.1(c), both dipoles contribute leading to the polarisation state of the reflected radiation being altered, except when the plane of incidence is parallel to the plane of symmetry of the

structures. Therefore, at other than normal incident angles, both dipoles can contribute which leads to the polarisation state being altered. The change is due to the circular dichroism and circular birefringence exhibited by the metasurface. In general, the contribution from each of these effects varies with the frequency of the incident radiation.

In summary, optical activity occurs when both dipoles radiate differently polarised fields in the direction of the reflected wave

Exploring this effect with the microwaves Plum at al. [40], constructed a sample consisting of $1mm$ wide slits cut into a $1mm$ thick aluminium plate. Each metamolecule comprised of a $15 \times 15mm^2$ unit cell with a $1mm$ wide circular slit, of $6mm$ radius, split at two positions, leaving two arcs: one subtending an angle of 140° and the other 160°.

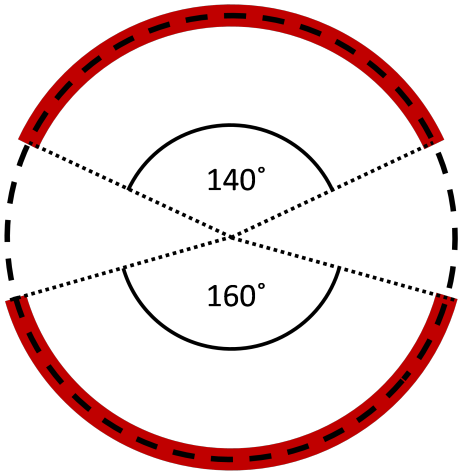

FIGURE 4.2: Design of a metasurface for observing optical activity at microwave frequencies [40].

The change to the polarisation state is caused by the circular dichroism and circular birefringence of the surface. Circular dichroism is the difference in reflectivity between left and right circularly polarised radiation whereas circular birefringence is the difference in the phases of the reflected components.

Characterising specular activity, the metasurface involved considering the linearly polarised, reflected light as a combination of left- and right-hand polarised light. Following the analysis outlined in [40], in the first step, the electric field of the reflected light E^r:

$$E_i^r = r_{ij} E_j^{inc} \tag{4.2}$$

is related to the incident light E^{inc} through right-handed (RCP, $i = +$) and left-handed (LCP, $i = -$) circularly polarised light components. The reflection coefficient is defined as:

$$R_{ij} = |r_{ij}|^2 \tag{4.3}$$

Specular circular dichroism, which can be also described as circular differential reflectance ΔR is defined as the difference between the reflection coefficients between incident RCP and LCP waves. Given that on reflection from a homogenous surface, the handedness of circularly polarised waves is reversed, specular circular dichroism can thus be calculated from:

$$\Delta R = R_{-+} - R_{+-} \tag{4.4}$$

Next, angle of rotation $\Delta\theta$ experienced by an incident linearly polarised wave upon reflection, the specular circular birefringence effect, can be defined as:

$$\Delta\theta = \frac{1}{2}\left(arg(r_{-+}) - arg(r_{+-})\right) \tag{4.5}$$

Figure 4.3 presents the main experimental results on specular reflection spectra of a metasurface for an angle of incidence of 30°. This particular metasurface has a resonance at approximately $9.4GHz$. As Figure 4.3(a) shows, reflection coefficients are different for RCP and LCP components, thus from these results the presence, as well as the magnitude, of specular circular dichroism can be extracted. The phases are also different and hence specular circular birefringence was also detected.

The most interesting is the narrow band around $9.4GHz$, at a 30° incidence angle, this double split ring metasurface exhibited a large circular birefringence, but no circular dichroism meaning the surface acts as a pure polarisation rotator. Using this metasurface, Plum et al. [40] demonstrated a 17° polarisation rotation from a single refection at $9.4GHz$.

4.3 Designs of achiral Metasurface for Optical Activity upon Reflection

For this thesis, in order to explore this effect at optical wavelengths new metasurfaces were explored. This involved the fabrication of such nano-structured metal surfaces featuring a specially design resonant achiral nano-pattern. The metamolecules of this metasurface consist of a pair of slits of different length residing in a square $250 \times 250nm$ unit cell, a simplified design for the ease of fabrication. Samples with various sizes of slits (ranging from $50nm$ to $200nm$) were fabricated. Reference samples with single slits and double slits of equal length were also fabricated. The

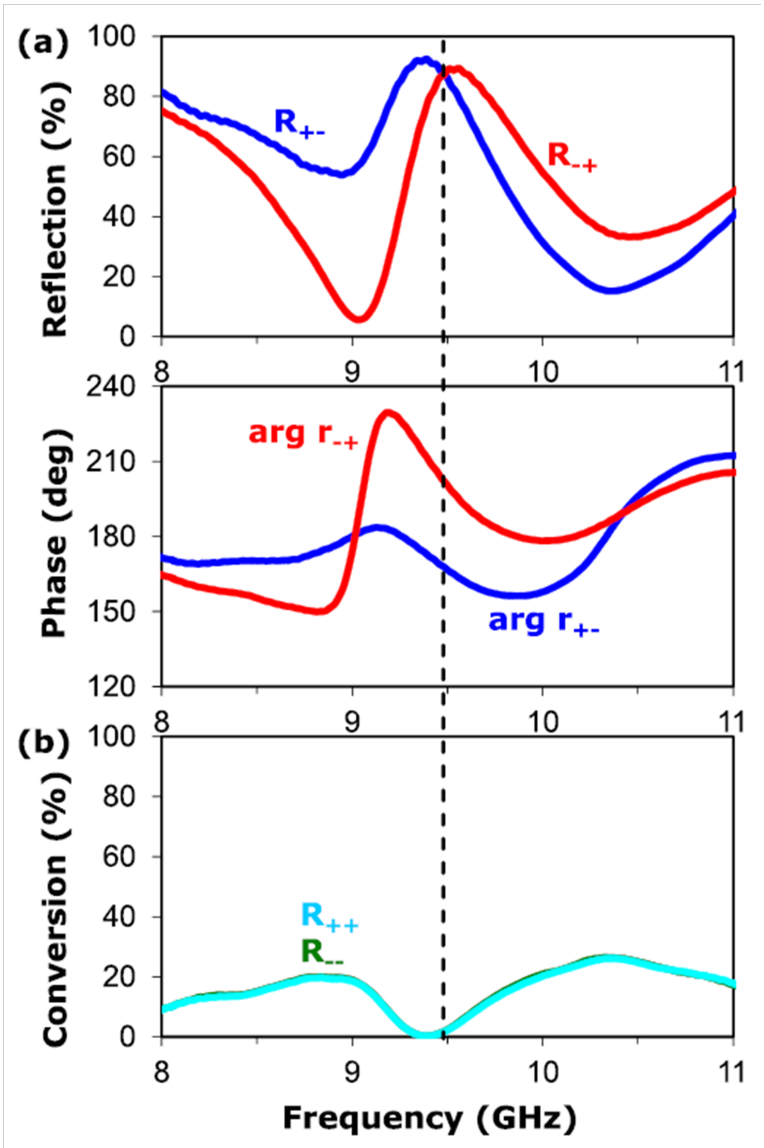

FIGURE 4.3: Reflection spectra for left and right polarisations [40].

metal for the samples was changed from aluminium, used in the microwave regime, to gold to take advantage of its plasmonic properties. The slits were milled, using a focused ion beam, into an $80nm$ thick gold film that had been deposited on a fused quartz substrate. Each sample consisted of 80×80 metamolecules resulting in a $20 \times 20\mu m$ active region.

The schematic design for the new metasurface is shown in Figure 4.4 with typical dimensions indicated.

Figures 4.4 and 4.5 show that an individual metamolecule consists of a pair of slits, each of different length. Two main metasurfaces designs were therefore considered, both achiral and with the same sub-wavelength period. One had an asymmetric design with two slits of different length per unit cell and the second, reference metasurface had a symmetric design featuring a single slit per unit cell. Samples

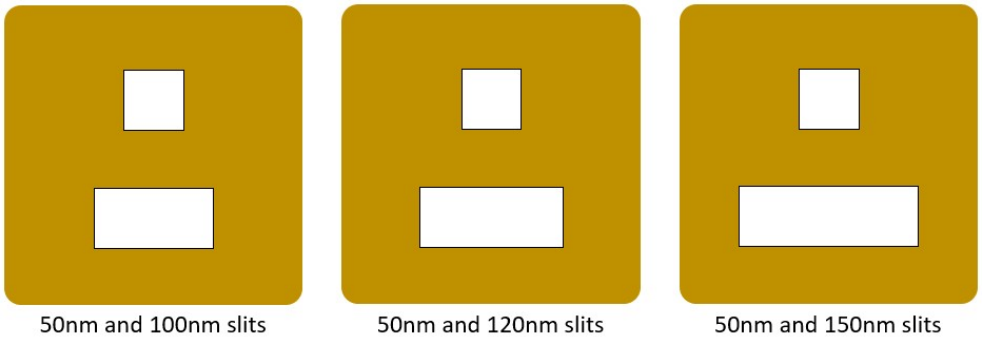

FIGURE 4.4: Design of the metasurface for optical activity at optical wavelengths.

consisting of single and double slits of the same length were fabricated to act as a reference.

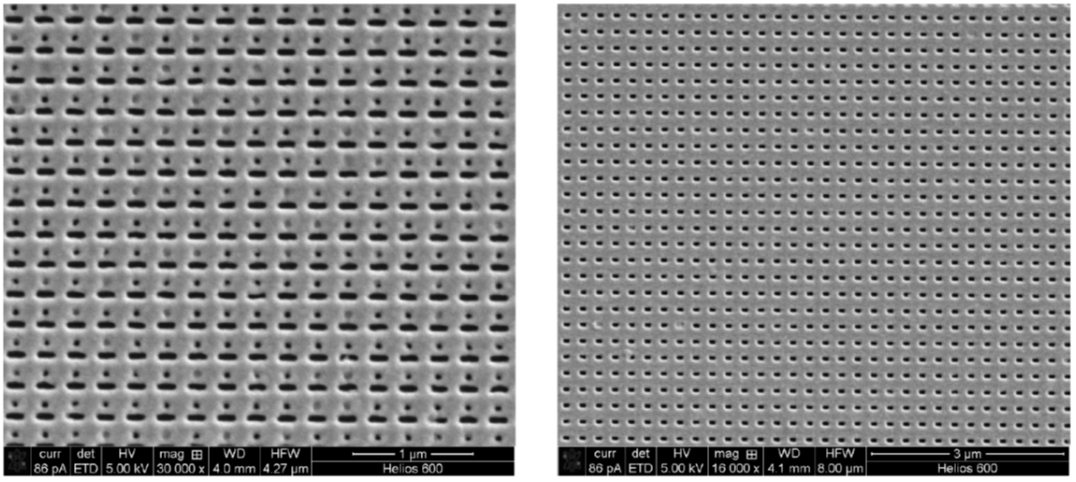

(a) Asymmetric double slits (b) Single slit reference

FIGURE 4.5: SEM image of symmetric and asymmetric designs. The scale bars are indicated at the bottom of each panel, namely 1 μm for the a) panel on the left and 3 μm for the b) panel on the right

.

4.4 Experiments with optically active metasurface system

The metasurfaces were investigated using a magneto-optical Kerr effect microscope, the NanoMOKE3 from Durham Magneto Optics Ltd. It provides the ability to view samples simultaneously in reflection mode and polarisation rotation mode (Kerr signal). The core principles behind the NanoMOKE3 measurement and imaging techniques were developed in 2003, to provide high sensitivity measurements of nanostructures and capture maps of magnetic domains on the surface of samples [106]. The instrument is a very powerful tool, but its main purpose is the investigation of magnetic materials and as it is an all-in-one system, is not particularly flexible. For example, it is not possible to freely adjust the angle of incidence which would be an

interesting parameter to explore for the different slit designs considered in this work. Nevertheless, the ease of access to this instrument and the nature of the project pursued as part of this thesis, namely providing an initial proof of concept, justified the use of the NanoMOKE3.

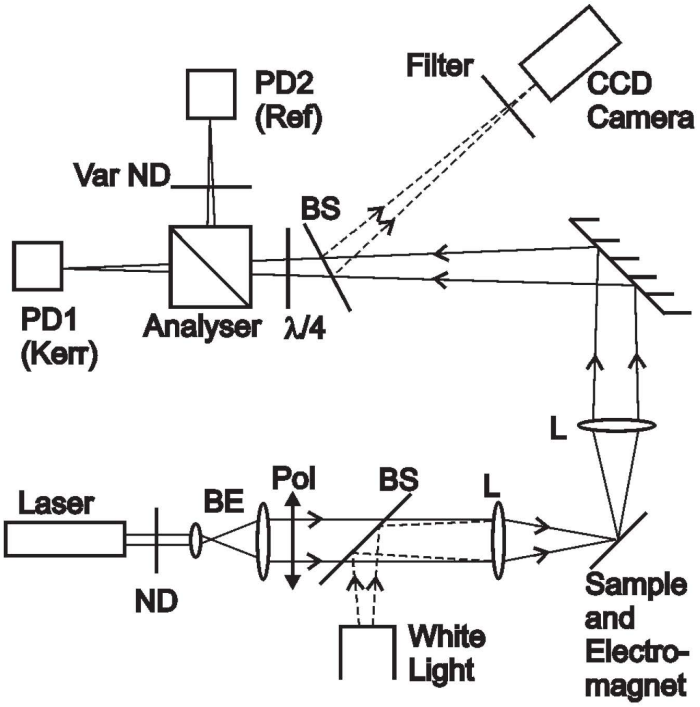

FIGURE 4.6: Schematic diagram of MOKE instrument with the main optical components indicated: neutral density filter (ND), beam expander (BE), polariser (Pol), beam splitter (BS), lens (L), quarter-wave plate λ /4; variable neutral density filter (VarND), photodiode detector (PD1, PD2) to collect the Kerr and reference signals, respectively (from [106])

Figure 4.6 presents a schematic diagram of the design and the main optical components. A linearly polarised beam is reflected off the sample and in the case of a passive surface, the reflected light remains polarised in the same plane as the incident beam. If optical activity is present, the light becomes elliptically polarised and with its major axis rotated from its initial incident polarisation direction. This is usually expressed as the rotation of the major axis with respect to the plane of polarisation of the incident light beam and the ellipticity factor, so called Kerr rotation and Kerr ellipticity, respectively [107].

On reflection from the sample, the light passes through the quarter-wave plate and then the analyser, namely a Glan–Taylor polarising analyser, which directs the transmitted and reflected beams to be detected by the photodiodes. The main role of this combination of quarter-waveplate and analyser, both being adjustable, is to calibrate the system. For example, through the rotation of the quarter-waveplate and adjusting the position of the analyser, its fast axis can be set to match the polarisation of the reflected beam and thus null the effect of rotation of that axis. The settings of the

polarisers/analyser and the waveplate are important for the correct offsetting of any depolarisation, non-Kerr rotation or ellipticity that contribute to the signal [106]. A background field can come from the variation of the incidence angles of the light beam reflecting from the surface of the sample and its micro or nanostructure. The inclusion of the neutral density filters also allows for setting the intensities of the Kerr and reference signal to be comparable for the ease of analysing the results.

The main goal of this experimental study, however, was not the precise determination of the rotation of polarisation, but exploring if the effect can be detected from the asymmetric slits and if so, to provide initial data on the size and the geometry of the samples that yield the strongest effect.

In the results presented here, the Kerr microscope measured polarisation rotation of linearly polarised light, at the wavelength of $660nm$, reflected off the samples at 30° from the normal to their surface, forming the Kerr signal. Both reflection and Kerr rotation modes were collected.

Figure 4.7 presents a photograph of the NanoMOKE3 set up and the arrangement for the incident and the reflected beam.

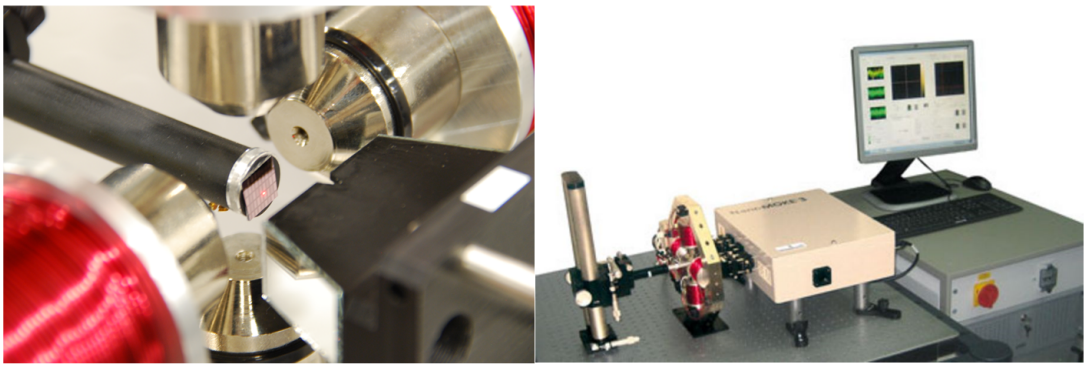

FIGURE 4.7: Pictures of the NanoMOKE3 microscope used.

The geometry of the incident and the reflected beams are illustrated on Figure 4.8, indicating linearly polarised $660nm$ light incident on the sample and then collected for analysis.

A series of images were collected and analysed. An example of a raw imaged collected is shown on Figure 4.9. As shown, the microscope can image the surface in reflection and polarisation rotation modes. Images were taken at regular intervals as the samples were rotated through 360° and then data was then extracted from these images.

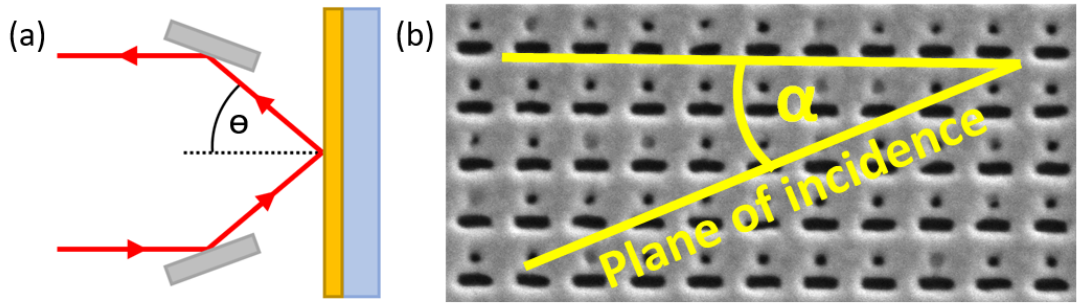

FIGURE 4.8: Diagrams showing the angle of incidence (a) and the angle of the plane of incidence with respect to the samples (b). he size of each unit, a set of two asymmetric slits, is 250 nm.

.

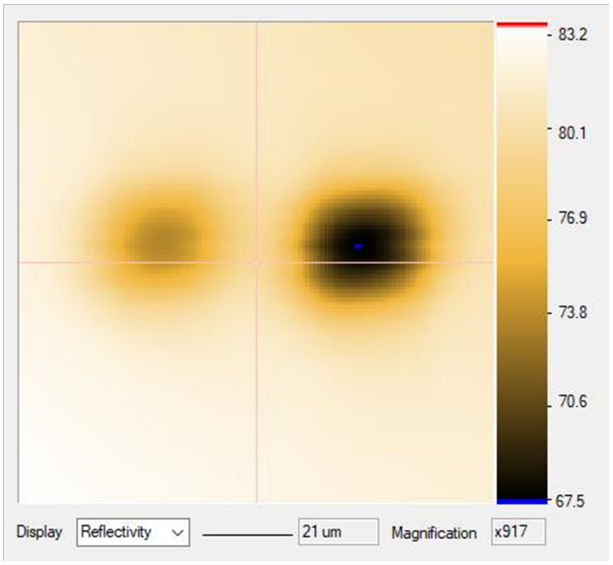

FIGURE 4.9: Example of reflection image output. The colour bar represents the percentage of reflection. The line at the bottom is the scale bar indicating the size of the area probed.

4.5 Main experimental results specular optical activity

The experiments were carried out on several sets of samples, with slits of different dimensions and design as shown on SEM images in the previous section. Multiple measurements were taken to detect and confirm the effect as well as check the repeatability. This section presents the main results with the measurements taken shortly after fabrication and they demonstrate the strength of the effect, while the following section includes examples of supplementary measurements.

Multiple experiments were carried out with a NanoMOKE3 microscope at Dr Gavin Stenning's, Materials Characterisation Lab at the Rutherford Appleton Laboratories. Another set of experiments undertaken for this thesis was carried out at the

University of Cambridge using the same NanoMOKE instrument, which additionally included an extra magnifying optics.

Each sample was mounted on a holder, as shown in Figure 4.7 that allowed it to be rotated while keeping the same incidence angle. During imaging the sample were rotated in their plane to extract the contribution of the metamaterial anisotropy to the Kerr signal. Therefore, the samples were rotated with respect to the plane of incidence keeping the incidence angle constant. Reflectance and Kerr rotation images were taken for each angle. From these images the Kerr signal from the sample could be determined.

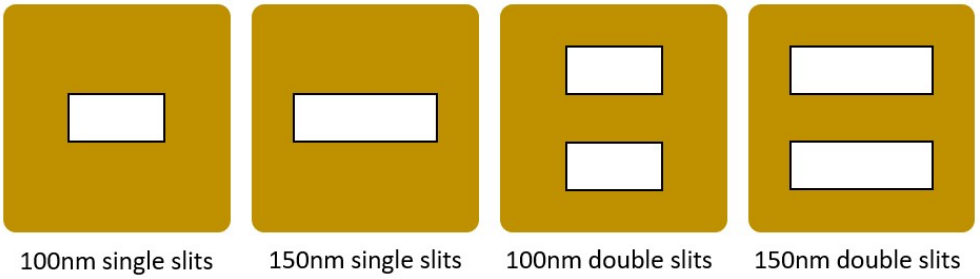

FIGURE 4.10: Design of the reference metasurfaces.

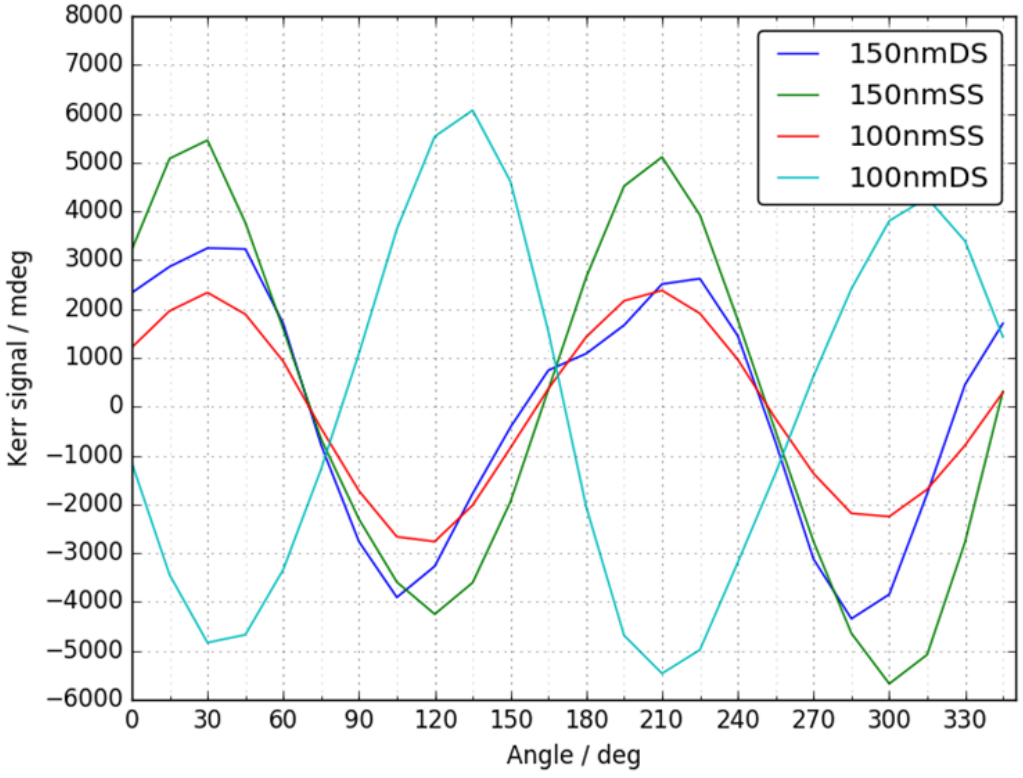

FIGURE 4.11: Measured Kerr signal against angle between the plane of incidence and the sample slits for single slit (SS) and double slit (DS) samples.

First set of data, shown on Figure 4.11 presents results collected for the reference samples with either single slits (SS) or with different sizes of double slits (DS) – all

symmetric samples. As expected from the experiments, and the analysis, in the microwave regime, standard sine-like signal was detected, without any additional prominent features. The origin of the difference in their amplitudes and in the smoothness of the curves is likely to originate from the experimental procedure and the precision of mounting the sample exactly in the middle of the holder to ensure precise rotation. This was difficult to achieve, given some degree of undesired movement of the holder while rotating. Such technical issues are most likely responsible for the differences in those symmetric curves, especially for the $100nm$ double slits results.

As can be observed on figure 4.11, the reference curve for the $100nm$ DS case is $180°$ out of phase with the other metasurfaces. This is likely due to an experimental error that was not realised during the measurement, stemming from the calibration of the machine. This reference plot was nevertheless included to show its regular and smooth shape, as expected.

The symmetric samples were then replaced by three different asymmetric samples ones and the results are presented on Figure 4.12.

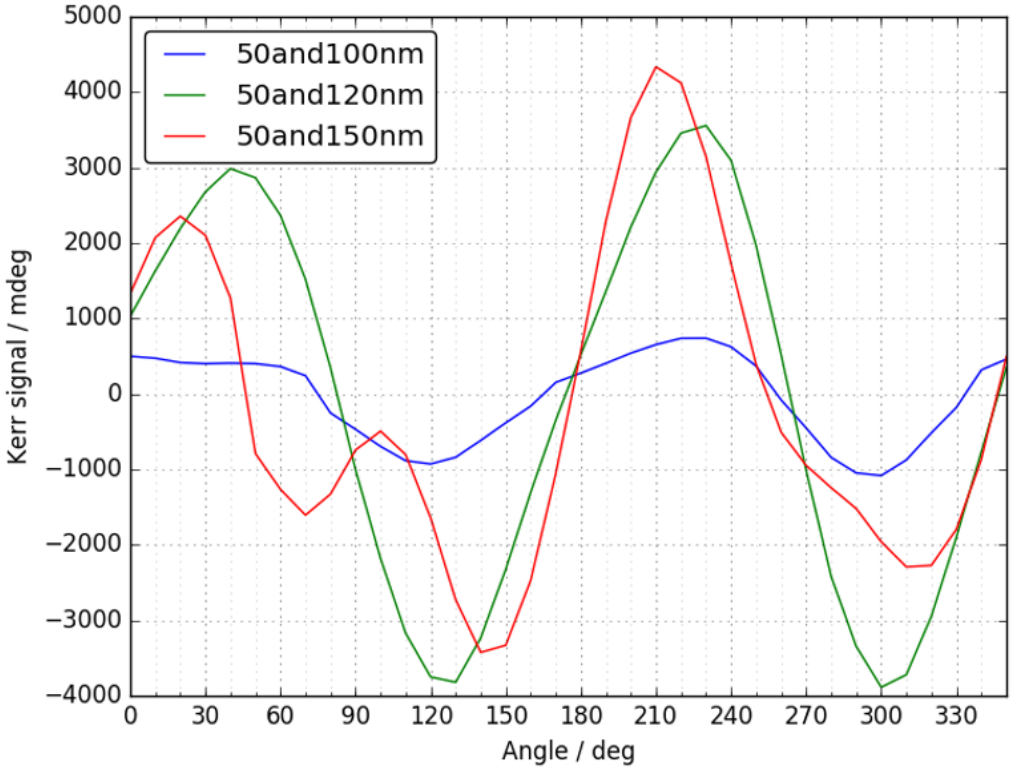

FIGURE 4.12: Measured Kerr signal against angle between the plane of incidence and the sample slits asymmetric samples.

It is also helpful to compare on the same graph the Kerr signal detected for an asymmetric sample with respect to the signal for a symmetric sample. Figure 4.13

presents the two signals, with the region where the optical activity was detected indicated by a dashed, light red line.

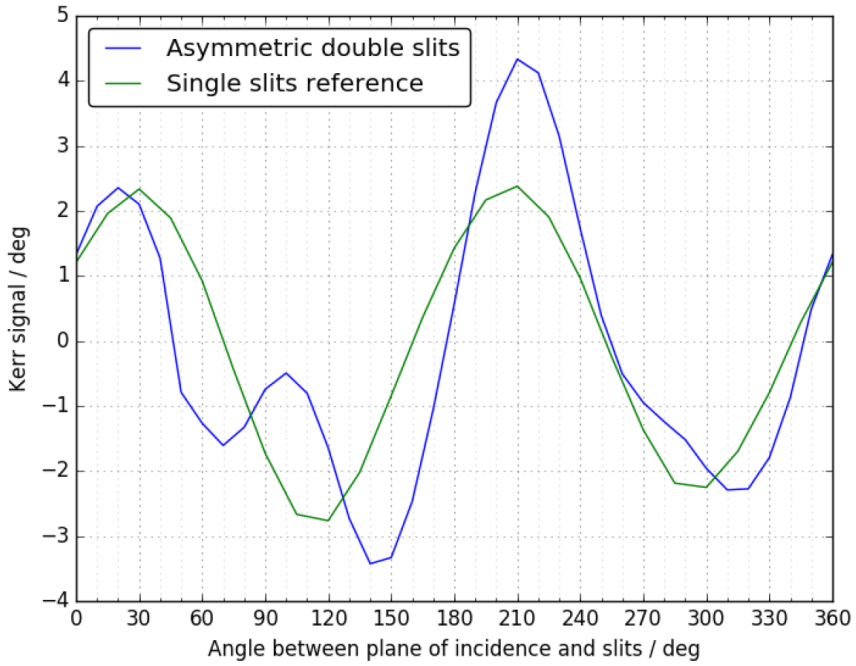

FIGURE 4.13: Measured Kerr signal compared between active and reference samples.

As shown on the figure, the reference sample shows a sinusoidal like dependence, whereas the asymmetric double slit sample shows more features, indicating potential optical activity. This typical sinusoidal variation of the Kerr signal for the symmetric metasurface originates from its inherent structural anisotropy of the design. The same response was observed for all of the single and double slit reference samples as well as the asymmetric samples which are not resonant with the wavelength of the laser. This background effect only varied in amplitude for the different samples.

This is sinusoidal variation is also seen for all the asymmetric slits, as shown on Figure 4.12, but it is accompanied by additional features, which can be regarded as modulation from the polarisation rotation. Importantly this modulation reverses when the sample is rotated through 180°, which is characteristic of the specular activity effect, which was the aim of this experiment.

The behaviour of the asymmetric metasurface is more complex, with two pronounced asymmetric features in the Kerr signal (amplitude 1°) located at 90° and 270° superimposed on the sinusoidal profile, which correspond to optical activity of opposite signs. They correspond to specular optical activity exhibited by the sample when the plane of incidence becomes parallel to the slits, with the strength of the effect of around 1°.

The results obtained for the three sizes of the asymmetric slits show that the specular optical activity was the strongest for the design that had the largest difference between the two slits forming a metamolecule, namely $50/150nm$ (red curve on Figure 4.12 and blue curve on Figure 4.13). For the two other asymmetric in size slits, the effect was not as strong. For these two other slits, with $50/100nm$ and $50/120nm$, some indication of specular optical cavity could be detected inspecting the asymmetry of the signal – the difference in the slope of the leading and the trailing edge of the sine-like curve (green and blue curve in Figure 4.12). Such asymmetry in the signal was not observed for the symmetric slits. The effect was expected to be the strongest for the largest difference in the two slit sizes, such as $50/150nm$, as indeed observed.

4.6 Robustness and long-term stability of symmetric and asymmetric slit metasurfaces

This section provides a more detailed account of the experimental work carried out, with the aim of confirming repeatability and robustness of the observed effect. The limited access to the NanoMOKE instruments as well as unavoidable delays, including those caused by maintenance and repairs, meant that the measurements presented here were collected over three years. Due to this, in some cases the samples were tested soon after their fabrication and then re-tested several months later. Care was taken to store the nanostructured gold samples in a suitable environment but despite this, possible deterioration of their quality and thus performance was expected.

New sets of samples were also fabricated, and given the challenging nanofabrication requirements, their quality was not always sufficient to use in experiments or detect such subtle effect as specular optical activity. The following figures capture the results from each round of experiments.

Two sets of samples were initially fabricated and called Set 2 containing asymmetric samples was assessed via SEM as having good quality. Previously Figure 4.4 showed the design of the three asymmetric slits. Set 2 results were included in the previous section already, but shown here for completeness and comparison. As described before, they had the structures milled from gold mounted on a fused quartz substrate. The unit cell was $250 \times 250nm$ unit and the total area was $20 \times 20\mu m$.

Figure 4.14 show the comparison of the Kerr signal dependence on rotation angle for measurements taken shortly after fabrication at RAL NanoMOKE3 (Figure 4.14(a)) and then after three months using Cambridge NanoMOKE3 instrument (Figure 4.14(b)). Only the most promising, $50/150nm$ sample, was tested in that second instrument to investigate reliability.

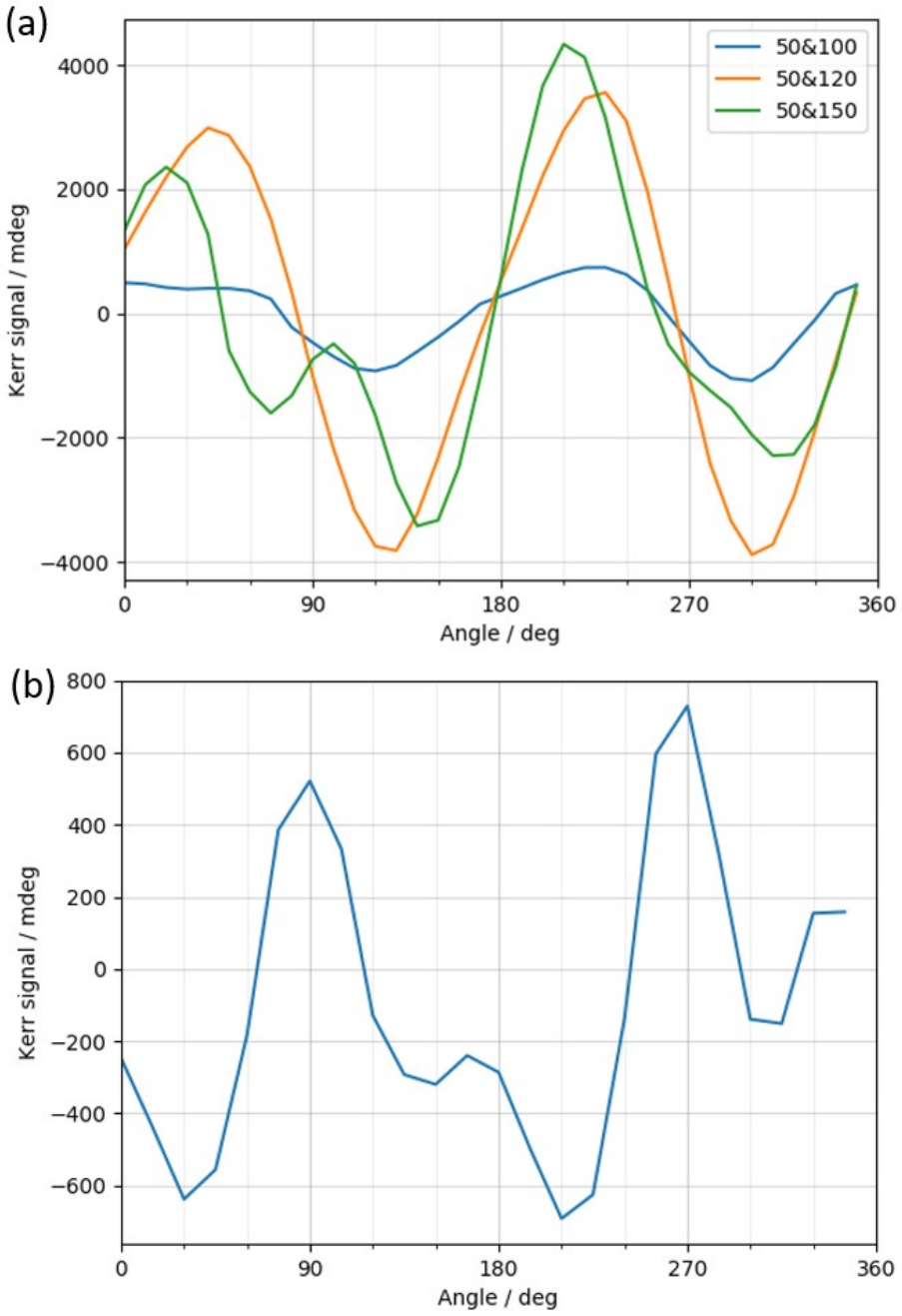

FIGURE 4.14: (a) Initial measurement with the setup at RAL, (b) Measurement three months later using the Cambridge setup.

In spite of using two different instruments and the passage of time the presence of the additional features/modulation can be observed in both experiments, thus confirming repeatability. The use of additional optics to focus the signal, available with the Cambridge NanoMOKE3 was also tried in this measurement, but this additional element did not bring any significant improvements in the resolution achieved.

For calibration and as an additional reference, a Kerr signal was collected for the incident light polarised along the perpendicular direction, namely s-polarisation on

the 50/150nm Set 2 slits.

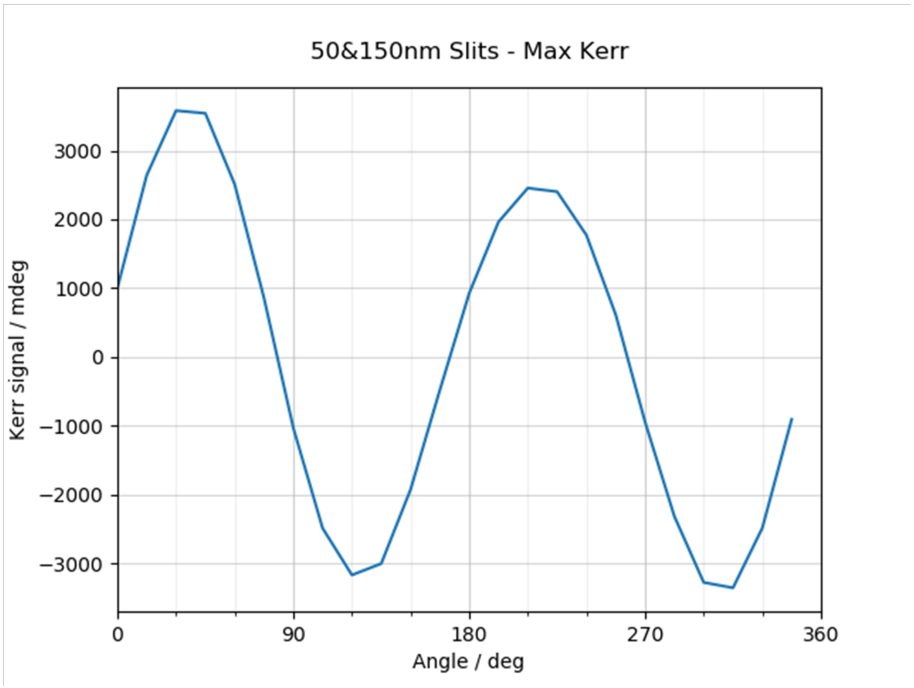

FIGURE 4.15: Kerr signal as sample was rotated for incident s-polarisation.

No specular optical activity was expected and, indeed, none was observed, as shown on Figure 4.15. This experiment was carried out after the measurement of Kerr signal for p-polarisation with the Cambridge NanoMOKE3 for the same set of 50/150nm slits (Figure 4.14(b)). The signal in Figure 4.15 shows a regular sine-like dependence, similar to the traces measured for the symmetric cells. This experiment on polarisation dependence provided an additional argument on the specular optical activity being the source of the additional features as detected and shown in Figure 4.14.

Figure 4.16 shows the follow-on measurements on the same Set 2 taken 17 months after the original measurement of Kerr signal. The experiments were carried out with the RAL NanoMOKE3. The experiment conducted after 17 months also included the measurements for a larger range of angles, namely from 0° to 720°.

Capturing the signal over this large range of angles means that the details of the additional features are less visible, even for the 50/150nm sample (green curve), but nevertheless, their presence was detected, thus again, confirming the robustness of the samples.

In parallel with the investigation of the asymmetric slits, similar long term stability tests were carried out for the symmetric slits. Figure 5.8 presents the main design of the symmetric slits, called Set 3.

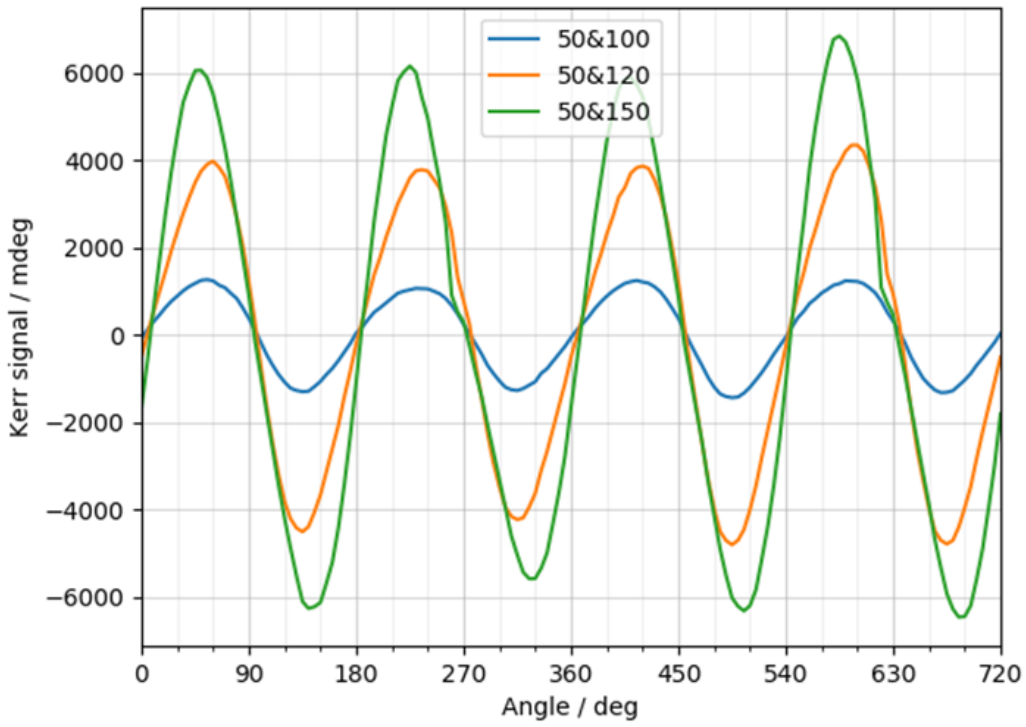

FIGURE 4.16: Kerr signal as sample was rotated.

The symmetric samples were fabricated together with the asymmetric ones, again milling their nanostructure in gold, supported by a quartz substrate. The metamolecules had unit cells size of $250 \times 250nm$ and the total area was $20 \times 20\mu m$.

Figure 4.17 shows the results of Kerr signal measured after 17 months. When compared to Figure 4.11 in both cases featureless sine-like dependence with respect to the rotation angle was measured, as expected.

In the next stage of the experimental work, new metasurfaces were fabricated to explore if the effect could be enhanced with improving further the quality and the precision of the slit shapes. The same design and size as the most promising sample explored before was fabricated. This challenging fabrication process produced one set that was deemed to have good quality, namely one set of symmetric $50/150nm$ slits as well as $150nm$ symmetric double slits, as seen from their SEM images, shown on Figure 4.18.

The fabrication of the samples took place 27 months after the initial fabrication. As seen from Figure 4.18, the SEM images indicated good quality and correct size of the slits. Kerr signal experiments were then carried out using RAL NanoMOKE3, following the same procedure. Two sessions scheduled over a period of seven weeks produced the plots shown in Figures 4.19, each session consisting of at least two sets of measurements. Unfortunately, the signal detected from the asymmetric samples

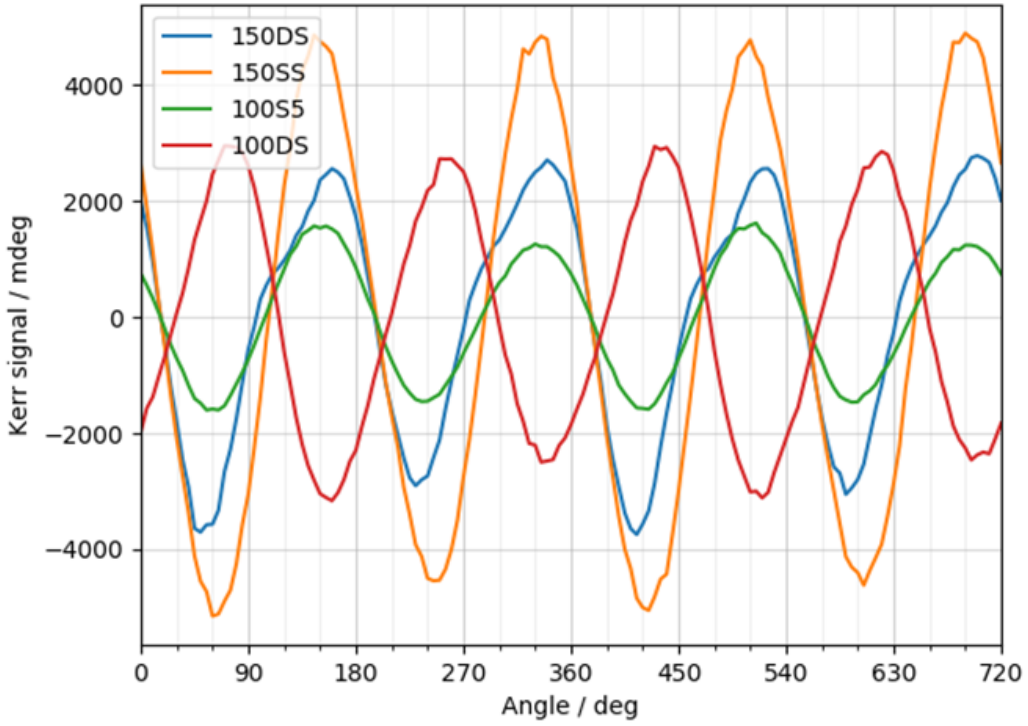

FIGURE 4.17: Kerr signal from reference samples as they were rotated.

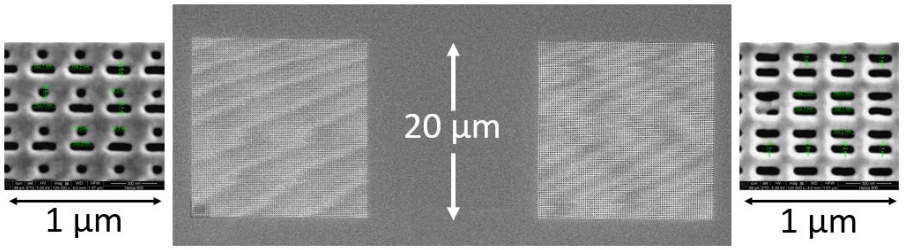

FIGURE 4.18: Active and reference sample pair SEM image.

was dominated by sine-like dependence, similar to the symmetric samples, thus not showing any obvious features originating from the specular optical activity.

The Kerr signal for the asymmetric slit sample, while not showing in such detail the additional features to the extent observed for the original Set 2, does not follow the regular, symmetric angle dependence as detected for the symmetric double slit sample. The leading and the trailing edge of the asymmetric slits Kerr signal are different, again indicating the influence of specular optical activity.

The repeated tests did not lead to resolving in more detail this difference between the two edges of the signal. It was also not possible to achieve a stronger indication of the specular optical activity effect. Inspecting the results from several experimental attempts confirmed that the precision of alignment was extremely crucial as well as the precise collimation of the beam. Instruments such as NanoMOKE3 are intended for testing other types of materials, such as larger samples ferromagnetics, so

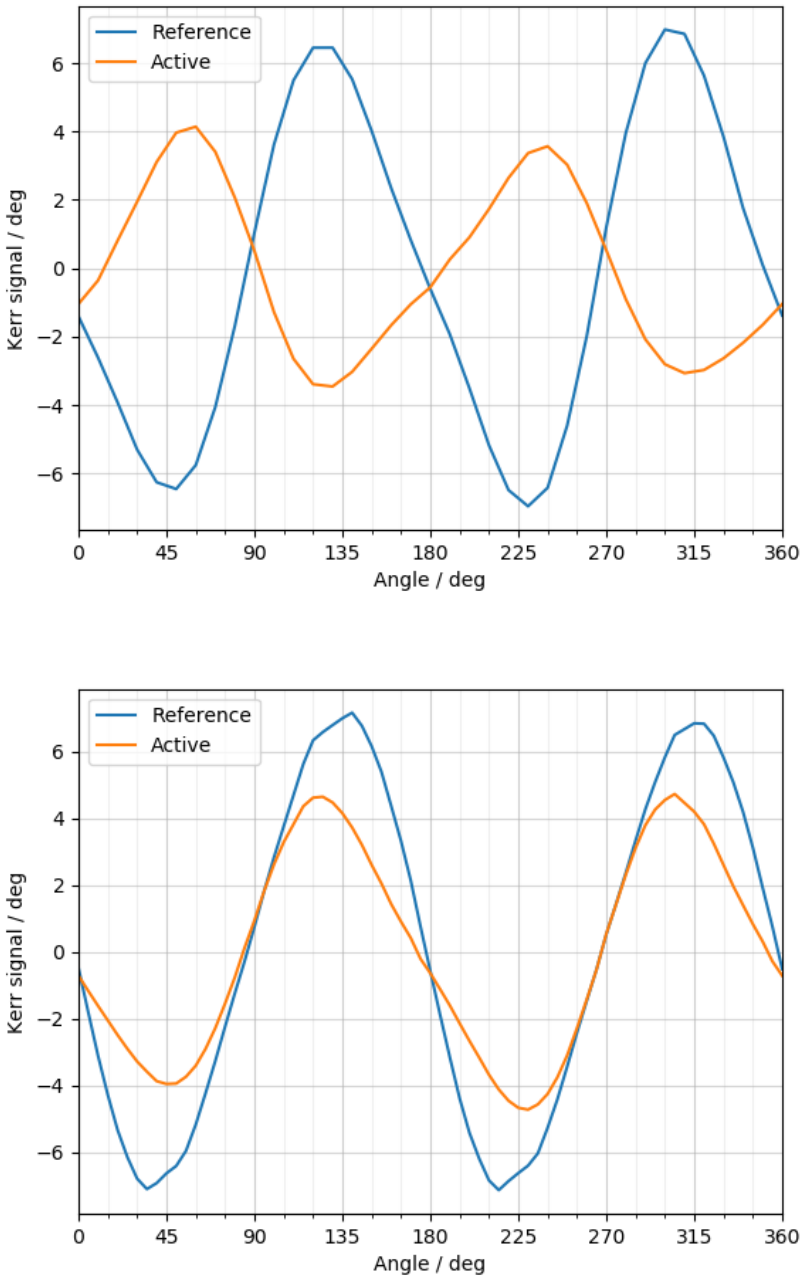

FIGURE 4.19: Kerr signal from 2 pairs of samples as they were rotated.

achieving precise alignment of the light source on a relatively, small sample proved very challenging as well as the position of the detector.

The incidence angle was also limited by the instruments constraints, with the option of just two incidence angles, namely 30° and 45°. Hence, it was not possible to optimise the incidence angle to achieve a stronger signal.

4.7 Conclusions

Specular optical activity is generally extremely weak, especially in the visible domain. This subtle effect was detected as the contribution to polarisation rotation coming from nanostructured metallic films that are not magnetic themselves and no magnetic field was present. Such specular optical activity in the visible part of the spectrum was shown as part of this thesis, for the first time to the best of our knowledge, present for a single reflection from nano-structured achiral metal surfaces.

The originally fabricated set of $50/150nm$ asymmetric samples produced the strongest evidence for specular optical activity, with the measurements being repeatable after three months. However, further tests revealed the issues with the long term stability of the samples as well as unknown contamination of the samples during nanofabrication which affected their performance.

This demonstration of principle could be followed by further experiments as well as simulations to extract more quantitative estimates on the magnitude of the optical activity observed as well as to potentially increase the effect. Further extension, in line with the other project carried out in this thesis, is to consider integrating the structure with liquid crystal chiral materials. However, as the results show here demonstrated, a detailed spectroscopy of nanostructured gold would be need to be captured to detect possible contamination or the use of different metals. Simulations will also aid further optimisation of the possible designs to optimise the strength of the specular optical activity.

In addition, while the NanoMOKE instrument can provide very high resolution measurements, it is not particularly flexible in terms of changing the incidence angle. The incidence angle of 30^o was attempted in this project, following the initial estimates as likely to yield the maximum effect, but exploring a wider range of incident angles and for all the sets of slits considered would provide a more comprehensive study of this phenomenon. Furthermore, the initial estimates also indicated that 50/120 nm slits would be the optimum design for maximising optical activity, while in fact 50/150 nm slits provided the strongest response. In order to carry out such investigations, own MOKE experimental set up would need to be designed and constructed rather to have the required flexibility in adjusting the measurement conditions.

Chapter 5

General conclusions and future work

In this thesis, three main, experimental projects were undertaken aiming to enhance the functionality of metasurfaces and exploring new effects using nanoscale metasurfaces.

In the first project, the reconfigurable metasurfaces with mechanical switching were investigated. The use of liquid crystals to reverse adhesion between the metasurface movable nanobridges was attempted with the aim to repair such metasurfaces by exploiting the elastic forces of liquid crystals. While the full reversal of stiction was not achieved, the results obtained indicated that liquid crystals affected the resonances of the liquid crystal loaded metasurface beyond just the change of the refractive index in the vicinity of the nano-bridges. The supply of good quality samples with such nanoscale metasurfaces proved increasingly difficult to obtain due to short circuit issues, possibly stemming from contamination during gold evaporation or gallium contamination during focused ion beam milling. Future work on this project, with good quality samples, could include using different fabrication techniques, such as e-beam. Other options include exploring different liquid crystals, namely those with higher elastic coefficients to engage stronger elastic forces to separate the stuck nanobridges, while also considering their viscosity and the conditions to promote their infiltration of the gaps between the nanobridges. Furthermore, with successful fabrication, the nanobridge wires of different length could be produced, thus exploring the strength of the restoring force for the liquid crystal.

One additional challenge with this project is that the resonances and the response of the nanobridge wires cannot be easily modelled. The detection of the stiction effect taking place relies on capturing the SEM images before and after voltage is applied. Such imaging cannot be done with a layer of liquid crystal integrated with the nanobridges. Hence, the effect of liquid crystal and the potential repair needs to be

deduced from the light transmission measurement, while ramping the voltage up and down. However, the liquid crystal alignment, and thus their effect on transmission will also change with applied voltage hence if they even partially remove the adhesion of the nanobridges, they may not be easily extracted from the experimental results.

The zigzag design was used in the second project, where zigzag metasurfaces fabricated for this thesis were used to explore the spatial coherence of light. The intriguing effect, where the resonance detected for the incoherent light was found not to match the theoretical simulation, with the model that assumed a coherent illuminating beam. The fabrication and the experiments confirmed this effect and included experiments on varying the spatial coherence of the illuminating sources by changing the size of the aperture near the sample. The dependence of the measured resonance of such variation of spatial coherence was observed. The effect was later explored and confirmed in a separate experiment (led by Dr T. Cookson) using OPO. Future work on this system could include a more comprehensive investigation of different tilt angles to explore the direction of the re-radiated, scattered light and whether beam steering could be achieved.

The third project, which again involved fabrication on the nanoscale, explored the effect of specular optical activity using samples with asymmetric slits, such as $50/150nm$. The challenging experimental work, as well as nanofabrication, provided evidence on the presence of such effect in the optical regime. In spite of the effect being quite subtle, the features observed for the Kerr signal reflected from such non-magnetic samples with respect to the angle of rotation showed potential specular optical activity. One of the main challenges concerned the use of MOKE instruments for such small and non-magnetic samples. MOKE magnetometers are intended for analysing much larger samples of ferromagnetic materials, inspecting for example, the magnetic grains of such bulk materials. Detecting specular optical activity with MOKE was carried out at the edge of this instrument resolution and proved challenging in understanding how the Kerr signal is processed, controlling the measurement of the signal and as well as achieving a precise alignment. This included the correct collimation of the beam to prevent the specular optical activity features being averaged out. Future work on this project, to achieve better resolution of the observed features and modulation would require building a dedicated optical set up to go beyond the indication of the effect collected from the use of a commercial MOKE magnetometer.

Appendix A

List of publications: Thomas Frank

A.1 Papers

Frank, T., Buchnev, O., Cookson, T., Kaczmarek, M., Lagoudakis, P., & Fedotov, V. A. (2019) "Discriminating between coherent and incoherent light with planar metamaterials". Nano Letters, 19(10), 6869-6875.

Buchnev, O., Podoliak, N., Frank, T., Kaczmarek, M., Jiang, L., & Fedotov, V. A. (2016). "Controlling stiction in nano-electro-mechanical systems using liquid crystals". ACS Nano, 10(12), 11519-11524.

A.2 Conferences

Buchnev, O., **Frank, T.**, Kaczmarek, M., Fedotov, V. A., "Novel liquid crystal-metamaterial hybrids with elasto-mechanical coupling", 2016, 26th International Liquid Crystal Conference (ILCC'16), USA.

Frank, T., Buchnev, O., Kaczmarek, M., Fedotov, V.A, "Specular optical activity from a metasurface at optical wavelengths", 2019, Photorefractive Photonics and beyond conference, France.

Frank, T. Buchnev, O., Cookson, T. Kaczmarek, M., Lagoudakis, P., Fedotov, V.A, "Sensing Spatial Coherence of Light with Planar Metallic Metamaterials", META 2021, Virtual Conference.

Gorecki, J., Frank, T., Buchnev, O., Stenning, G., Kaczmarek, M., Fedotov, V.A., "Mimicking longitudinal MOKE with metasurfaces", 2021, SPIE Optics & Photonics 2021, Virtual Conference.

Frank, T. Buchnev, O., Cookson, T. Kaczmarek, M., Lagoudakis, P., Fedotov, V.A, "Detecting Spatially Incoherent Light with Plasmonic Metasurfaces", 2020, Frontiers in Optics and Laser Science Conference, (OSA All-Virtual Meeting) USA.

Frank, T. Buchnev, O., Cookson, T., Kaczmarek, M., Lagoudakis, P., Fedotov, V.A, "Metasurfaces can Sense Spatial Coherence of Light", 2019, CLEO Europe - EQEC 2019, Germany.

Frank, T. Buchnev, O., Cookson, T., Kaczmarek, M., Lagoudakis, P., Fedotov, V.A, "Sensing Spatial Coherence of Light with Metasurfaces", 2019, SPIE Optics & Photonics, USA.

Frank, T. Buchnev, O., Cookson, T. Kaczmarek, M., Lagoudakis, P., Fedotov, V.A, "Detecting spatial coherence of light with planar metallic metamaterials", 2019, IEEE Proceedings Of The 2019 International Conference On Electromagnetics In Advanced Applications (ICEAA), 770, Spain.

Frank, T., Buchnev, O., Cookson, T., Kaczmarek, M., Lagoudakis, P., Fedotov, V.A, "Sensing spatial coherence of light with planar metamaterials", 2019, Metanano, Russia.

Frank, T., Buchnev, O., Cookson, T., Kaczmarek, M., Lagoudakis, P., Fedotov, V.A, "Sensing Spatial Coherence of Light with Metasurface", 2019, Photonics & Electromagnetics Research Symposium, PIERS 2019, Italy.

Frank, T. Buchnev, O., Cookson, T. Kaczmarek, M., Lagoudakis, P., Fedotov, V.A, "Detecting Coherence of Light with Metasurfaces", 2018, 12th International Congress on Artificial Materials for Novel Wave Phenomena – Metamaterials, Finland.

Buchnev, O., Frank, T., Podoliak, N., Kaczmarek, M., Jiang, L., Fedotov, V. A., "Tuneable liquid crystal-metamaterial hybrids with elasto-mechanical coupling, 2016, Metamaterials Conference, Greece.

Buchnev, O., Frank, T., Podoliak, N., Kaczmarek, M., Jiang, L., Fedotov, V. A., "Exploiting the full potential of liquid crystals in tuneable and re-configurable metamaterials", 2016, International Conference on Optical, Optoelectronic and Photonic Materials and Applications 2016 (ICOOPMA'16), Canada.

Appendix B

COMSOL Simulation Details

COMSOL was used to model the zigzag metasurfaces. The model consisted of a single unit of the gold metasurface placed on top of fused quartz and with air above. The quartz and air extend 2um away from the gold with refractive indices of 1.45 and 1 respectively. An interpolated model of the real and imaginary refractive indices was used to define the properties of the gold.

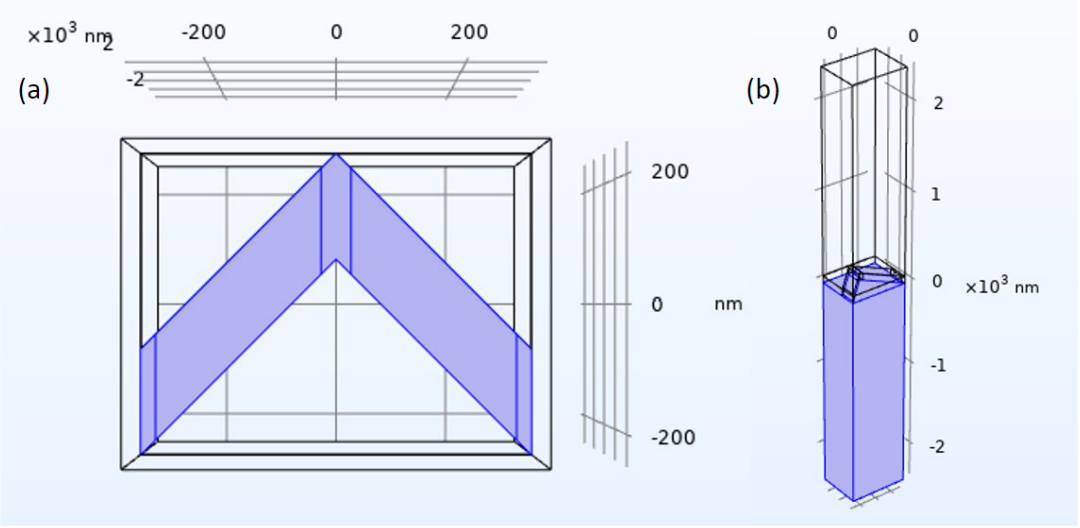

FIGURE B.1: (a) Blue volume defined as gold for the zigzag wire samples. The inverse selection is made for the zigzag slits. (b) Blue volume defined as fused quartz

The parameters of the model were varied to create the different aspect ratio and different parts were selected to be gold to create the inverted and isolated structures.

The 4 boundaries surrounding the metasurface were defined as periodic boundary conditions, effectively making the model an infinite plane. The top and bottom of the model were defined as ports to allow for waves to be created and collected. Scattering boundary conditions were used to eliminate any reflections from the ports.

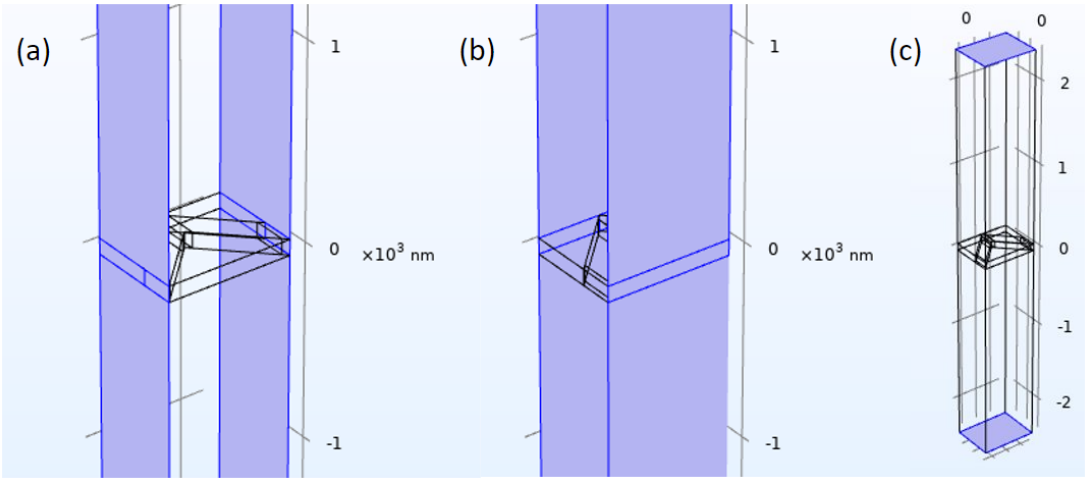

FIGURE B.2: (a)&(b) Periodic boundary conditions on the sides. (c) Ports with scattering boundary conditions at the top and bottom.

Finer mesh elements were used in the metasurface plane. Larger mesh elements were used for the air and glass volumes. The mesh was defined for 2 perpendicular sides and then copied to the opposite sides to ensure the mesh matched for the periodic boundary conditions. The internal volume mesh was then generated after this.

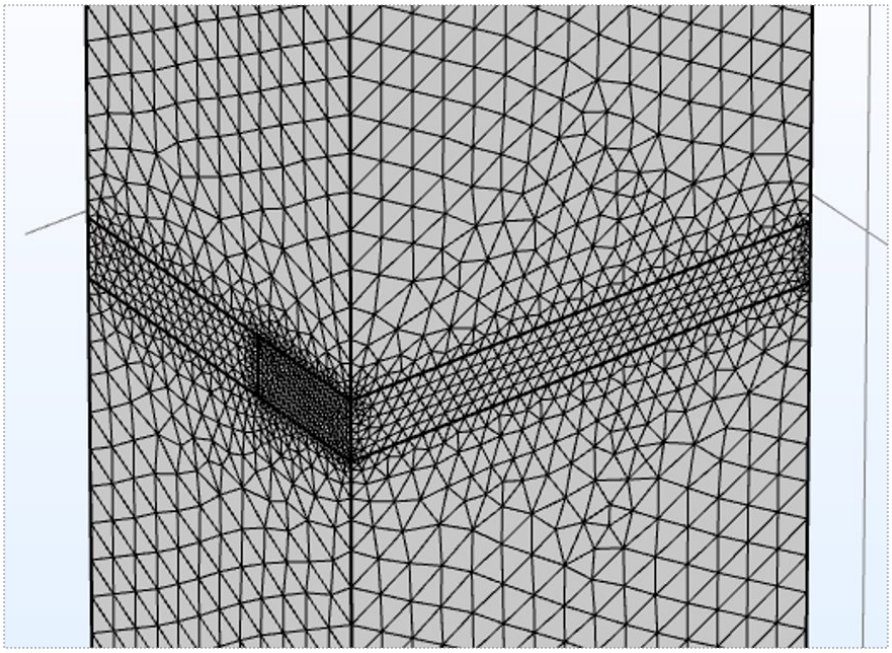

FIGURE B.3: The mesh.

References

[1] Weidong Zhou and Shanhui Fan. *Photonic Crystal Metasurface Optoelectronics*. Academic Press, 2019.

[2] Vladimir Alekseevich Belyakov et al. *Diffraction optics of complex-structured periodic media*. Springer, 1992.

[3] Richard A Shelby, David R Smith, and Seldon Schultz. Experimental verification of a negative index of refraction. *science*, 292(5514):77–79, 2001.

[4] Tolga Ergin, Nicolas Stenger, Patrice Brenner, John B Pendry, and Martin Wegener. Three-dimensional invisibility cloak at optical wavelengths. *Science*, 328(5976):337–339, 2010.

[5] Hyesog Lee, Zhaowei Liu, Yi Xiong, Cheng Sun, and Xiang Zhang. Development of optical hyperlens for imaging below the diffraction limit. *Optics express*, 15(24):15886–15891, 2007.

[6] Xingcun Colin Tong. *Functional metamaterials and metadevices*, volume 262. Springer, 2018.

[7] J. B. Pendry. Negative refraction makes a perfect lens. *Phys. Rev. Lett.*, 85:3966–3969, Oct 2000.

[8] Vladimir M Shalaev, Wenshan Cai, Uday K Chettiar, Hsiao-Kuan Yuan, Andrey K Sarychev, Vladimir P Drachev, and Alexander V Kildishev. Negative index of refraction in optical metamaterials. *Optics letters*, 30(24):3356–3358, 2005.

[9] DR Smith and R Liu. *Metamaterials: theory, design, and applications*. Springer, New York, 2010.

[10] Safa Kasap and Peter Capper. *Springer handbook of electronic and photonic materials*. Springer, 2017.

[11] Li Min and Lirong Huang. Perspective on resonances of metamaterials. *Opt. Express*, 23(15):19022–19033, Jul 2015.

[12] Leonard Lewin. The electrical constants of a material loaded with spherical particles. *Journal of the Institution of Electrical Engineers - Part III: Radio and Communication Engineering*, 94:65–68, 1947.

[13] Xiaobo Wang and Ji Zhou. Fano resonance in a subwavelength Mie-based metamolecule with split ring resonator. *Applied Physics Letters*, 110(25):254101, 06 2017.

[14] David R Smith and John B Pendry. Homogenization of metamaterials by field averaging. *JOSA B*, 23(3):391–403, 2006.

[15] Ruopeng Liu, Tie Jun Cui, Da Huang, Bo Zhao, and David R Smith. Description and explanation of electromagnetic behaviors in artificial metamaterials based on effective medium theory. *Physical Review E*, 76(2):026606, 2007.

[16] Viktor G Veselago. The electrodynamics of substances with simultaneously negative values of ϵ and μ. *Soviet physics uspekhi*, 10(4):509, 1968.

[17] Wei Ming Zhu, Ai Qun Liu, Xu Ming Zhang, Din Ping Tsai, Tarik Bourouina, Jing Hua Teng, Xin Hai Zhang, Hong Chen Guo, Hendrix Tanoto, Ting Mei, et al. Switchable magnetic metamaterials using micromachining processes. *Advanced Materials*, 23(15):1792–1796, 2011.

[18] Matthew J Dicken, Koray Aydin, Imogen M Pryce, Luke A Sweatlock, Elizabeth M Boyd, Sameer Walavalkar, James Ma, and Harry A Atwater. Frequency tunable near-infrared metamaterials based on vo 2 phase transition. *Optics express*, 17(20):18330–18339, 2009.

[19] JS Kyoung, MA Seo, SM Koo, HR Park, HS Kim, BJ Kim, HT Kim, NK Park, DS Kim, and KJ Ahn. Active terahertz metamaterials: Nano-slot antennas on vo2 thin films. *physica status solidi (c)*, 8(4):1227–1230, 2011.

[20] Oleksandr Buchnev, Nina Podoliak, Malgosia Kaczmarek, Nikolay I Zheludev, and Vassili A Fedotov. Electrically controlled nanostructured metasurface loaded with liquid crystal: toward multifunctional photonic switch. *Advanced Optical Materials*, 3(5):674–679, 2015.

[21] Ekmel Özbay. The magical world of photonic metamaterials. *Optics and Photonics News*, 19(11):22–27, 2008.

[22] Costas M Soukoulis and Martin Wegener. Past achievements and future challenges in the development of three-dimensional photonic metamaterials. *Nature photonics*, 5(9):523–530, 2011.

[23] Jun Zhao, Chunjie Zhang, Paul V Braun, and Harald Giessen. Large-area low-cost plasmonic nanostructures in the nir for fano resonant sensing. *Advanced Materials*, 24(35):OP247–OP252, 2012.

[24] Cyriaque Genet and Thomas W Ebbesen. Light in tiny holes. *Nature*, 445(7123):39–46, 2007.

[25] Ben A Munk. *Frequency selective surfaces: theory and design*. John Wiley & Sons, 2005.

[26] John C Vardaxoglou. Frequency selective surfaces: analysis and design. *(No Title)*, 1997.

[27] Vassili A Fedotov, Jan Wallauer, Markus Walther, Mauro Perino, Nikitas Papasimakis, and Nikolay I Zheludev. Wavevector selective metasurfaces and tunnel vision filters. *Light: Science & Applications*, 4(7):e306–e306, 2015.

[28] C Menzel, C Helgert, C Rockstuhl, E-B Kley, A Tünnermann, T Pertsch, and F Lederer. Asymmetric transmission of linearly polarized light at optical metamaterials. *Physical review letters*, 104(25):253902, 2010.

[29] Jiaming Hao, Yu Yuan, Lixin Ran, Tao Jiang, Jin Au Kong, Che Ting Chan, and Lei Zhou. Manipulating electromagnetic wave polarizations by anisotropic metamaterials. *Physical review letters*, 99(6):063908, 2007.

[30] Anders Pors, Michael G Nielsen, and Sergey I Bozhevolnyi. Plasmonic metagratings for simultaneous determination of stokes parameters. *Optica*, 2(8):716–723, 2015.

[31] Nader Engheta. Thin absorbing screens using metamaterial surfaces. In *IEEE Antennas and Propagation Society International Symposium (IEEE Cat. No. 02CH37313)*, volume 2, pages 392–395. IEEE, 2002.

[32] N Iê Landy, S Sajuyigbe, Jack J Mock, David R Smith, and Willie J Padilla. Perfect metamaterial absorber. *Physical review letters*, 100(20):207402, 2008.

[33] Francesco Aieta, Patrice Genevet, Mikhail A Kats, Nanfang Yu, Romain Blanchard, Zeno Gaburro, and Federico Capasso. Aberration-free ultrathin flat lenses and axicons at telecom wavelengths based on plasmonic metasurfaces. *Nano letters*, 12(9):4932–4936, 2012.

[34] Satoshi Ishii, Vladimir M Shalaev, and Alexander V Kildishev. Holey-metal lenses: sieving single modes with proper phases. *Nano letters*, 13(1):159–163, 2013.

[35] Nanfang Yu and Federico Capasso. Flat optics with designer metasurfaces. *Nature materials*, 13(2):139–150, 2014.

[36] SS Wang and RJAO Magnusson. Theory and applications of guided-mode resonance filters. *Applied optics*, 32(14):2606–2613, 1993.

[37] Weidong Zhou, Deyin Zhao, Yi-Chen Shuai, Hongjun Yang, Santhad Chuwongin, Arvinder Chadha, Jung-Hun Seo, Ken X Wang, Victor Liu, Zhenqiang Ma, et al. Progress in 2d photonic crystal fano resonance photonics. *Progress in Quantum Electronics*, 38(1):1–74, 2014.

[38] Fu Min Huang, Tsung Sheng Kao, Vassili A Fedotov, Yifang Chen, and Nikolay I Zheludev. Nanohole array as a lens. *Nano letters*, 8(8):2469–2472, 2008.

[39] AS Schwanecke, VA Fedotov, VV Khardikov, SL Prosvirnin, Y Chen, and NI Zheludev. Nanostructured metal film with asymmetric optical transmission. *Nano letters*, 8(9):2940–2943, 2008.

[40] Eric Plum, Vassili A Fedotov, and Nikolay I Zheludev. Specular optical activity of achiral metasurfaces. *Applied Physics Letters*, 108(14):141905, 2016.

[41] Marek S Wartak, Kosmas L Tsakmakidis, and Ortwin Hess. Introduction to metamaterials. *Physics in Canada*, 67(1):30–34, 2011.

[42] Augustine M Urbas, Zubin Jacob, Luca Dal Negro, Nader Engheta, A D Boardman, P Egan, Alexander B Khanikaev, Vinod Menon, Marcello Ferrera, Nathaniel Kinsey, Clayton DeVault, Jongbum Kim, Vladimir Shalaev, Alexandra Boltasseva, Jason Valentine, Carl Pfeiffer, Anthony Grbic, Evgenii Narimanov, Linxiao Zhu, Shanhui Fan, Andrea AlÃ¹, Ekaterina Poutrina, Natalia M Litchinitser, Mikhail A Noginov, Kevin F MacDonald, Eric Plum, Xiaoying Liu, Paul F Nealey, Cherie R Kagan, Christopher B Murray, Dorota A Pawlak, Igor I Smolyaninov, Vera N Smolyaninova, and Debashis Chanda. Roadmap on optical metamaterials. *Journal of Optics*, 18(9):093005, aug 2016.

[43] Peter J Collings and Michael Hird. *Introduction to liquid crystals: chemistry and physics*. CRC Press, 1997.

[44] Nico Vieweg, Christian Jansen, Mohammad Khaled Shakfa, Maik Scheller, Norman Krumbholz, Rafal Wilk, Martin Mikulics, and Martin Koch. Molecular properties of liquid crystals in the terahertz frequency range. *Opt. Express*, 18(6):6097–6107, Mar 2010.

[45] E. Hecht. *Optics*. Addison-Wesley, 2002.

[46] Fuli Zhang, Qian Zhao, Lei Kang, Davy P Gaillot, Xiaopeng Zhao, Ji Zhou, and Didier Lippens. Magnetic control of negative permeability metamaterials based on liquid crystals. In *2008 38th European Microwave Conference*, pages 801–804. IEEE, 2008.

[47] Qian Zhao, Lei Kang, Bo Du, Bo Li, Ji Zhou, Hong Tang, Xiao Liang, and Baizhe Zhang. Electrically tunable negative permeability metamaterials based on nematic liquid crystals. *Applied physics letters*, 90(1):011112, 2007.

[48] Shumin Xiao, Uday K Chettiar, Alexander V Kildishev, Vladimir Drachev, IC Khoo, and Vladimir M Shalaev. Tunable magnetic response of metamaterials. *Applied Physics Letters*, 95(3):033115, 2009.

[49] Boyoung Kang, JH Woo, E Choi, Hyun-Hee Lee, ES Kim, J Kim, Tae-Jong Hwang, Young-Soon Park, DH Kim, and JW Wu. Optical switching of near infrared light transmission in metamaterial-liquid crystal cell structure. *Optics Express*, 18(16):16492–16498, 2010.

[50] Alexander Minovich, James Farnell, Dragomir N Neshev, Ian McKerracher, Fouad Karouta, Jie Tian, David A Powell, Ilya V Shadrivov, Hark Hoe Tan, Chennupati Jagadish, et al. Liquid crystal based nonlinear fishnet metamaterials. *Applied Physics Letters*, 100(12):121113, 2012.

[51] O Buchnev, JY Ou, M Kaczmarek, NI Zheludev, and VA Fedotov. Electro-optical control in a plasmonic metamaterial hybridised with a liquid-crystal cell. *Optics express*, 21(2):1633–1638, 2013.

[52] Fuli Zhang, Weihong Zhang, Qian Zhao, Jingbo Sun, Kepeng Qiu, Ji Zhou, and Didier Lippens. Electrically controllable fishnet metamaterial based on nematic liquid crystal. *Optics express*, 19(2):1563–1568, 2011.

[53] Iam Choon Khoo. Nonlinear optics, active plasmonics and metamaterials with liquid crystals. *Progress in Quantum Electronics*, 38(2):77–117, 2014.

[54] Manuel Decker, Christian Kremers, Alexander Minovich, Isabelle Staude, Andrey E Miroshnichenko, Dmitry Chigrin, Dragomir N Neshev, Chennupati Jagadish, and Yuri S Kivshar. Electro-optical switching by liquid-crystal controlled metasurfaces. *Optics express*, 21(7):8879–8885, 2013.

[55] Nikolay I Zheludev and Yuri S Kivshar. From metamaterials to metadevices. *Nature materials*, 11(11):917–924, 2012.

[56] Ilya V Shadrivov, Mikhail Lapine, Yuri S Kivshar, et al. *Nonlinear, tunable and active metamaterials*. Springer, 2015.

[57] Imogen M Pryce, Koray Aydin, Yousif A Kelaita, Ryan M Briggs, and Harry A Atwater. Highly strained compliant optical metamaterials with large frequency tunability. *Nano letters*, 10(10):4222–4227, 2010.

[58] Mikhail Lapine, Ilya V Shadrivov, David A Powell, and Yuri S Kivshar. Metamaterials with conformational nonlinearity. *Scientific Reports*, 1(1):138, 2011.

[59] Hu Tao, AC Strikwerda, K Fan, Willie J Padilla, X Zhang, and RD Averitt. Reconfigurable terahertz metamaterials. *Physical review letters*, 103(14):147401, 2009.

[60] Jun-Yu Ou, Eric Plum, Liudi Jiang, and Nikolay I Zheludev. Reconfigurable photonic metamaterials. *Nano letters*, 11(5):2142–2144, 2011.

[61] PR Evans, GA Wurtz, WR Hendren, R Atkinson, W Dickson, AV Zayats, and RJ Pollard. Electrically switchable nonreciprocal transmission of plasmonic nanorods with liquid crystal. *Applied Physics Letters*, 91(4):043101, 2007.

[62] SM Spearing. Materials issues in microelectromechanical systems (mems). *Acta materialia*, 48(1):179–196, 2000.

[63] AD Romig Jr, Michael T Dugger, and Paul J McWhorter. Materials issues in microelectromechanical devices: science, engineering, manufacturability and reliability. *Acta Materialia*, 51(19):5837–5866, 2003.

[64] KL Ekinci and ML Roukes. Nanoelectromechanical systems. *Review of scientific instruments*, 76(6), 2005.

[65] Hyungsoon Im, Xing-Jiu Huang, Bonsang Gu, and Yang-Kyu Choi. A dielectric-modulated field-effect transistor for biosensing. *Nature nanotechnology*, 2(7):430–434, 2007.

[66] Akshay K Naik, MS Hanay, WK Hiebert, XL Feng, and Michael L Roukes. Towards single-molecule nanomechanical mass spectrometry. *Nature nanotechnology*, 4(7):445–450, 2009.

[67] Tolga Bagci, Anders Simonsen, Silvan Schmid, Luis G Villanueva, Emil Zeuthen, Jürgen Appel, Jacob M Taylor, A Sørensen, Koji Usami, Albert Schliesser, et al. Optical detection of radio waves through a nanomechanical transducer. *Nature*, 507(7490):81–85, 2014.

[68] Uzma Akram, Nikolai Kiesel, Markus Aspelmeyer, and Gerard J Milburn. Single-photon opto-mechanics in the strong coupling regime. *New Journal of Physics*, 12(8):083030, 2010.

[69] Ewold Verhagen, Samuel Deléglise, Stefan Weis, Albert Schliesser, and Tobias J Kippenberg. Quantum-coherent coupling of a mechanical oscillator to an optical cavity mode. *Nature*, 482(7383):63–67, 2012.

[70] Sang Wook Lee, Dong Su Lee, Raluca E Morjan, Sung Ho Jhang, Martin Sveningsson, OA Nerushev, Yung Woo Park, and Eleanor EB Campbell. A three-terminal carbon nanorelay. *Nano letters*, 4(10):2027–2030, 2004.

[71] Weon Wi Jang, Jeong Oen Lee, Jun-Bo Yoon, Min-Sang Kim, Ji-Myoung Lee, Sung-Min Kim, Keun-Hwi Cho, Dong-Won Kim, Donggun Park, and Won-Seong Lee. Fabrication and characterization of a nanoelectromechanical switch with 15-nm-thick suspension air gap. *Applied Physics Letters*, 92(10), 2008.

[72] Owen Y Loh and Horacio D Espinosa. Nanoelectromechanical contact switches. *Nature nanotechnology*, 7(5):283–295, 2012.

[73] Jun-Yu Ou, Eric Plum, Jianfa Zhang, and Nikolay I Zheludev. An electromechanically reconfigurable plasmonic metamaterial operating in the near-infrared. *Nature nanotechnology*, 8(4):252–255, 2013.

[74] Kenzo Yamaguchi, Masamitsu Fujii, Toshihiro Okamoto, and Masanobu Haraguchi. Electrically driven plasmon chip: Active plasmon filter. *Applied Physics Express*, 7(1):012201, 2013.

[75] Rutger Thijssen, Ewold Verhagen, Tobias J Kippenberg, and Albert Polman. Plasmon nanomechanical coupling for nanoscale transduction. *Nano letters*, 13(7):3293–3297, 2013.

[76] Xianliang Liu and Willie J Padilla. Dynamic manipulation of infrared radiation with mems metamaterials. *Advanced Optical Materials*, 1(8):559–562, 2013.

[77] Kenzo Yamaguchi, Hiroki Yamanaka, Tomoya Ohtsu, and Satoshi Ishii. Electrically driven plasmon chip: Active plasmon lens in the visible range. *Applied Physics Letters*, 108(11), 2016.

[78] Roya Maboudian and Roger T Howe. Critical review: Adhesion in surface micromechanical structures. *Journal of Vacuum Science & Technology B: Microelectronics and Nanometer Structures Processing, Measurement, and Phenomena*, 15(1):1–20, 1997.

[79] Zhao Yapu. Stiction and anti-stiction in mems and nems. *Acta Mechanica Sinica*, 19(1):1–10, 2003.

[80] Henry Guckel, Jeffrey J Sniegowski, Todd R Christenson, and Farshid Raissi. The application of fine-grained, tensile polysilicon to mechanicaly resonant transducers. *Sensors and Actuators A: Physical*, 21(1-3):346–351, 1990.

[81] Roya Maboudian. Surface processes in mems technology. *Surface Science Reports*, 30(6-8):207–269, 1998.

[82] Roya Maboudian, W Robert Ashurst, and Carlo Carraro. Tribological challenges in micromechanical systems. *Tribology letters*, 12:95–100, 2002.

[83] CH Mastrangelo. Adhesion-related failure mechanisms in micromechanical devices. *Tribology Letters*, 3(3):223–238, 1997.

[84] MP De Boer and TM Mayer. Tribology of mems. *Mrs Bulletin*, 26(4):302–304, 2001.

[85] Roya Maboudian, W Robert Ashurst, and Carlo Carraro. Self-assembled monolayers as anti-stiction coatings for mems: characteristics and recent developments. *Sensors and Actuators A: Physical*, 82(1):219–223, 2000.

[86] Lei L Mercado, S-M Kuo, T-YT Lee, and Lianjun Liu. Mechanics-based solutions to rf mems switch stiction problem. *IEEE Transactions on Components and Packaging Technologies*, 27(3):560–567, 2004.

[87] Jeong Oen Lee, Yong-Ha Song, Min-Wu Kim, Min-Ho Kang, Jae-Sub Oh, Hyun-Ho Yang, and Jun-Bo Yoon. A sub-1-volt nanoelectromechanical switching device. *Nature nanotechnology*, 8(1):36–40, 2013.

[88] W Robert Ashurst, C Carraro, and Roya Maboudian. Vapor phase anti-stiction coatings for mems. *IEEE Transactions on Device and Materials Reliability*, 3(4):173–178, 2003.

[89] Oleksandr Buchnev, Nina Podoliak, Thomas Frank, Malgosia Kaczmarek, Liudi Jiang, and Vassili A Fedotov. Controlling stiction in nano-electro-mechanical systems using liquid crystals. *ACS nano*, 10(12):11519–11524, 2016.

[90] Nicolas Brouckaert, Nina Podoliak, Tetiana Orlova, Denitsa Bankova, Angela F De Fazio, Antonios G Kanaras, Ondrej Hovorka, Giampaolo D'Alessandro, and Malgosia Kaczmarek. Nanoparticle-induced property changes in nematic liquid crystals. *Nanomaterials*, 12(3):341, 2022.

[91] M Cui and JR Kelly. Temperature dependence of visco-elastic properties of 5cb. *Molecular Crystals and Liquid Crystals Science and Technology. Section A. Molecular Crystals and Liquid Crystals*, 331(1):49–57, 1999.

[92] Nanfang Yu, Patrice Genevet, Francesco Aieta, Mikhail A Kats, Romain Blanchard, Guillaume Aoust, Jean-Philippe Tetienne, Zeno Gaburro, and Federico Capasso. Flat optics: controlling wavefronts with optical antenna metasurfaces. *IEEE Journal of Selected Topics in Quantum Electronics*, 19(3):4700423–4700423, 2013.

[93] Ian H Malitson. Interspecimen comparison of the refractive index of fused silica. *Josa*, 55(10):1205–1209, 1965.

[94] Edward D Palik. *Handbook of optical constants of solids*, volume 3. Academic press, 1998.

[95] Thomas Frank, Oleksandr Buchnev, Tamsin Cookson, Malgosia Kaczmarek, Pavlos Lagoudakis, and VA Fedotov. Discriminating between coherent and incoherent light with planar metamaterials. *Nano Letters*, 19(10):6869–6875, 2019.

[96] VA Fedotov, PL Mladyonov, SL Prosvirnin, and NI Zheludev. Planar electromagnetic metamaterial with a fish scale structure. *Physical Review E*, 72(5):056613, 2005.

[97] Ingo Dierking. Chiral liquid crystals: Structures, phases, effects. *Symmetry*, 6(2):444–472, 2014.

[98] Frank L Pedrotti, Leno M Pedrotti, and Leno S Pedrotti. *Introduction to optics*. Cambridge University Press, 2017.

[99] Martti Kauranen and Stefano Cattaneo. Polarization techniques for surface nonlinear optics. *Progress in Optics*, 51:69–120, 2008.

[100] Justyna K Gansel, Michael Thiel, Michael S Rill, Manuel Decker, Klaus Bade, Volker Saile, Georg von Freymann, Stefan Linden, and Martin Wegener. Gold helix photonic metamaterial as broadband circular polarizer. *science*, 325(5947):1513–1515, 2009.

[101] Yuri Svirko, Nikolay Zheludev, and Michail Osipov. Layered chiral metallic microstructures with inductive coupling. *Applied physics letters*, 78(4):498–500, 2001.

[102] Alexei A Maradudin. *Structured surfaces as optical metamaterials*. Cambridge University Press, 2011.

[103] MP Silverman and J Badoz. Multiple reflection from isotropic chiral media and the enhancement of chiral asymmetry. *Journal of electromagnetic waves and applications*, 6(5-6):587–601, 1992.

[104] E Plum, X-X Liu, VA Fedotov, Y Chen, DP Tsai, and NI Zheludev. Metamaterials: optical activity without chirality. *Physical review letters*, 102(11):113902, 2009.

[105] E Plum, VA Fedotov, and NI Zheludev. Optical activity in extrinsically chiral metamaterial. *Applied physics letters*, 93(19), 2008.

[106] D A Allwood, Gang Xiong, M D Cooke, and R P Cowburn. Magneto-optical kerr effect analysis of magnetic nanostructures. *Journal of Physics D: Applied Physics*, 36(18):2175, sep 2003.

[107] Wen-Chin Lin, Chiao-Sung Chi, Tsung-Ying Ho, Cheng-Jui Tsai, Fang-Yuh Lo, Huan-Chia Chuang, and Ming-Yau Chern. Hydrogenation-induced change of magneto optical Kerr effect in Pd/Fe bilayers. *Journal of Applied Physics*, 112(6):063914, 09 2012.